

MATHEMATICAL MODELING AND SIMULATION OF MECHANOELECTRICAL
TRANSDUCERS AND NANOFUIDIC CHANNELS

By

Jin Kyoung Park

A DISSERTATION

Submitted to
Michigan State University
in partial fulfillment of the requirements
for the degree of

Mathematics - Doctor of Philosophy

2014

ABSTRACT

MATHEMATICAL MODELING AND SIMULATION OF MECHANOELECTRICAL TRANSDUCERS AND NANOFLUIDIC CHANNELS

By

Jin Kyoung Park

Remarkable advances in nanotechnology and computational approaches enable researchers to investigate physical and biological phenomena in an atomic or molecular scale. Smaller-scale approaches are important to study the transport of ions and/or molecules through ion channels in living organisms as well as exquisitely fabricated nanofluidic channels. Both subjects have similar physical properties and hence they have common mathematical interests and challenges in modeling and simulating the transport phenomena. In this work, we first propose and validate a molecular level prototype for mechanoelectrical transducer (MET) channel in mammalian hair cells. Next, we design three ionic diffusive nanofluidic channels with different types of atomic surface charge distribution, and explore the current properties of each channel.

We construct the molecular level prototype which consists of a charged blocker, a realistic ion channel and its surrounding membrane. The Gramicidin A channel is employed to demonstrate the realistic channel structure, and the blocker is a positively charged atom of radius 1.5\AA which is placed at the mouth region of the channel. Relocating this blocker along one direction just outside the channel mouth imitates the opening and closing behavior of the MET channel. In our atomic scale design for an ionic diffusive nanofluidic channel, the atomic surface charge distribution is easy to modify by varying quantities and signs of atomic charges which are equally placed slightly above the channel surface. Our proposed nanofluidic

systems constitutes a geometrically well-defined cylindrical channel and two reservoirs of KCl solution.

For both the mammalian MET channel and the ion diffusive nanofluidic channel, we employ a well-established ion channel continuum theory, Poisson-Nernst-Planck theory, for three dimensional numerical simulations. In particular, for the nano-scaled channel descriptions, the generalized PNP equations are derived by using a variational formulation and by incorporating non-electrostatic interactions. We utilize several useful mathematical algorithms, such as Dirichlet to Neumann mapping and the matched interface and boundary method, in order to validate the proposed models with charge singularities and complex geometry. Moreover, the second-order accuracy of the proposed numerical methods are confirmed with our nanofluidic system affected by a single atomic charge and eight atomic charges, and further study the channels with a unipolar charge distribution of negative ions and a bipolar charge distribution.

Finally, we analyze electrostatic potential and ion conductance through each channel model under the influence of diverse physical conditions, including external applied voltage, bulk ion concentration and atomic charge. Our MET channel prototype shows an outstanding agreement with experimental observation of rat cochlear outer hair cells in terms of open probability. This result also suggests that the tip link, a connector between adjacent stereocilia, gates the MET channel. Similarly, numerical findings, such as ion selectivity, ion depletion and accumulation, and potential wells, of our proposed ion diffusive realistic nanochannels are in remarkable accordance with those from experimental measurements and numerical simulations in the literature. In addition, simulation results support the controllability of the current within a nanofluidic channel.

To my parents, Jongyoul Park and Sunkyoung Choi, and my sister, Minkyung Park

ACKNOWLEDGMENTS

Over the past eight years, it has been a challenging and rewarding journey for me to complete the PhD study. I would never have been able to finish my dissertation without the guidance of my committee members, support from my family, and help from my friends and colleagues. Within the limited space, I wish to acknowledge those who contribute to my achievement.

I would like to thank all my comprehensive exam and dissertation defense committee members, Dr. Guowei Wei, Dr. Chichia Chiu, Dr. Jongeun Choi, Dr. Andrew Christlieb, Dr. Russell Schwab and Dr. Moxun Tang for their valuable time and support. Especially, I would like to express my deepest and sincerest gratitude to my advisor, Dr. Guowei Wei, for his thoughtful guidance, encouragement, caring and patience. He has provided me a systematic training in computational skills and a broad understanding of several research fields, including Mathematics, Biology, Chemistry, Physics and Engineering. He also led me to build an interdisciplinary perspective. Five years' study with him taught me to have great passion in research.

I would like to express immeasurable gratitude to my lovely family. My father is always my first and everlasting mentor, my mother supports me in every way and my wonderful sister is my lifetime companion.

Especially, I deeply appreciate my precious friends, Ms. Yeoreum Lee and Mr. Daewoo Pak for helping with the preparation for my dissertation defense presentation. I also would like to thank Dr. Sanghyup Jeong, who has been a mentor in that he gave me considerate advice on overcoming difficulties as a PhD student.

Finally, I would like to thank my other friends as a colleague. Firstly, I appreciate Dr. Kelin Xia for his valuable help in programming tools and research tips whenever I met

difficulties in my work. Many thanks also go to the rest of former and current members in Dr. Wei's group, Dr. Duan Chen, Dr. Zhan Chen, Dr. Langhua Hu, Mr. Yin Cao and Ms. Weijuan Zhou, for their cooperation. Further, I would like to express gratitude to my other MSU friends, Dr. Kyungbae Park, Ms. Hana Cho, Ms. Bosu Choi, Mr. Seonghak Kim, Mr. Sugil Lee and Mr. Woong Bae Park, for their encouragement.

TABLE OF CONTENTS

LIST OF TABLES	ix
LIST OF FIGURES	x
Chapter 1 Introduction	1
1.1 Introduction to mechanoelectrical transducer channel in auditory system . .	1
1.2 Introduction to nanofluidic channels	4
1.3 Review of current computational models	10
1.3.1 Three representative computational approaches	11
1.3.1.1 Molecular dynamics	11
1.3.1.2 Stochastic dynamics	12
1.3.1.3 Continuum models	14
1.3.2 Modeling and simulation of biological ion channels	18
1.3.3 Modeling and simulation of synthetic nanofluidic channels	21
1.4 Existing challenges	23
1.4.1 Existing challenges in mechanoelectrical transducer channel	23
1.4.2 Existing challenges in nanofluidics	24
Chapter 2 Theoretical models and mathematical algorithms	26
2.1 Generalized Poisson-Nernst-Planck (PNP) model	26
2.1.1 Computational domain	27
2.1.2 Energy functional	29
2.1.3 Governing equations	34
2.2 Mathematical algorithms	38
Chapter 3 Modeling and simulating a mechanoelectrical transducer (MET) channel in mammalian hair cells in molecular level	41
3.1 A molecular level prototype of a MET channel	42
3.2 Computational setup for the PNP systems	44
3.3 MET channel prototype simulations	46
3.3.1 Experimental data	46
3.3.2 Computational results	47
3.4 Concluding remarks	53
Chapter 4 Modeling and simulating three types of ionic diffusive nanoflu- idic channels	56
4.1 Atomic scale design of an ionic diffusive nanofluidic channel	57

4.2	Numerical validation	59
4.2.1	Analytical solution system	60
4.2.2	A cylindrical nanochannel with a single atomic charge	61
4.2.3	A cylindrical nanochannel with eight atomic charges	62
4.2.4	A negatively charged ionic diffusive nanofluidic channel	64
4.2.5	A bipolar ionic diffusive nanofluidic channel	66
4.3	Nanofluidic simulations	68
4.3.1	A negatively charged ionic diffusive nanofluidic channel	69
4.3.2	A bipolar ionic diffusive nanofluidic channel	76
4.3.3	A double-well ionic diffusive nanofluidic channel	82
4.4	Concluding remarks	85
Chapter 5	Thesis achievements and future work	88
5.1	Contributions	89
5.1.1	On the modeling and simulating a MET channel in mammalian hair cells	89
5.1.2	On the modeling and simulating charged nanofluidic channels	91
5.2	Future work	92
APPENDICES	94
A	Mathematical algorithms	95
A.1	Dirichlet to Neumann mapping	95
A.2	Matched interface and boundary (MIB) method	96
A.3	Iterations of Poisson and Nernst-Planck equations	99
B	Unit system	102
C	Atomic charge distribution	105
C.1	A negatively charged channel	105
C.2	A bipolar channel	106
C.3	A double-well channel	107
BIBLIOGRAPHY	108

LIST OF TABLES

Table 4.1	Numerical errors and orders for the cylindrical channel with a single atomic charge.	63
Table 4.2	Numerical errors and orders for the cylindrical channel with eight atomic charges.	63
Table 4.3	Numerical errors and orders for the negatively charged channel. . . .	67
Table 4.4	Numerical errors and orders for the bipolar channel.	68
Table 1	Centimeter-Gram-Second system of units	102
Table 2	Gaussian units	102
Table 3	Positions and charges of all atomic charges in the negatively charged channel.	105
Table 4	Positions and charges of all atomic charges in the bipolar channel. . .	106
Table 5	Positions and charges of all atomic charges in the double well channel.	107

LIST OF FIGURES

Figure 2.1	An illustration of the computational domain Ω consisting of Ω_m and Ω_s . (a) For the MET channel prototype, the domain is divided into four regions: channel protein, membrane layers, bulk regions and channel pore. Here, the red circle represents the blocker, a charged atom, for channel gating effect and the arrow indicates the direction of its movement. (b) For the ionic diffusive nanofluidic channel, the ion inclusion region Ω_s is composed of two reservoirs and the inside of the cylindrical channel with a static boundary. Here, red circles indicate the charged atoms around the channel to generate channel surface charge effect.	27
Figure 3.1	An illustration of the MET channel model consisting of GA channel protein, the artificial membrane, and a positive ion which presents the gating effect.	43
Figure 3.2	Electrostatic potential profiles at different locations x_b of the blocker with charge $Q = 2e_c$ when $C^0 = 0.1\text{M}$ and $\Phi^0 = 0.1\text{V}$. The region between two dashed lines indicates the channel pore region. As the blocker position gets closer to 0.9\AA along the x -direction, the blocker produces a stronger barrier near the channel mouth as shown in the electrostatic potential profile.	48
Figure 3.3	Electrostatic potential profiles along the channel direction for the MET prototype (a) at different bulk ion concentrations $C^0 = 0.1\text{M}$ (circles) and $C^0 = 0.2\text{M}$ (diamonds) under the fixed applied voltage $\Phi^0 = 0.1\text{V}$ and (b) at different applied external voltages $\Phi^0 = 0.1\text{V}$ (circles) and $\Phi^0 = 0.2\text{V}$ (diamonds) under the fixed bulk concentration $C^0 = 0.1\text{M}$. In both investigations, we locate the blocker at $x_b = 0.9\text{\AA}$ and set the blocker charge as $Q = 2e_c$. Increase either in the bulk concentration or in the external voltage creates higher potential within the channel.	49
Figure 3.4	The total current versus the relative displacement d_x of the charged blocker. (a) Total current behavior under two bulk ion concentrations $C^0 = 0.1\text{M}$ (circles) and $C^0 = 0.2\text{M}$ (diamonds) when $Q = 2e_c$ and $\Phi^0 = 0.1\text{V}$ are fixed. (b) Total current behavior under two external voltages $\Phi^0 = 0.1\text{V}$ (circles) and $\Phi^0 = 0.2\text{V}$ (diamonds) when $Q = 2e_c$ and $C^0 = 0.1\text{M}$ are fixed. Consequently, increase either in bulk ion concentration or in external voltage induces increase in channel current. 50	50

Figure 3.5	(a) Electrostatic potential profiles and (b) total current profiles for four different charges $Q = 0.5e_c$ (triangles), $Q = 1e_c$ (diamonds), $Q = 1.5e_c$ (squares) and $Q = 2e_c$ (circles) when $C^0 = 0.1\text{M}$ and $\Phi^0 = 0.1\text{V}$ are fixed. The region between two dashed lines indicates the channel pore region in (a). As the blocker charge gets increased, the barrier at the gate of the channel gets higher. In conclusion, the amplitude of the current curve also gets enlarged.	51
Figure 3.6	Open probability P_O is plotted against the relative displacement d_x under four different atomic charges $Q = 0.5e_c$ (triangles), $Q = 1e_c$ (diamonds), $Q = 1.5e_c$ (squares) and $Q = 2e_c$ (circles) where $C^0 = 0.1\text{M}$ and $\Phi^0 = 0.1\text{V}$ are set. The solid dots are experimental data of the normalized MET current versus normalized rat hair bundle displacement obtained from the literature [123]. At each blocker charge, the open probability in response to the relative displacement forms a sigmoidal shape and, especially, the charge $Q = 2e_c$ gives a remarkable agreement with the experimental result.	53
Figure 3.7	Sensitivity test of the molecular level MET model for the prediction of open-closed probability according to the relative blocker displacement when (a) the bulk ion concentration is doubled; (b) the applied external voltage is doubled. Both cases are fairly consistent with the experimental finding [123].	54
Figure 4.1	Illustration of a nanofluidic system geometry. (a) A 3D view of a schematic cylindrical nanochannel whose ends are connected to two reservoirs of KCl solution. (b) A 2D cross-section view of the cylindrical channel whose diameter is 10\AA and length is 49\AA in the xz -plane. Here, Φ_L^0 and Φ_R^0 , respectively, represent the external voltage applied at the left and right electrodes, and C^0 represents the bulk ion concentration of both K^+ and Cl^- in two reservoirs.	57
Figure 4.2	Illustration of atomic charge distribution. (a) A 2D cross-section view and (b) a 3D view of schematic diagram consisting of the cylindrical channel and four atomic charges which are equally placed around the nanochannel at $z = 0\text{\AA}$	58
Figure 4.3	Illustration of the geometries of two simple numerical test cases. . .	62
Figure 4.4	Surface plot of electrostatic potential profiles on (a) a negatively charged channel and (b) a bipolar channel. As represented in the color bar, blue colors represent negative values, while red colors represent positive values. The negatively charged channel surface is mostly blue, but the color of the bipolar channel surface is changed from red to blue.	64

Figure 4.5	Three contour plots of electrostatic potential through the negatively charged channel at $z = -10$, $z = 0$ and $z = 10$ on the xy -plane when the mesh size is $h = 0.2$. The blue colors just outside the channel imply the negative surface charge.	66
Figure 4.6	Three contour plots of electrostatic potential through the bipolar channel at $z = -10$, $z = 0$ and $z = 10$ on the xy -plane when the mesh size is $h = 0.2$. As indicated in the color bar, blue colors represent negative values, while red colors represent some small positive values. At the cross section of $z = -10$ the inside of the channel is blue (i.e., negatively charged solution), whereas at the cross section of $z = 10$ the inside of the channel is red (i.e., slightly positively charged solution). 67	
Figure 4.7	Effect of applied voltage on electrostatics and dynamics through the negatively charged nanofluidic channel. (a) Electrostatic potential profiles and (b) ion concentration distributions along the channel length (z -axis). Here $\Delta\Phi$ is varied from 0V (squares), 0.2V (triangles), 0.4V (asterisks), 0.6V (diamonds), 0.8V (circles) to 1V (plus signs), where $\Delta\Phi$ is the difference of the applied voltage between two electrodes. Each surface atomic charge is $Q_k = -0.08e_c$ and bulk concentration is $C^0 = 0.05\text{M}$. Two dashed vertical lines indicate the ends of the nanochannel. As the applied voltage difference gets larger, the potential at the right part of the inner channel is increased. Consequently, more K^+ ions (dashed line) are accumulated at the left part of the inner channel. However, there is little change in the concentration of Cl^- ion (solid line).	70
Figure 4.8	Ionic current for each ion species versus the applied potential difference $\Delta\Phi$ through (a) the uncharged nanochannel ($Q_k = 0e_c$) and (b) the negatively charged nanochannel ($Q_k = -0.08e_c$). Here, the bulk ion concentrations at both reservoirs are fixed at $C^0 = 0.05\text{M}$. When $Q_k = 0e_c$, both current-voltage graphs are linear and the positive current (squares) is roughly double of the negative current (triangles). When $Q_k = -0.08e_c$, the positive current-voltage graph (squares) is nonlinear and the negative current-voltage graph (triangles) is almost always zero.	71

Figure 4.9	Effect of atomic surface charge on ionic current through the negatively charged nanochannel. The ionic currents in response to the change of the atomic charge Q_k are depicted. Six different charges $Q_k = 0e_c$, $Q_k = -0.02e_c$, $Q_k = -0.04e_c$, $Q_k = -0.06e_c$, $Q_k = -0.08e_c$ and $Q_k = -0.1e_c$ are simulated under the fixed bulk concentration $C^0 = 0.05\text{M}$ and applied voltage difference $\Delta\Phi = 1\text{V}$. Herein, $ Q_k $ is the magnitude of the charge of the each atom. Stronger atomic charges amplify the K^+ current (squares) sharply, but reduce the Cl^- current (triangles) to near zero.	73
Figure 4.10	Effect of bulk ion concentration on total current through the negatively charged nanochannel. The graphs of total channel current against the external voltage difference (I-V) are shown at five different bulk concentrations $C^0 = 0.01\text{M}$ (squares), $C^0 = 0.05\text{M}$ (triangles), $C^0 = 0.1\text{M}$ (diamonds), $C^0 = 0.2\text{M}$ (circles) and $C^0 = 0.4\text{M}$ (plus signs) when $Q_k = -0.08e_c$. As the bulk ion concentration is increased, the total current gets higher and, moreover, the I-V characteristic becomes near linear.	74
Figure 4.11	The effect of bulk ion concentration on the normalized current through the negatively charged nanochannel. (a) The normalized ionic current and (b) the normalized channel current with respect to the increase in bulk ion concentration when the atomic charge $Q_k = -0.08e_c$ and the applied voltage difference $\Delta\Phi = 1\text{V}$ are fixed. The negatively charged channel with a sufficiently larger bulk ion concentration behaves like a uncharged channel because the normalized values becomes one. . .	75
Figure 4.12	(a) Electrostatic and (b) ion concentration profiles of the bipolar nanofluidic channel along the channel axis at (i) no bias $\Delta\Phi = 0\text{V}$, (ii) forward bias $\Delta\Phi = 1\text{V}$ and (iii) reverse bias $\Delta\Phi = -1\text{V}$. Fix the bulk ion concentration $C^0 = 0.1\text{M}$ and the atomic surface charges $ Q_k = 0.08e_c$	77
Figure 4.13	Ionic current versus applied voltage difference in the bipolar nanofluidic channel. The atomic charge $ Q_k = 0.08e_c$ and the bulk ion concentration $C^0 = 0.1\text{M}$ are assumed. Under reverse bias, both ion species cannot pass through the channel. However, under forward bias, the currents of both ion species get enlarged. Especially, the cation current (squares) increases faster.	79

Figure 4.14	Effect of atomic surface charge on the current through the bipolar nanofluidic channel. Three sets of atomic charges, that is, $ Q_k = 0.04e_c$ (squares), $ Q_k = 0.08e_c$ (triangles) and $ Q_k = 0.12e_c$ (diamonds), are studied. Here, the bulk ion concentration C^0 is fixed at 0.1M. All I-V curves increase when $\Delta\Phi$ varies from $-1V$ to $1V$. Greater magnitude of the atomic charge results in a higher channel current with forward bias, but insufficient atomic charge may generate a current leakage because it weakens the depletion zone with reverse bias.	80
Figure 4.15	Effect of bulk ion concentration on the channel current through the bipolar nanofluidic channel. Three sets of bulk ion concentrations, such as $C^0 = 0.05M$ (squares), $C^0 = 0.1M$ (triangles) and $C^0 = 0.2M$ (diamonds), are explored in terms of the current-voltage relation. The atomic charges are given by $ Q_k = 0.08e_c$. As the bulk ion concentration gets higher, the amplitude and gradient of the current-voltage relationship gets maximized.	81
Figure 4.16	The schematic diagram of a three-dimensional double-well nanofluidic channel. The channel length is divided into three parts. The first and last parts are negatively charged, but the middle part is positively charged. The red dots indicate atoms with negative charge $Q_k = -0.12e_c$ and the green dots indicate atoms with positive charge $Q_k = 0.04e_c$	82
Figure 4.17	Effect of applied voltage on electrostatics and dynamics through the double-well nanofluidic channel. (a) Electrostatic potential profiles and (b) ion concentration distributions along the channel length (z -axis). Here $\Delta\Phi$ is varied from $0V$ (squares), $-0.2V$ (triangles), $-0.4V$ (asterisks), $-0.6V$ (diamonds), $-0.8V$ (circles) to $-1V$ (plus signs), where $\Delta\Phi$ is the difference of the applied voltage between two ends of the system. The bulk concentration is $C^0 = 0.05M$ for both ions K^+ and Cl^- . Two dashed vertical lines indicate the ends of the cylindrical channel. Each electrostatic potential graph shows two potential wells, which brings about two piles of K^+ ions along the channel axis. Moreover, higher applied voltage at the left end of the system, Φ_L^0 , breaks the symmetry of the potential wells. The left well becomes weaker and the right well becomes stronger.	83

Figure 4.18	Effect of bulk ion concentration on the channel current through the double-well nanofluidic channel. The graphs of total channel current against the external voltage difference (I-V) are studied at four different bulk concentrations: $C^0 = 0.01\text{M}$ (squares), $C^0 = 0.05\text{M}$ (triangles), $C^0 = 0.1\text{M}$ (diamonds), and $C^0 = 0.2\text{M}$ (circles). Higher bulk ion concentration encourages the total current to increase and the I-V characteristic to become linear.	84
Figure 1	An illustration of the MIB method for an irregular geometry. The k th grid line intersects the interface at (x_i, y_o, z_k) (star), which involves two irregular points (circle) (x_i, y_j, z_k) and (x_i, y_{j+1}, z_k) . Here (x_i, y_o, z_{k+2}) and (x_i, y_o, z_{k+1}) (square) are two auxiliary points needed to discretize $(\epsilon\tilde{\Phi}_z)_z$ and (x_{i-1}, y_o, z_k) and (x_{i-2}, y_o, z_k) (square) are two auxiliary points needed to discretize $(\epsilon\tilde{\Phi}_x)_x$. The other points (triangle) indicate the points selected to interpolate $\tilde{\Phi}$ along the y -grid lines at (x_i, y_o, z_k) , (x_i, y_o, z_{k+1}) and (x_i, y_o, z_{k+2})	97
Figure 2	Flowchart of the numerical implementation to solve the standard PNP system	100

Chapter 1

Introduction

1.1 Introduction to mechanoelectrical transducer channel in auditory system

Ion channels are pore-forming membrane proteins which are very permeable and highly selective and their opening and closing are suitably managed [112]. Ion channels are involved in diverse physiological functions including altering membrane potentials, controlling electrolyte movements for cell volume regulation and polarized transport of salt, and generating electrical signals which are utilized to regulate hormone secretion, neurotransmitter release and muscle contraction [94]. Traditionally, ion channels are classified and named by their two crucial properties such as ion selectivity and gating mechanism [94, 98]. Most channels allow only a few specific ions to penetrate through them although there are exceptions like non-selective cation channels and, in particular, potassium, sodium, calcium and chloride are four principal permeable ions. The gating mechanism of an ion channel is classified according to a particular stimulus which the channel gate react strongly. Typical kinds of stimuli are the voltage gradient across the transmembrane (voltage-gated), the binding and interaction of ligands with an ion channel (ligand-gated) and a mechanical force (mechanically-gated). Besides, other ways to gate ion channels can be triggered by photonic and thermal stimuli.

The mechanoelectrical transducer (MET) channel in hair cells is one of the remarkable ion

channel research subjects. Hair cells in the inner ear play a pivotal role in the mechanotransduction for the sense of hearing. Mechanotransduction is the conversion of a mechanical stimulus into an electrical signal, which is fundamental for the senses of hearing, touch and balance [88]. The peripheral auditory system, the sensory system for hearing, is mainly divided into three parts: the outer, middle and inner ear [21]. A wide range of airborne sound waves enters the external canal of the outer ear and through the middle ear they are converted to pressure waves which vibrate the basilar membrane in the cochlea of the inner ear [159]. In the cochlea, basilar membrane vibrations deflect the stereociliary bundles on the hair cells and hence the sensory cells are depolarized by allowing cations, predominantly Ca^{2+} , to penetrate into the mechanoelectrical transducer (MET) channels [88].

The human cochlea contains three rows of outer hair cells (OHCs) and one row of inner hair cell (IHC) with different functions and shapes [175]. OHCs amplify the amplitude as well as the frequency selectivity of basilar membrane vibrations. IHCs convey acoustic information to afferent neurons [78, 121]. Each hair cell possess a mechanically sensitive bundle consisting of a number of actin-filled microvilli, also named stereocilia, on its apical surface [159]. The stereocilia in a bundle are arranged in rows of increasing height and, moreover, they are tightly connected to each other by extracellular linkages including tip links and top-connectors [175]. In particular, it is speculated that the tip link, which extends from the tip of a stereocilium to the side of an adjacent taller stereocilium, directly opens the mechanically gated ion channels [121, 175]. Additionally, it is postulated that an elusive elastic element, a so-called gating spring, contributes to unfasten the channel inlet [121].

The biophysical principles underlying the mechanotransduction process in hair cells have been intensively investigated in the past few decades. The recently proposed model of activation and adaptation of the hair cell transducer channel is composed of three stages

[121]. It is postulated that deflection of a hair bundle toward the tallest stereocilia, namely positive deflection, increases the open probability of the MET channel at the lower end of the tip link. Then Ca^{2+} ions travel through the channel pore and then contribute to fast adaptation by binding to a molecule inside or near the channel. Finally, slow adaptation including channel closure and tension restoration is accomplished by a myosin motor at the upper end of the tip link. Despite these advances in MET channel study, the molecular detail of the mechanotransducer machinery has been proved to be elusive. Particularly, there is no direct structural confirmation for the molecular building blocks of the MET channel.

There have been several studies to elucidate the features of the MET channel such as gating mechanism, ion conductance, molecular-level structure and location because characterizing the channel is beneficial to comprehend not only hair cell transducer process but also hearing mechanism [77]. First of all, the MET channel is a non-selective cation channel with a considerably high permeability of Ca^{2+} [156]. Then many empirical experiments have been focused on the localization of this mechanosensitive channel, which is essential to validate that the channel is gated by mechanical stimuli [62, 109]. Especially, Beurg *et al.* established that the MET channels were located only at the bottom of the tip links as indicated by fast confocal calcium-imaging [16]. In spite of these findings, the MET channel is a notable example of ion channels whose molecular nature is still obscure, partly due to few channels per hair cell and few hair cells per organ [159]. Although various potential candidates including any known mechanosensitive channels and transient receptor potential channels were compared with the MET channel from biophysical perspectives in the literature, none of them was perfectly matched with the MET channel [77, 159]. However, Ricci *et al.* showed that the conductance of hair cells in the turtle cochlea was tonotopically changed with their characteristic frequency, which implies that the MET channel might be composed of several

subunits [165]. Farris and his colleagues measured the dimensions of the MET channel using various antagonists of the candidate channel classes and simple amine compounds [74]. Then they found that the minimal pore size was about 12Å and channel length was approximately 31Å [74]. More intrinsic characteristics of the MET channel are yet to be discovered in order to construct its molecular components.

1.2 Introduction to nanofluidic channels

Nanofluidics, one of the most vibrant scientific research fields, refers to the study and application of the transport of molecules and/or ions dissolved in a solution as well as fluid behavior through or past structures with one or more nanometer dimensions [55, 172]. The nanofluidic studies have been highly motivated by the efforts to design a solid-state DNA separation system and, moreover, extensive research has been driven by the dramatic advance in both nanofabrication techniques and theoretical tools to describe fluid motion on the nanoscale [188]. Another impetus is the discovery of new mechanical and electrochemical phenomena which are non-existent or less influential in macrofluidic or microfluidic systems [188]. In a nanofluidic channel, the combination of the remarkably large surface-to-volume ratio, the electrostatic interactions between the fluid and the charged wall, and the channel's characteristic dimension comparable with the size of biomolecules generate unique transport patterns such as double-layer overlap, ion-current rectification, ion permittivity and diffusion [68, 223].

The extraordinary transport features of nanofluidics have been received a great deal of attention in chemistry, physics, biology, material science, medicine and several engineering fields [172]. In particular, the design and fabrication of nanofluidic devices for molecular

biology applications is a new interdisciplinary field that takes advantage of precise control and manipulation of fluids at submicrometer and nanometer scales in order to study the behavior of molecular and biological systems. Nanofabrication techniques are generally classified into two groups: top-down and bottom-up methods [151, 160]. The top-down method creates patterns on a large scale with nanometer lateral dimensions, while the bottom-up method places the atoms and molecules in nanostructures by using chemical reactions. Sophisticatedly synthesized nanochannels are applied to biosensing of high-throughput, regulating and separating ions and molecules and energy harvesting [93]. As the characteristic length scale of the fluid is comparable with the length scale of the biomolecule and/or the Debye length, nanofluidics can be applied to a variety of interesting powerful tools for genomics or proteomics [1, 154]. For example, Han *et al.* introduced an entropic trapping sieving mechanism for long DNA molecules [95] and Fu *et al.* designed and investigated a patterned anisotropic nanofluidic sieving structure for size-based separation of DNA and proteins as well as electrostatic separation of proteins [82]. For a protein analysis, nanofilter is used to maximize protein concentration in a sample [204]. Schoch and his colleagues demonstrated a pH-controlled diffusional separation of proteins in a nano-scaled channel [171]. Besides, nanofluidic techniques have been instrumented for macromolecule accumulator [44, 210], electronic circuits [116, 118, 215], local charge inversion [96], photonic crystal circuits [73] and nanofluidic dynamic array [202]. Despite rapid development in nanotechnology, it is still an intriguing challenge for engineers to generate inexpensive nanostructures which are more feasible in diverse areas, for example biomedical research [154]. Since nanofluidic device prototyping and fabrication are technically challenging and financially expensive, it is desirable to further advance the field by mathematical/theoretical modeling and simulation.

One major factor to characterize a nanofluidic system is its structure. The novel nanofab-

rication skills enable the production of diverse nanofluidic devices from 0, 1 to 2 dimensions, where the dimension indicates the number of non-nanometer length component of the device [68]. Generally, 0-D, 1-D, and 2-D nanochannels are also called as nanopores, nanotubes, and nanoslits, respectively. Another parameter to represent the structure is the ratio of channel height to width, namely the aspect ratio (AR), and, especially, low AR and near-unity AR channels are referred to as planar and square channels [1]. Nanopores are usually formed perpendicularly through diverse substrate materials, and the most well-known nanopore sensors are pore-forming proteins such as α -hemolysin and silicon nitride membranes with solid-state pores [196, 223]. Nanopore-based sensing is a cost-effective label-free approach without amplification at a relatively high speed and it has been promoted to meet the needs of researchers interested in DNA sequencing [22, 196]. Kasianowicz and his group tried to detect single-stranded RNA and DNA molecules using α -hemolysin [120] and Li *et al.* designed a set of solid-state nanopores in a silicon nitride to observe the folding behavior of individual double-stranded DNA [134]. Nanochannels whose depth and/or width are reduced to the nanoscale are eligible to combine with other sophisticated devices and to demonstrate the transport inside the channel [223]. For example, Perry and his colleagues designed funnel-shape nanofluidic channels with different taper angles and proved that the taper angle of the funnel influenced the ion-rectifying effect [161]. Typically, nanochannels with comparatively longer lateral length have either a cylindrical or a conical geometry [223]. While surface charge and applied external potential predominantly control the counterion current in a cylindrical channel, the flow direction is also critical to determine the ion conductance patterns through a conical channel. In the work presented here, we will concentrate more on nanofluidic channels.

The other important property that distinguishes a nanofluidic system from a higher

dimensional fluid system is its unprecedented transport phenomena. The fluid transport through a nanoscale channel is explained by three factors: the external driving force generated by either an electrical potential gradient or a pressure gradient, a variety of molecular-level interactions, and the friction forces caused by solvent-wall interactions and hydrodynamic solute-wall interactions [188]. Due to the extraordinary surface-to-volume ratio in nanofluidic systems, fluid interactions with the wall dominantly induce notable transport behaviors including ion permselectivity, ion enrichment and depletion, fast mixing and rapid injection of a small amount of reagent [162]. Especially, steric/hydration interactions, van der Waals interactions and electrostatic interactions play a central role in nanofluidic systems and these intermolecular interactions determine the characteristic length scale of nanofluidics [55]. The interactions within a nanoscale fluid system are mostly influenced by its physical and chemical properties such as geometrical confinement and charge, and flow condition such as ion composition and concentration. Consequently, microscopic interactions dominate the solute and solvent transport in nanofluidic structures, but continuum fluid mechanics regulate it in macrofluidic and microfluidic structures.

Electrostatic distribution in a solution and electrokinetic flow of the solute molecules are fundamental concepts to understand the transport in nanofluidic devices [172]. Specifically, the surface charge of the channel wall plays a pivotal role to derive electrostatic interactions and electrokinetic effects within nanoscale fluidic channels when charged particles are sufficiently adjacent to the wall [56, 173, 190, 218]. The fixed charge at the channel wall induces electrostatic interactions with ions dissolved in a solution; hence the wall attracts oppositely charged ions, but repels ions with the same charge [188]. The interplay between the long-range electrostatic forces and short-range van der Waals forces creates a screening region, so-called an electrical double layer (EDL), in an electrolyte solution confined to the nanostructure so

that this oppositely charged region is able to attain electroneutrality at the interface between the solid and the liquid [172]. The combination effect between two forces at the charged solid-liquid interface is well-established by the Derjaguin-Landau-Verwey-Overbeek (DLVO) theory [63, 197]. The structure of the EDL is described well in the Gouy-Chapman-Stern model, which suggests three layers of the EDL: the inner Helmholtz plane, outer Helmholtz plane and diffuse layer [172]. While the inner Helmholtz plane consists of non-hydrated coions and counterions that are attached to the channel surface, the outer Helmholtz plane contains bound, hydrated and partially hydrated counterions. Moreover, the part between the inner and outer Helmholtz planes is called the Stern layer, where the charge and potential are linearly varied. The diffuse layer, the farthest layer, contains mobile coions and counterions. In particular, a thorough understanding of the potential variance in accordance with the structure of the EDL is indispensable because the principal mechanism of the transport is electrokinetic behavior [162]. The readers can refer to the literature [6, 91, 157] for a more comprehensive understanding of the EDL.

Characteristic length scale, such as Reynolds number, Biot number and Nusselt number, is a reference quantity used to explain particular characteristics in a physical system. For example, Reynolds number, the ratio of inertial forces to viscous ones, is a dimensionless number to determine flow patterns in fluidic mechanics [105]. One of the most representative characteristic length scales in nanofluidic structures is the Debye length $\lambda_D = \sqrt{\frac{\varepsilon\varepsilon_0 k_B T}{\sum_{\alpha} C_{\alpha}^0 q_{\alpha}^2}}$, where ε is the dielectric constant of the solvent, ε_0 is the permittivity of vacuum, k_B is the Boltzmann constant, T is the absolute temperature, and C_{α}^0 and q_{α} are, respectively, the bulk ion concentration and the charge of ion species α [55]. The Debye length only depends on the flow conditions, including the solute composition and concentration, and also describes the

thickness (or, precisely, $\frac{1}{e}$ th reduction) of the EDL where the potential decays exponentially [172]. Essentially, ionic fluid behaves like a microscopic flow within the EDL region, but it acts as a macroscopic flow far beyond the Debye length.

When the internal diameter of a nanochannel is comparable to or smaller than the Debye length, the electrolyte solution becomes a unipolar solution with a charge of sign opposite to the channel surface charge [55]. However, this unipolar transport never occurs in microfluidic systems because the channel pore is much larger than the Debye length. If the EDLs are overlapped across the channel pore dimension, only the control of counterion flow is possible, but otherwise the flow of both counterions and coions can be governed [56]. Ion selectivity is another important feature which enables nano-sized channels to work as an ionic filter and it is defined as the ratio of the difference between currents of cations and anions to the total current delivered by both ions [199]. Vlasiouk and his group examined the ion selectivity of single nanometer channels under various conditions including channel dimension, buffer concentration and applied voltage.

The rectification of ionic current in nanofluidic devices has been of great interest because it is possible to control the ionic flow by simple electrical switches [41]. This asymmetry in ion conductance can be derived by applying the external voltage when the symmetry of surface charge distribution, bulk concentration, channel geometry or a combination of these is broken along the longitudinal axis [41]. In order to interpret the rectification phenomena through nanofluidic systems, several experiments and theoretical modeling have been performed in various types of structures. For example, Pu *et al.* conducted experiments to observe ion-enrichment and ion-depletion effects in 60-nm-deep nanochannels, which usually resulted in the ion-current rectification [163]. In their design, an applied field gave rise to accumulation of both cations and anions at the cathode and absence of all ions at the anode of the channels.

Siwy and her colleagues showed the rectification phenomena in a single conical nanopore and in a single conical nanotube when the surface was adequately charged [184, 183, 180, 181, 182]. Karnik *et al.* designed a cylindrical nanofluidic diode with uneven surface charge distribution [117] and Daiguji *et al.* theoretically described the ionic transport through such channels [56].

1.3 Review of current computational models

Channels with nanoscale pores are ubiquitous in biological systems, while recently astonishing advance in synthesis techniques enables manufacturing such small-sized pore channels for various applications[153]. Modeling and analyzing the ionic transport and fluidic dynamics through both natural and artificial nanofluidic channels have been a great challenge and a crucial task over the past few decades. Membrane channels are obviously different from solid-state channels. For instance, the ionic selectivity of membrane channels is mainly based on the sizes of ions and channel pore; in contrast, that of solid-state channels depends on electrostatic effects [55]. In spite of such differences, ion transport through both types of nanochannels can be simulated using similar theoretical and computational tools due to common physical features.

An enormous number of theoretical approaches, from phenomenological to fundamental, have been proposed and developed in order to elucidate the transport phenomena within cell membrane channels as well as man-made channels [46, 55, 112, 133, 146, 153, 168]. In this section, we account for three well-known representative theoretical approaches: all-atom molecular dynamics (MD), stochastic dynamics and continuum models such as Poisson-Boltzmann (PB) and Poisson-Nernst-Planck (PNP) equations. Then we discuss the history

of modeling biological ion channels and introduce several theoretical models and simulations of ion channels using each model in the literature. Finally, we summarize a list of modeling and simulation of synthetic nanofluidic channels.

1.3.1 Three representative computational approaches

1.3.1.1 Molecular dynamics

In the MD simulation, the dynamical motions of all the atoms, including ions, water, protein and lipid in the simulated system, are described via Newton’s second law of motion, and the empirical force fields express the potential energy under the influence of interatomic interactions [153].

$$m_i \frac{d^2}{dt^2} \mathbf{r}_i(t) = \mathbf{F}_i(t) = -\nabla V(\mathbf{r}_i(t), \dots, \mathbf{r}_N(t)),$$

where \mathbf{r}_i and m_i denote, respectively, the position and the mass of the atom i , N the total number of atoms in the system and \mathbf{F}_i the force acting on the atom i that is the gradient of the potential energy $V(\mathbf{r}_i(t), \dots, \mathbf{r}_N(t))$.

The potential energy is composed of bonded potential and unbonded potential [146]. While the former is related to bond lengths, bond angles, improper dihedral angles and torsional angles, the latter contains the Coulomb potential for electrostatic interactions and the Lennard-Jones potential for van der Waals interactions. The widely used molecular dynamics simulation packages with a set of force fields are CHARMM [23, 143], AMBER [51, 209], GROMOS [97], and OPLS-AA [113].

The greatest advantage of the MD simulation is to give the most accurate time-dependent atomic detail of the system of interest which is also comparable with experimental data [146]. In this respect, it is a powerful theoretical approach for biophysical and biochemical

analysis. Especially, the MD calculates a valuable parameter, the potential of mean force (PMF). It is very beneficial to discover the permeation through nanometer pores or channels and, moreover, it can provide the selectivity sequences of monovalent cations using the free-energy profiles [48]. Despite such great benefits, the MD has several limitations: the high computational cost due to microscopic detailedness of description, the wide range of time scales from femtoseconds over milliseconds to seconds, the difficulty to account for polarization and pH value, and the difficulty to apply an electrostatic potential across the system [153]. The abrupt advance of computer powers raises the time scales of simulation up to 1 microsecond [125]. *Ab initio* MD framework has progressed to analyze the polarization effects in biomolecular systems and, for instance, these simulations successfully demonstrate dissociation of NaCl in water [148, 192]. Many studies have purported to surmount the other puzzling issue of the availability of the external electrostatic potential in MD simulations [153]. Since Aksimentiev and Schulten simulated the ion conductance through α -Hemolysin under the applied external electrostatic field [4], a similar investigation method has been utilized to study ion transport in a variety of systems [20, 126, 145, 152, 179, 174].

1.3.1.2 Stochastic dynamics

The stochastic dynamics scheme is proposed as a great compromise between two computational approaches in that it can simulate only a reasonable number of ions explicitly by considering the solvent molecules implicitly [55]. The simplest and most commonly used form of stochastic dynamics to explore complex many-body systems is the Brownian dynamics (BD) [48]. Specifically, for the BD simulations of nanofluidic channels, the dynamics depict the behavior of each solute ion while considering the channel as a rigid structure and the solvent molecules implicitly under frictional and stochastic forces [146]. By reducing the number of degrees of

freedom in calculation, this statistical approach provides very useful computational data such as current-voltage and conductance-concentration curves at a relatively lower cost [48, 153]. Herein, the Langevin equation is repeatedly solved to detect the random motions of the individual ions of interest under the influence of the dissipative and fluctuating forces [48]:

$$m_i \frac{d^2}{dt^2} \mathbf{r}_i(t) = \mathbf{F}_i(t, \mathbf{r}) - m_i \gamma_i \dot{\mathbf{r}}_i(t) - \xi_i(t),$$

where \mathbf{F}_i denotes the systematic force including electrostatic forces derived from interactions between the charged atoms, $m_i \gamma_i \dot{\mathbf{r}}_i(t)$ the frictional force denoting m_i the mass, γ_i the reciprocal of the relaxation time and $\dot{\mathbf{r}}_i$ the velocity, and ξ_i the stochastic force. Two necessary parameters required to conduct a BD simulation are the diffusion coefficient for each ion and the force applied to each ion which corresponds to the multi-ion PMF [146]. These two factors are usually obtained from all-atom MD simulations.

In particular, the BD simulations are very valuable for ion channel studies in that they empower to calculate the current flow and ionic concentrations in the system using a trajectory analysis and to determine the valence selectivity [48]. Although the BD somewhat compensates the defects of both the MD and the continuum approaches, this framework also has critical shortcomings and hence many scholars have extensively researched solutions to such problems [48, 146, 153]. The stochastic dynamics of the reduced system involves two major simplifications assuming water as a continuum and protein as a fixed structure, which are closely involved in the shortcomings of the simulations [133]. Another weakness of the BD method is using the position-independent dielectric constant for water, but the MD demonstrates that the polarizability of water is decreased due to confinement in a real system [48]. Thus, some BD simulations use position-dependent dielectric constants validated by

MD simulations [107, 131]. For ion channel analysis, the conformational changes of proteins may have influence on ion permeation, which needs to be discovered using experiments and MD simulations and, further, to be applied in BD simulations [48].

The dynamic Monte Carlo (DMC) is an alternative statistical theory to simulate non-equilibrium or relaxation systems [169]. The fundamental principle of the DMC is that the dynamics of a system can be described by a sequence of states generated by random particle displacements in time [54, 169]. In this simulation, a randomly-chosen ion of an arbitrary species is transferred to a randomly-chosen new location within a maximum displacement of its former location [54]. Csényi *et al.* satisfactorily computed ionic current through a sodium channel model under nearly physiological bulk ion concentration [54]. A theoretical approach coupling grand canonical Monte Carlo (GCMC) and Brownian dynamics (BD) is proposed by Roux and his colleagues in order to incorporate bulk ion concentration and transmembrane potential in ion channel microscopic simulations [107, 108]. They validated the proposed algorithm to study ion permeation and selectivity of the OmpF porin of *Escherichia coli*.

1.3.1.3 Continuum models

In a continuum based simulation, the mathematical theory treats all the components of a system of interest including ions, water and proteins as a continuous element [48]. The most well-established continuum models are Poisson-Boltzmann (PB) for electrostatics and Poisson-Nernst-Planck (PNP) for ion transport [146]. Due to such simplifying approximation, the continuum approach has a number of limitations; however, it plays a crucial role to predict structural and physical features from the current-voltage-concentration relation at high computational efficiency [146].

In the early 1900s, the PB equation was first proposed by Gouy (1910) and Chapman (1913)

in order to elucidate electrostatic patterns around a biomolecule [29, 90]. It is generalized as a continuum approach to compute electrostatic free energy of small spherical ions in an ionic solution by Debye and Hückel in solution chemistry [61]. Since such worthwhile usage of the PB equation in electrochemistry, this model has been studied and applied in various research fields as well [139]. For example, it is the foundation of DLVO theory which describes electrostatic effects in colloid systems [63, 197] and, moreover, it is also utilized in biophysics [59, 103]. The non-linear PB equation is usually written in the following form:

$$-\nabla \cdot (\epsilon(\mathbf{r}) \nabla \Phi(\mathbf{r})) = 4\pi \rho_m(\mathbf{r}) + 4\pi \lambda(\mathbf{r}) \sum_{\alpha} q_{\alpha} C_{\alpha}^0 \exp \left(\frac{-q_{\alpha} \Phi(\mathbf{r})}{k_B T} \right),$$

where $\epsilon(\mathbf{r})$ denotes the spatial-dependent dielectric constant, $\Phi(\mathbf{r})$ the electrostatic potential and $\rho_m(\mathbf{r})$ the fixed charge density of the biomolecule. For each mobile ion species α within an aqueous solution, C_{α}^0 and q_{α} represent, respectively, the concentration at bulk region and the charge. Moreover, k_B is the Boltzmann constant, T is the absolute temperature, and $\lambda(\mathbf{r})$ is the characteristic function whose value is 1 in the solvent region which ions can penetrate through, but whose value is 0 in the biomolecule region impermeable to ions.

The fundamental assumption of the PB model is that the electrostatic potential in an ionic solution is determined by the Boltzmann distribution of solute charges [81, 146]. The PB equation is largely solved to compute the electrostatic potential at the solvent-accessible molecular surface, the reaction rates between molecules in a solution, the free energy of biomolecular association and its salt dependence and pKa shifts in proteins [81]. Furthermore, it can be conveniently integrated into molecular mechanics and dynamics to maximize computational efficiency [81]. Since the PB is involved with a mean-field approximation, the PB modeling produces several weaknesses [26]. First, the important properties of an

ion, such as the size and the discrete surface charge, are not considered while the ion is simply considered as a point charge. Second, the non-electrostatic ion-ion interactions and ion-solid interactions are ignored. Third, the dielectric constant of the solvent is assumed to be the same through the system, but in reality the permittivity of the medium can be altered due to charge distribution near the surface. Such problems notwithstanding, the PB framework is definitely a useful tool in ion channel studies in that it facilitates the calculation of the free energy required to move an ion from the bulk region to the channel inside, the characterization of ion-channel interactions and the description of transmembrane electrostatic potential distribution [146].

The utmost remarkable continuum theory for ion transport through a nanofluidic channel is an electrodiffusion model, namely Poisson-Nernst-Planck (PNP) theory, which treats both solutes and solvent as continuous entities, but describes membrane protein in atomic detail. Specifically, the PNP model describes the solvent water molecule as a dielectric continuum, treats ion species by continuum density distributions and, in principle, retains the discrete atomic detail and/or charge distribution of the channel or pore constitution [14, 72, 129, 221, 220]. The Nernst-Planck equation (NP) combines two fundamental physical laws, that is, Ohm's law and Fick's law, based on the fact that the flux of ions through a nanochannel is driven by the potential and concentration gradients [48]. For each solvent ion species α ,

$$\mathbf{J}_\alpha(\mathbf{r}) = -D_\alpha(\mathbf{r}) \left(\nabla C_\alpha(\mathbf{r}) + \frac{C_\alpha(\mathbf{r})}{k_B T} \nabla (q_\alpha \Phi(\mathbf{r}) + U_\alpha(\mathbf{r})) \right),$$

with the Boltzmann constant k_B and the absolute temperature T . Herein, $\mathbf{J}_\alpha(\mathbf{r})$, $D_\alpha(\mathbf{r})$, $C_\alpha(\mathbf{r})$, q_α and $U_\alpha(\mathbf{r})$ are, respectively, the flux density, the diffusion coefficient, the concentration, the charge valence and the sum of potentials induced from interactions with the

channel for ion species α . Additionally, the electrostatic potential $\Phi(\mathbf{r})$ is obtained from the Poisson equation:

$$-\nabla \cdot (\epsilon(\mathbf{r}) \nabla \Phi(\mathbf{r})) = 4\pi \rho_m(\mathbf{r}) + 4\pi \sum_{\alpha} q_{\alpha} C_{\alpha}(\mathbf{r}),$$

where $\epsilon(\mathbf{r})$ and $\rho_m(\mathbf{r})$ are the position-dependent dielectric constant and the partial charge density of the nanopore, respectively. By solving the NP and Poisson equations self-consistently and simultaneously, one can calculate the electrostatic potential, the ionic concentration and the ionic currents [153]. To simulate the PNP model with a nanofluidic channel, the required parameters need to be gained empirically or, sometimes, by all-atom simulations [48, 153]. The parameters include the channel geometry and its surface charge composition, the dimension and bulk ion concentration at each reservoir, the dielectric constant at each region, the diffusion coefficients of an ion species and the applied external potential [48]. Although the PNP theory is proved to analyze and predict ion transport at a comparably small computational cost, it is similar with the PB theory in its limitations. In particular, the PNP theory is inadequate to describe the transport phenomena through narrow nanochannels owing to the finite size effects of the ions [114] and short-range non-electrostatic interactions [52].

The Poisson-Nernst-Planck theory, combined with the density functional theory, is a useful extension of the PNP model [86, 87]. In this framework, ions are considered as charged rigid spheres and the density functional theory is employed to calculate the chemical potential of the ions. Other potent theoretical tools are Poisson-Boltzmann-Nernst-Planck (PBNP), which simplifies the calculation for multiple ion species with Boltzmann distributions of ion concentrations [140, 221] and variational multiscale models for charge transport, which employ diverse variational formulations based on differential geometry theory [208].

1.3.2 Modeling and simulation of biological ion channels

In 1952, Hodgkin and Huxley designed a voltage clamp experiment technique which is used to determine the membrane permeability [100]. Using this brilliant idea, they elucidated the action potential in squid giant axons by analyzing electrical movements of Na^+ and K^+ through the ion channels [99]. Similarly, early studies on ion channels were biophysical experiments to study conductance by measuring voltage and current [19]. Then the understanding of ion channels at molecular level have been expanded by structural studies [19]. For example, electron microscopy, nuclear magnetic resonance (NMR) spectroscopy and X-ray crystallography have been established to reveal atomic-level structural information of ion channels [112]. The discovery of the crystallized structure of the *Streptomyces lividans* KcsA potassium channel by MacKinnon and his collaborators was a remarkable achievement, which also helps to understand the ion conductance mechanism at atomic basis [67, 144]. As another good example of the well-studied ion channel structure, the pore and channel molecular structures of a Gramicidin A (GA) channel have been explored by X-ray crystallographic and/or NMR spectroscopic methods [201]. The molecular structures of other potassium channels [135], mechanosensitive channels [9, 28] and a chloride channel [69] have been discovered. Therefore, the abrupt advance in crystallographic analysis gives rise to atomic-resolution structures of many ion channels [48]. The detected structures are used to identify their functions from the essential laws of physics in electrolyte solutions [48].

Parallel to progress in experimental methods, theoretical tools have been so sophisticated that researchers could investigate structure, function, dynamics and transport of ion channels in electrophysiology, biochemistry, molecular biology, computational chemistry and bioinformatics from the whole cell studies to single channel studies [112]. Theoretical

modeling is beneficial to obtain an overall physical description of an ion channel, which gives several advantages [46, 168]. First of all, it is very effective not only to organize and visualize experimental data but also to predict physical phenomena. Moreover, it possibly provides a connection between the structure of an ion channel and its functions. A number of theoretical frameworks have been proposed and developed to answer the following puzzling issues: the detailed process of ion permeation, the positions of binding sites in a channel, the rate-limiting steps in conduction, and the relationship between the molecular composition of an ion channel and its ion selectivity [153]. Powerful computational approaches including all-atom molecular dynamics (MD), Brownian dynamics (BD), Poisson-Boltzmann (PB) model, Poisson-Nernst-Planck (PNP) model, Poisson-Boltzmann-Nernst-Planck (PBNP) model and variational multiscale models have been established over years to explore ion channels [112, 146, 153]. Each method has strengths and weaknesses, so a researcher should choose an appropriate method by considering the computational complexity and cost [146].

MD, a dynamic description of the detailed motions of individual atoms in a system, has been developed to deal with more complex biological or chemical systems [5, 119, 149]. Since the first simulation of a folded globular protein, its usage has been extended to account for dynamic conformational changes and longer time scales [5, 119, 149]. Mackay and his coworkers applied MD method to observe the transport of four ions (lithium, sodium, potassium, and cesium) through the GA channel, which was the first MD simulation of an ion channel [142]. Especially, this theoretical approach elucidates the mechanism of ion selectivity, for instance, water permeation through human aquaporin-1 [60] and Ca^{2+} permeation through an L-type calcium channel [7]. BD describes the ions of interest explicitly, but it treats the solvent molecules implicitly [146]. Chung *et al.* performed BD simulations to study currents of sodium and chloride ions through the designed membrane channel

whose structure is similar to ACh channel [47]. PB is an equilibrium approach beneficial to describe the electrostatics around charged biomolecules in a solution, while PNP is a nonequilibrium approach useful to explore the ion fluxes depending on concentration gradient and electrostatic potential gradient [146]. Due to high efficiency of computational cost, PNP has been applied to study diverse ion channels including GA channel [31, 49, 101, 129] and OmpF porin [3, 107]. Zheng and her colleagues suggested PBNP model in order to simplify the calculations of Nernst-Planck equations and tested that model with two protein molecules such as cytochrome c551 and GA [221].

Recently, a variety of differential geometry based multiscale models were introduced for charge transport by our group [207, 208, 206]. The differential geometry theory of the molecular surface provides a natural means to separate the microscopic domain of biomolecules from the macroscopic domain of solvent so that appropriate physical laws are applied to appropriate domains. Our variational formulation is able to efficiently bridge macro-micro scales and synergically couple macro-micro domains [206]. One type of our multiscale models is the combination of Laplace-Beltrami (LB) equation, PB equation and Kohn-Sham equations to study the molecular mechanism of proton transport [30, 33]. Another type incorporates LB equation into the generalized PNP equations for the dynamics and transport of ion channels and transmembrane transporters [208, 206]. The other type alternates MD simulations and continuum elasticity (CE) descriptions of the solute molecule as well as continuum fluid mechanics formulation of the solvent [207, 208, 206, 213]. We proposed the theory of continuum elasticity with atomic rigidity (CEWAR) to treat the shear modulus as a continuous function of atomic rigidity so that the dynamics complexity of a macromolecular system is separated from its static complexity [213]. As a consequence, the time-consuming dynamics is approximated by the CE theory, while the less time-consuming static analysis is

carried out in atomic level. Efficient geometric modeling strategies associated with differential geometry based multiscale models have been carried out with both Lagrangian Eulerian [75, 76] and Eulerian representations [212].

1.3.3 Modeling and simulation of synthetic nanofluidic channels

Nanofluidics has been extensively studied in chemistry, physics, biology, material science, and many areas of engineering [172]. The modeling and simulation of nanofluidic systems have been of enormous importance and a fast growing research field in the past decade. Basically, modeling a fluidic system with one or more dimensions at nanoscale is different from modeling a microfluidic system in that the liquid confined to such a narrow system contains fewer molecules and the wall considerably influences on the transport [189]. Thus the simulation models utilized in microfluidic systems need to be carefully tested if each model is applicable in nanofluidic analysis [189]. Most microfluidic devices involve a fluid flow through a microfluidic pore or channel, which has been an interesting concern in the theoretical modeling. Gad-al-Hak classified the fluidics models as two categories: continuum models including Euler, Navier-Stokes (NS) and Burnett equations, and molecular models including molecular dynamics (MD), direct simulation Monte Carlo (DSMC) and lattice-Boltzmann method (LBM) [83]. The characteristic length scales such as Reynolds number and Debye Screening length are key factors to explore the transport features in nanofluidics as well as microfluidics [55, 105]. Especially, for a nanofluidic device, if the characteristic length scale of its pore is greater than 5nm, the PNP equations and Stokes equations well describe electrokinetics and liquid flow within the device, respectively [55, 189]. Otherwise, the transport analysis requires the discreteness of substances; thus, in particular, MD is an efficient tool in this respect [55].

In every fluidic system, the transport behavior is determined by the forces between the individual atoms, which implies that considering all the atomic interactions is the best way to depict fluid mechanics [70]. In spite of several critical limitations such as time scale, MD is the foremost modeling tool to study the structural and dynamic characteristics of nanoscale devices [55]. For nanofluidic analysis, MD simulations have been employed to discover significant dynamics phenomena such as ion current rectification and charge inversion in various types of solid-state nanochannels [153]. Lyden-Bell *et al.* designed a simple cylindrical channel model to investigate the mobility and solvation of ions and uncharged molecules in an aqueous solution [141]. This study found the solvation shell of water molecules by means of the MD simulations. All-atom molecular dynamics simulations have been performed to delineate the ionic transport and several remarkable phenomena within silica devices [153]. Lorenz *et al.* investigated ζ -potential, Stern layer conductance, charge inversion and ionic mobilities using a detailed description of ionic transport, electro-osmotic flow and streaming currents [136, 137]. Curz-Chu *et al.* demonstrated the effect of ion-binding spots at the silica surface on the ionic current rectification [53]. Moreover, Shirono and his colleagues successfully provided a atomic-scale description of ionic transport within ultra-narrow silica nanopores with 2nm diameter pore [178]. Although MD is a powerful theoretical approach, it is inadequate to examine a dilute fluid because the intermolecular interactions have little influence and hence alternative theoretical approaches are mandatory [105]. For example, a lattice-Boltzmann method (LBM) based on mesoscopic kinetic equations with microscopic models has been advanced to simulate not only microfluidic systems but also nanofluidic systems [37, 105].

The Navier-Stokes (NS) equations have been a famous continuum dynamics model to elucidate microfluidic phenomena in lap-on-a-chip systems at comparatively less computational

cost and its simpler version is the Stokes equations [105]. The Navier-Stokes/Stokes equations have been coupled with various other equations such as PB equations for electrokinetic flow dynamics and PNP equations for ion transport analysis [105]. Especially, the PNP is the most renowned model for charge transport in nanofluidics [14, 27, 57, 71]. Daiguji and his coworkers intensively characterized a variety of transport phenomena through nanofluidic channels including unipolar solution, energy conversion and ionic rectifying effect by coupling the NS equations with the PNP equations [57, 58, 56]. Choi *et al.* investigated the electrokinetic flow-induced currents through silica nanofluidic channels using the performances of the PB and PNP models with appropriate boundary conditions [43]. They also validated the proposed models by comparing with experimental data. The BD simulation of ions in a nanopore channel was combined with the continuum PNP model for regions away from the nanopore channel [2]. A further simplified model is the Lippmann-Young equation, which is able to predict the liquid-solid interface contact angle and interface morphology under an external electric field [186].

1.4 Existing challenges

1.4.1 Existing challenges in mechanoelectrical transducer channel

Mechanosensitive channel is one of the most famous targets of computational studies, but the molecular mechanism of mechanosensation is still elusive [146]. For only few simple mechanosensitive channels, their crystal structures were discovered and they have been studied to elucidate ion conductance and the mechanism of mechanical gating using simulations [9, 28, 187, 191]. Since the transduction process of hair cells attracted a great deal of

attention, many principal physiological properties of a hair cell mechanotransducer have been demonstrated [79]. These features contain exceptional sensitivity to a mechanical force, kinetic principles such as activation and adaptation, ion selectivity, and conductance of a single MET channel. Especially, the channel permeation properties are critical foundations to build its molecular building blocks [158]. However, the molecular identity of the MET channel is not confirmed yet because it is fairly formidable to connect properly its physiological functions to intrinsic cytoarchitecture and accessory proteins [158]. Parallel to this difficulty, there are two obscure, but essential, questions - whether the transducer channel is activated by mechanical stimuli through accessory proteins or by the deformation change in the lipid bilayer and which part of the channel protein calcium ions bind to for fast adaptation [79]. It is one of the most challenging as well as indispensable works to complete the molecular structure of the MET channel, which will provide more substantial understanding of the transduction process in hearing.

1.4.2 Existing challenges in nanofluidics

Nanofluidics has been intensively and extensively developed not only in terms of fabrication skills but also in terms of theoretical studies over the past decades. In nanofluidic modeling, computation and analysis, there are many standing theoretical and technical problems. For example, nanofluidic processes may induce structural modifications and even chemical reactions [115, 195], which are not described in the present nanofluidic simulations. The PNP model, one of the most widely used theories in nanofluidics, can incorporate atomic charge details in its pore or channel description, which are vital to channel gating and fluid behavior. However, atomic charge details beyond the coarse description of surface charge are usually neglected in most nanofluidic simulations. Although Stern layer and ion steric

effect are significant for the EDL as discussed earlier, they are not appropriately described in the conventional PNP model. Furthermore, nanofluidic simulations have been hardly performed in three dimensional realistic settings with physical parameters. Consequently, simulation results can only be used for qualitative (i.e., phenomenological) comparison and not for quantitative prediction. Finally, the material interface induced jump conditions in the Poisson equation are seldom enforced in nanofluidic simulations with realistic geometries. Therefore, it is imperative to address these issues in the current nanofluidic modeling and simulation.

Chapter 2

Theoretical models and mathematical algorithms

This chapter contributes to derive a generalized Poisson-Nernst-Planck (PNP) model using a variational formulation in order to describe the ion transport within not only a biological ion channel but also a synthetic nanopore channel. In this model, we consider van der Waals interactions as part of our free energy functional to describe solvent-solute and ion-ion non-electrostatic interactions. Then we develop Dirichlet to Neumann mapping (DNM) for dealing with charge singularities and the matched interface and boundary (MIB) method for material interfaces in order to compute the PNP equations with 3D irregular channel geometries and singular charges.

2.1 Generalized Poisson-Nernst-Planck (PNP) model

Although the PNP theory is quite standard to describe the dynamics within nanochannels [14, 35, 36, 45, 50, 110, 194, 199, 200, 203, 206, 222, 225], it does not include non-electrostatic interactions. In this section, we present a generalized PNP theory by incorporating non-electrostatic interactions between the solution and the nanoscale channel pore, and between solvent molecules such as waters and ions. We utilize a variational formulation to derive generalized PNP equations.

2.1.1 Computational domain

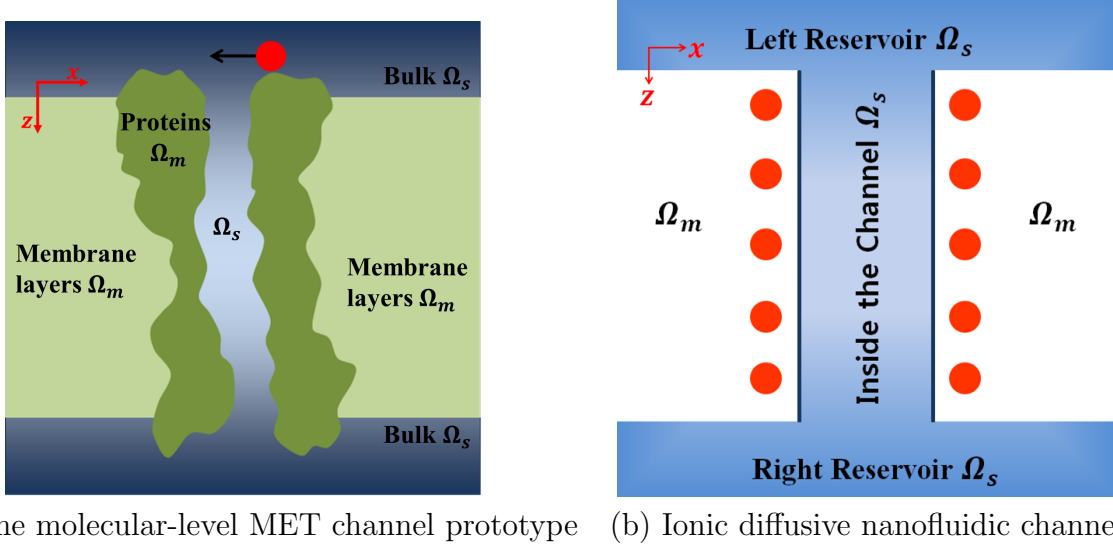


Figure 2.1: An illustration of the computational domain Ω consisting of Ω_m and Ω_s . (a) For the MET channel prototype, the domain is divided into four regions: channel protein, membrane layers, bulk regions and channel pore. Here, the red circle represents the blocker, a charged atom, for channel gating effect and the arrow indicates the direction of its movement. (b) For the ionic diffusive nanofluidic channel, the ion inclusion region Ω_s is composed of two reservoirs and the inside of the cylindrical channel with a static boundary. Here, red circles indicate the charged atoms around the channel to generate channel surface charge effect.

Let us consider a total computational domain $\Omega \subset \mathbb{R}^3$. We denote Ω_m and Ω_s respectively the microscopic channel region (or the ion exclusion region) and the solution region (or the ion inclusion region). Essentially, we seek continuum descriptions of ions in the solution domain Ω_s , while we consider a discrete atomistic description in the channel structure domain Ω_m . Interface Γ separates two regions Ω_m and Ω_s so that $\Omega_m \cup \Gamma \cup \Omega_s = \Omega$. Since biological channels and artificial channels differ in the specific composition of the domain Ω , the domain setting is a careful process. Moreover, it is critical, not simple, to determine a well-defined interface because it is related to the structural features of the channel.

In this work, we simulate two nano-scaled systems: the molecular prototype for the MET channel and the ionic diffusive nanofluidic channels with atomic surface charge. In the

following, we will discuss in detail about the computational domain for each channel type.

Biological ion channel domain setting

As depicted in Fig. 2.1(a), the molecule region Ω_m consists of channel proteins and membrane layers, but the solvent region Ω_s is composed of channel pore and bulk regions which ions and molecules travel through. Since in reality, the shape of a protein channel continuously varies, for example by its interactions with water molecules, identifying a static structure has been a puzzling issue in a theoretical modeling of a complex macromolecule [166]. The molecular surface (MS) is one of the standard methods to visualize the molecule-solvent interface [166, 170]. The minimal molecular surface (MMS) is proposed in order to minimize the surface free energy [10, 11]. To describe the boundary of our MET prototype, we employ the hypersurface function $S : \mathbb{R}^3 \rightarrow \mathbb{R}$ from our earlier differential geometry based multiscale models [207, 208, 206]. Basically, the function $S(\mathbf{r})$ is a solvent-solute characteristic function whose value is 1 in Ω_s and 0 in Ω_m , whereas it takes proper values between 0 and 1 near the boundary of the biomolecule to become a smooth function [206]. Thus, the hypersurface function determines movable biomolecule-solvent interface whose dynamics is driven by mechanical and electrostatic forces, for example using the Laplace-Beltrami equation [208]. With this hypersurface function $S(\mathbf{r})$, we can derive a generalized PNP model using the differential geometry formalism of solvent-solute interface as in [206].

Synthetic nanofluidic channel domain setting

In solid-state channel analysis, the region Ω_s is divided into the channel inside and two reservoirs as in Fig. 2.1(b). Usually, an external field leads ions and molecules to pass through the channel inside from one reservoir to another. Herein, we introduce a domain

characteristic function $\mathcal{S} : \mathbb{R}^3 \rightarrow \mathbb{R}$ such that $\Omega_m = \mathcal{S}\Omega$ and $\Omega_s = (1 - \mathcal{S})\Omega$. Obviously, \mathcal{S} and $(1 - \mathcal{S})$ are the indicators for the channel domain and the solution domain, respectively. Unlike the charge and material transport in biomolecular systems, the charge and material transport in nanofluidic systems induces a negligible reconstruction of the solid-fluid interface compared to the system scale. Therefore, the fixed solid-fluid interface is predetermined in the present model as opposed to using the hypersurface function $S(\mathbf{r})$ in ion channel model. With this domain characteristic function $\mathcal{S}(\mathbf{r})$, we present a new variational derivation of the PNP model for the solid-state nanofluidic channel in this thesis work.

2.1.2 Energy functional

Generally, a nanochannel, which can be either biological or artificial, system is mainly composed of an ionic solution and a microscopic channel composition. Inter-particle correlations occur between components of the solution or between the solution component and the channel component at the channel surface. These interactions are mainly classified to be either electrostatic or non-electrostatic.

Electrostatic energy functional

Electrostatic interactions are ubiquitous in all biomolecular systems and processes, and are also the dominating effects for nanofluidic behaviors [55, 81]. Especially, electrostatic interactions in biomolecules are salient to elucidate the several behaviors such as folding, binding, conformational stability and enzyme activity [155]. The electrostatic interactions are typically modeled by a number of theoretical approaches: the Poisson-Boltzmann (PB) theory [59, 81, 130, 177], the polarizable continuum solvation theory [150, 193] and the generalized Born model, an approximate continuum solvent model, [8, 66]. Among these methods, the PB

theory is the most popular in structural and functional analysis of biomolecules. A variation formulation of this theory was originally introduced by Sharp and Honig in 1990 [176], and was extended to a multiscale formalism [207, 206] as well as an electrostatic force derivation [89].

In the present work, we consider the following electrostatic energy functional

$$G_{\text{electr}} = \int \left\{ \chi \left[-\frac{\epsilon_m}{2} |\nabla \Phi|^2 + \Phi \rho_m \right] + (1 - \chi) \left[-\frac{\epsilon_s}{2} |\nabla \Phi|^2 + \Phi \sum_{\alpha=1}^{N_s} q_\alpha C_\alpha \right] \right\} d\mathbf{r}, \quad (2.1)$$

where Φ is the electrostatic potential, and ϵ_s and ϵ_m are the dielectric constants of the ionic solution and channel regions, respectively. $\rho_m = \sum_{k=1}^{N_m} Q_k \delta(\mathbf{r} - \mathbf{r}_k)$ with Q_k denoting the partial atomic charge at position \mathbf{r}_k and N_m the total number of fixed charges on the channel surface. For each ion species α , C_α and q_α , respectively, represent the concentration and the charge valence which is zero for an uncharged solution component, and N_s represents the number of mobile ion species in the solution domain. Moreover, the function $\chi(\mathbf{r})$ in Eq.(2.1) is the characteristic function to determine the channel-solution interface. This characteristic function means the hypersurface function $S(\mathbf{r})$ for membrane channel modeling, but the domain characteristic function $\mathcal{S}(\mathbf{r})$ for solid-state channel modeling.

Non-electrostatic interactions

The examples of non-electrostatic interactions are van der Waals interactions, dispersion interactions, ion-water dipolar interactions, ion-water cluster formation or dissociation, steric effects, and so forth. In particular, these interactions near the solution-channel interface have a crucial influence on the transport features due to confinement or dilution of solution; however, continuum approaches ignore such important correlations [12, 26, 52, 114]. This

simplification may result in problematic discrepancy between simulation predictions and experimental data and hence the extensions of continuum models including non-electrostatic correlations have been explored. For example, the PB and PNP, two representative continuum based theories, have been studied in terms of ionic finite size effects in the past [13, 12, 24, 30, 92, 106, 127, 132, 198].

To account for solvent-channel interactions as well as solvent-solvent interactions, the non-electrostatic interaction energy functional takes the form

$$G_{\text{non-electr}} = \int_{\Omega_s} U d\mathbf{r} = \int_{\Omega} (1 - \chi) U d\mathbf{r}. \quad (2.2)$$

In this modeling, we assume that the aqueous environment has multiple ion species labeled by α . The non-electrostatic interaction potential U can be obtained by summing all the pairwise inter-particle interactions within the solution or near the solution-channel interface:

$$U(\mathbf{r}) = \sum_{\alpha} C_{\alpha}(\mathbf{r}) U_{\alpha}(\mathbf{r}) = \sum_k C_{\alpha}(\mathbf{r}) U_{\alpha k}(\mathbf{r}) + \sum_{\beta} C_{\alpha}(\mathbf{r}) U_{\alpha\beta}(\mathbf{r}), \quad (2.3)$$

where $C_{\alpha}(\mathbf{r})$ is the density of α th ionic component of the solution, which may be either charged or uncharged, and U_{α} is a non-electrostatic interaction potential with α th species. For each α , $U_{\alpha k}(\mathbf{r})$ is an interaction potential with the k th atom of the channel structure and $U_{\alpha\beta}(\mathbf{r})$ is a potential for ion-ion or ion-water non-electrostatic interactions with β th component of the solution.

The solvent-solute interactions in solvation analysis have been represented by the Lennard-Jones (LJ) potential [40, 38, 39]. The Weeks-Chandler-Andersen (WCA) decomposition [205]

was utilized to split the LJ potential into attractive and repulsive parts [39, 208]

$$\begin{aligned} U_{\alpha k}^{\text{att,WCA}}(\mathbf{r}) &= \begin{cases} -\bar{\epsilon}_{\alpha k}, & 0 < \|\mathbf{r} - \mathbf{r}_k\| < \sigma_k + \sigma_\alpha, \\ V_{\alpha k}^{\text{LJ}}, & \|\mathbf{r} - \mathbf{r}_k\| \geq \sigma_k + \sigma_\alpha, \quad \text{and} \end{cases} \\ U_{\alpha k}^{\text{rep,WCA}}(\mathbf{r}) &= \begin{cases} V_{\alpha k}^{\text{LJ}} + \bar{\epsilon}_{\alpha k}, & 0 < \|\mathbf{r} - \mathbf{r}_k\| < \sigma_k + \sigma_\alpha, \\ 0, & \|\mathbf{r} - \mathbf{r}_k\| \geq \sigma_k + \sigma_\alpha, \end{cases} \end{aligned} \quad (2.4)$$

where $\bar{\epsilon}_{\alpha k}$ is the depth of the potential well, σ_k and σ_α are respectively the radii of the k th atom in the channel region and the α th ion species in the solvent region, and \mathbf{r}_k represents the location of the k th atom in the channel. For the MET channel analysis, \mathbf{r}_k represents the position of the partial charge of the channel protein; however, for the ionic diffusive channel analysis, \mathbf{r}_k represents that of the atomic surface charge. Here, $V_{\alpha k}^{\text{LJ}} = 4\bar{\epsilon}_{\alpha k} \left\{ \left(\frac{\sigma}{r_d} \right)^{12} - \left(\frac{\sigma}{r_d} \right)^6 \right\}$ represents the Lennard-Jones potential for the interaction between the k th atom in the channel region and the α th ion species in the solvent region with denoting σ the distance at which the interaction potential is zero and r_d the distance between two particles.

The inter-particle interaction term $U_{\alpha\beta}(\mathbf{r})$ within the solution does not affect the derivation and the form of other expressions. More detailed description of $U_{\alpha\beta}(\mathbf{r})$ for ion channel transport can be found in our earlier work [33, 208].

Chemical potential related free energy

Chemical potential related free energy combines a reference homogeneous term and an entropic term of mobile charges [80], which is essential for the description of mobile charges

in the nanofluidic system.

$$G_{\text{chem}} = \sum_{\alpha=1}^{N_s} \int \left\{ \left(\mu_{\alpha}^0 - \mu_{\alpha 0} \right) C_{\alpha} + k_B T C_{\alpha} \ln \left(\frac{C_{\alpha}}{C_{\alpha 0}} \right) - k_B T (C_{\alpha} - C_{\alpha 0}) \right\} d\mathbf{r}, \quad (2.5)$$

where k_B is the Boltzmann constant and T is the temperature. For each α th species, $\mu_{\alpha 0}$ is a relative reference chemical potential which implies the difference between the equilibrium concentrations of different solvent species. μ_{α}^0 and $C_{\alpha 0}$, respectively, represent a reference chemical potential and its associated ion concentration, given that $\Phi = U_{\alpha} = \mu_{\alpha 0} = 0$. Especially, the term $k_B T C_{\alpha} \ln \left(\frac{C_{\alpha}}{C_{\alpha 0}} \right)$ is the entropy of mixing and the term $-k_B T (C_{\alpha} - C_{\alpha 0})$ is a relative osmotic term [147].

For each species α , it is standard that the variation of the energy G_{chem} with respect to C_{α} , namely, $\frac{\delta G_{\text{chem}}}{\delta C_{\alpha}}$, generates the chemical potential as follows [208].

$$\mu_{\alpha}^{\text{chem}} = \mu_{\alpha}^0 - \mu_{\alpha 0} + k_B T \ln \left(\frac{C_{\alpha}}{C_{\alpha 0}} \right). \quad (2.6)$$

Note that, at equilibrium, $\mu_{\alpha}^{\text{chem}}$ is nontrivial, and C_{α} and $C_{\alpha 0}$ are not equal due to possible external electrical potentials, solvent-solute interactions, and charged particles.

Total free energy functional

The total free energy functional for the nanofluidic system is

$$\begin{aligned}
G_{\text{total}}^{\text{PNP}}[\chi, \Phi, \{C_\alpha\}] &= \int \left\{ \left[\chi \left(-\frac{\epsilon_m}{2} |\nabla \Phi|^2 + \Phi \rho_m \right) + (1 - \chi) \left(-\frac{\epsilon_s}{2} |\nabla \Phi|^2 + \Phi \sum_{\alpha=1}^{N_s} q_\alpha C_\alpha \right) \right] \right. \\
&\quad + (1 - \chi) \sum_{\alpha=1}^{N_s} C_\alpha U_\alpha \\
&\quad \left. + (1 - \chi) \sum_{\alpha=1}^{N_s} \left[\left(\mu_\alpha^0 - \mu_{\alpha 0} \right) C_\alpha + k_B T C_\alpha \ln \left(\frac{C_\alpha}{C_{\alpha 0}} \right) - k_B T (C_\alpha - C_{\alpha 0}) + \lambda_\alpha C_\alpha \right] \right\} \text{dr.}
\end{aligned} \tag{2.7}$$

This shows three contributions to the total free energy: the electrostatic free energy including both fixed and mobile charges, the free energy of non-electrostatic interactions, and the chemical potential related energy. Note that the electrostatic free energy functional is the same as the polar solvation free energy functional in the literature [38, 39, 206]. Here λ_α is a Lagrange multiplier, which is included to ensure appropriate physical properties at equilibrium [80].

A powerful feature of the present total free energy function formulation (2.7) is to employ the free energy functional of the non-electrostatic interactions U for nanofluidic dynamics. Therefore, the present theory is able to deal with a variety of non-electrostatic interactions and the solvent microstructure near the channel can be predicted correctly as well.

2.1.3 Governing equations

The total free energy functional (2.7) is a function of electrostatic potential Φ and ion concentration C_α . The governing equations for this thesis work are derived by using the

variational principles [207, 208, 206].

Generalized Poisson equation

The variation of the total free energy functional (2.7) with respect to the electrostatic potential Φ results in the classical Poisson equation

$$-\nabla \cdot (\epsilon(\mathbf{r}) \nabla \Phi(\mathbf{r})) = \chi(\mathbf{r}) \sum_{k=1}^{N_m} Q_k \delta(\mathbf{r} - \mathbf{r}_k) + (1 - \chi(\mathbf{r})) \sum_{\alpha=1}^{N_s} q_\alpha C_\alpha(\mathbf{r}), \quad \mathbf{r} \in \Omega, \quad (2.8)$$

where $\epsilon(\mathbf{r}) = \chi(\mathbf{r})\epsilon_m + (1 - \chi(\mathbf{r}))\epsilon_s$ is the dielectric profile whose value is ϵ_m in the channel domain Ω_m and ϵ_s in the solution domain Ω_s . On the right-hand side, the first term accounts for the fixed charge density of the channel and the second term represents the mobile charge density within the solution. Due to the characteristic function $\chi(\mathbf{r})$, the Poisson equation (2.8) can be split into two equations

$$-\nabla \cdot (\epsilon_m \nabla \Phi(\mathbf{r})) = \sum_{k=1}^{N_m} Q_k \delta(\mathbf{r} - \mathbf{r}_k), \quad \mathbf{r} \in \Omega_m \quad (2.9)$$

$$-\nabla \cdot (\epsilon_s \nabla \Phi(\mathbf{r})) = \sum_{\alpha=1}^{N_s} q_\alpha C_\alpha(\mathbf{r}), \quad \mathbf{r} \in \Omega_s. \quad (2.10)$$

Since the electrostatic potential $\Phi(\mathbf{r})$ is defined on the whole computational domain Ω , the following jump conditions at the solution-channel interface Γ are to be implemented to ensure the well-posedness of the generalized Poisson equation [85, 102, 217].

$$[\Phi(\mathbf{r})] = \Phi^m(\mathbf{r}) - \Phi^s(\mathbf{r}) = 0 \quad (2.11)$$

$$[\epsilon(\mathbf{r}) \nabla \Phi(\mathbf{r})] \cdot \mathbf{n} = \epsilon_m \nabla \Phi^m(\mathbf{r}) \cdot \mathbf{n} - \epsilon_s \nabla \Phi^s(\mathbf{r}) \cdot \mathbf{n} = 0, \quad (2.12)$$

where \mathbf{n} is the outward unit norm of the interface Γ . In Eq. (2.8), the densities of ions C_α should be determined by the variational principle for the generalized Nernst-Planck equation in the following subsection.

The boundary conditions of Eq. (2.8) are typically mixed boundary conditions depending on experimental settings. In our numerical experiments, we use the Dirichlet boundary condition $\Phi(\mathbf{r}) = \Phi^0$ on $\partial\Omega$ and the Neumann boundary condition in other types of boundaries, where Φ^0 is the external voltage applied at electrodes. However, the boundary conditions except the applied voltages are somewhat irrelevant as long as boundaries are sufficiently far from the channel pore [220, 221].

Generalized Nernst-Planck equation

For each ion species α , we can derive the relative generalized potential μ_α^{gen} by the variation of the total free energy functional $G_{\text{total}}^{\text{PNP}}$ with respect to the ion density C_α , that is, $\frac{\delta G_{\text{total}}^{\text{PNP}}}{\delta C_\alpha}$,

$$\begin{aligned}\mu_\alpha^{\text{gen}} &= \mu_\alpha^0 - \mu_{\alpha 0} + k_B T \ln \left(\frac{C_\alpha}{C_{\alpha 0}} \right) + q_\alpha \Phi + U_\alpha + \lambda_\alpha \\ &= \mu_\alpha^{\text{chem}} + q_\alpha \Phi + U_\alpha + \lambda_\alpha.\end{aligned}\tag{2.13}$$

At equilibrium, we require not μ_α^{chem} but μ_α^{gen} to vanish, which results in

$$\lambda_\alpha = -\mu_\alpha^0 \quad \text{and} \quad C_\alpha = C_{\alpha 0} \exp \left(-\frac{q_\alpha \Phi + U_\alpha - \mu_{\alpha 0}}{k_B T} \right).\tag{2.14}$$

Consequently, the relative generalized potential μ_α^{gen} is simplified as

$$\mu_\alpha^{\text{gen}} = k_B T \ln \left(\frac{C_\alpha}{C_{\alpha 0}} \right) + q_\alpha \Phi + U_\alpha - \mu_{\alpha 0}.\tag{2.15}$$

We derived a similar quantity from a slightly different perspective in our earlier work [221]. It is interesting to note that the relative generalized potential μ_α^{gen} consists of contributions from the entropy of mixing, the electrostatic potential, the non-electrostatic interaction with α th ion species and the position-independent relative reference chemical potential. In practice, the biological or synthetic nanopore system is out of equilibrium due to applied external field and/or inhomogeneous concentration across the nanofluidic channel, which implies that μ_α^{gen} does not vanish.

The Fick's first law generates the ion diffusive flux

$$\mathbf{J}_\alpha(\mathbf{r}) = -D_\alpha(\mathbf{r})C_\alpha(\mathbf{r})\nabla\frac{\mu_\alpha^{\text{gen}}(\mathbf{r})}{k_B T} \quad (2.16)$$

with D_α denoting the diffusion coefficient of species α and the general conservation law gives the diffusion equation

$$\frac{\partial C_\alpha(\mathbf{r})}{\partial t} = -\nabla \cdot \mathbf{J}_\alpha(\mathbf{r}) \quad (2.17)$$

[128]. Therefore, the generalized Nernst-Planck equation is

$$\frac{\partial C_\alpha(\mathbf{r})}{\partial t} = \nabla \cdot \left[D_\alpha(\mathbf{r}) \left(\nabla C_\alpha(\mathbf{r}) + \frac{C_\alpha(\mathbf{r})}{k_B T} \nabla (q_\alpha \Phi(\mathbf{r}) + U_\alpha(\mathbf{r})) \right) \right], \quad \alpha = 1, \dots, N_s, \quad (2.18)$$

where $q_\alpha \Phi + U_\alpha$ can be regarded as the potential of the mean field. At the absence of non-electrostatic interactions, Eq. (2.18) reduces to the standard Nernst-Planck equation. At the steady state, one has

$$\nabla \cdot \left[D_\alpha(\mathbf{r}) \left(\nabla C_\alpha(\mathbf{r}) + \frac{C_\alpha(\mathbf{r})}{k_B T} \nabla (q_\alpha \Phi(\mathbf{r}) + U_\alpha(\mathbf{r})) \right) \right] = 0, \quad \alpha = 1, \dots, N_s. \quad (2.19)$$

Herein, Eq. (2.18) does not involve the characteristic function χ because it has already been restricted to the solution domain Ω_s even though the generalized Poisson equation (2.8) is defined on the whole domain Ω .

Mixed boundary conditions are also applied to the generalized NP equations (2.18) for all ion species. Since the Nernst-Planck equation is only defined in the ion inclusion region Ω_s , it is enough to consider the boundary $\partial\Omega_s$. On $\partial\Omega \cap \partial\Omega_s$, $C_\alpha = C_\alpha^0$, where C_α^0 represents the bulk ion concentration for species α . However, at the interface $\Gamma = \Omega_m \cap \Omega_s$, the zero-flux condition $- \left[D_\alpha \left(\nabla C_\alpha + \frac{C_\alpha}{k_B T} \nabla (q_\alpha \Phi + U_\alpha) \right) \right] = \mathbf{0}$ is required, where $\mathbf{0} = (0, 0, 0)$ is a null vector.

2.2 Mathematical algorithms

In the present study, we only solve the standard Poisson-Nernst-Planck equations in a self-consistent manner with appropriate initial/boundary conditions. To emphasize the primary effects of atomic charges in both molecular-level prototype for MET channel and ionic diffusive nanofluidic channel design, we neglect the non-electrostatic interactions U . However, since non-electrostatic interactions are important for nanoscopic scale systems [13, 12], the situation that $U \neq 0$ will be investigated in our future work.

Moreover, it is an indispensable task to establish rigorous numerical schemes and computational algorithms in the study of realistic biological, physical, chemical and engineering problems [208]. Therefore, we employ several novel theoretical schemes to obtain more effective and reasonable calculation results from the PNP model. They are the Dirichlet-to-Neumann mapping (DNM) technique, the matched interface and boundary (MIB) method, and the successive over relaxation (SOR)-like iterative procedure

First of all, the DNM is a computational technique using the Green's function in order to remove charge singularities due to the Dirac delta function $\delta(\mathbf{r} - \mathbf{r}_k)$ in the Poisson equation (2.8) [85, 217, 221, 220]. It decomposes the electrostatic potential $\Phi(\mathbf{r})$ into the regular part $\tilde{\Phi}(\mathbf{r})$ and the singular part $\bar{\Phi}(\mathbf{r})$, which results in the following equations:

$$-\nabla \cdot (\epsilon(\mathbf{r}) \nabla \tilde{\Phi}(\mathbf{r})) = (1 - \chi(\mathbf{r})) \sum_{\alpha=1}^{N_s} q_{\alpha} C_{\alpha}(\mathbf{r}), \quad \mathbf{r} \in \Omega, \quad (2.20)$$

and

$$\begin{cases} \nabla^2 \hat{\Phi}(\mathbf{r}) = 0, \mathbf{r} \in \Omega_m \\ \hat{\Phi}(\mathbf{r}) = -\Phi^*(\mathbf{r}), \mathbf{r} \in \Gamma. \end{cases} \quad (2.21)$$

This process generates a system of equations which can be numerically well-interpolated without losing the order of accuracy. For more information, readers may refer to Section A.1.

The MIB scheme has been extensively developed to deal with discontinuous coefficients and irregular complex geometries [208, 33, 30, 84, 85, 214, 217, 216, 219, 221, 220, 224, 226]. Basically, this method uses fictitious values and auxiliary points to extend the computational domain so that the desired order of convergence is achieved [217, 216, 226, 219]. Appendix A.2 outlines the principal ideas of the MIB method and introduces the required discretization equations. The advantages of this numerical scheme are using standard finite difference method on a simple rectangular coordinate system, carrying out low order of physical jump conditions and locally reducing three dimensional interface problem to one dimensional problem [221]. The standard centered finite difference scheme is implemented to find Φ^0 from Eq (2.21) and C_{α} from Eq. (2.19) without non-electrostatic interaction term U_{α} away from the complex boundary. However, careful interpolation is required near the boundary for both equations [217, 220]. Especially, the MIB method is utilized to solve Eq. (2.20) for $\tilde{\Phi}$

with two jump conditions (2.11) and (2.12). Since these equations are coupled, an iterative procedure is required to obtain convergent results as explained in detail in Section A.3.

Chapter 3

Modeling and simulating a mechanoelectrical transducer (MET) channel in mammalian hair cells in molecular level

In this chapter, we introduce a molecular level prototype of a MET channel and computational studies to explore the mechanoelectrical gating mechanism of the MET channel in mammalian hair cells. Our channel model consists of a realistic ion channel, a membrane and an additional charged lip. Our theoretical analysis has been carried out with the standard PNP model which is able to provide channel current under various experimental conditions, such as bulk ion concentration, applied voltage, lip charge and lip position. In particular, we examine the response of total current according to lip displacement. Our results are compared with experimental data of rat hair bundle displacement and current relation given by Kennedy *et al.* [123].

The rest of this chapter is organized as follows. In Section 3.1, the structure of our molecular level prototype for the MET channel is presented. Since the molecular structure of the MET channel is unknown, an alternative channel is mandatory to design the channel

model in microscopic detail. We use the Gramicidin A (GA) ion channel (PDB ID: 1MAG) for the following reasons. First, the structure of GA is simple so that a blocker can be added with 100% confidence in the blocker’s geometry. In practice, many other channels have additional domains and complex composition, which may cause unwanted complication in the result interpretation. Second, the GA is one of the most studied realistic channels and its behaviors are well-known [220, 33, 208]. Consequently, the change in fluidic behavior through this channel can be easily attributed to the blocker effect. A particle-like lip with an adjustable charge, also called a blocker, is mounted at the mouth region of the GA channel to enable the mechanoelectrical gating of the channel. Section 3.2 introduces the preparation of the GA atomic structural data and explains a few important simulation parameters including the dielectric constants and the diffusion coefficients. Section 3.3 is devoted to the numerical study of our prototype for the MET channel. We validate our model by analyzing the electrostatic potential and current under a variety of channel conditions via the second-order PNP solver recently developed in our lab [220]. Among our computational results, open probability distributions are compared with experimental data in the literature. This chapter ends with a conclusion in Section 3.4.

3.1 A molecular level prototype of a MET channel

Howard and Hudspeth [104] proposed the original gating spring model, in which the elastic component, the so-called gating spring, regulates opening and closing of the transducer channel. Deflection of a hair bundle toward the tallest row of stereocilia increases the tension of the spring which is attached to the hypothetical channel gate. As a result, the channel attains the open state. It was assumed that the tip link acted as a gating spring in the

beginning. However, recent research findings suggest that the tip link may be too stiff to express a spring effect and thus an elastic filament may be located at the bottom of the channel [88, 122, 175]. It is still mysterious how the deflection of a hair bundle gives rise to opening the MET channels. Several possibilities have been suggested, but none of them is conclusive owing to the lack of molecular level structural information for the MET channel and insufficient experimental evidence. Moreover, the channel opening may involve not only a conformational change but also a complicated molecular interplay [159, 164].

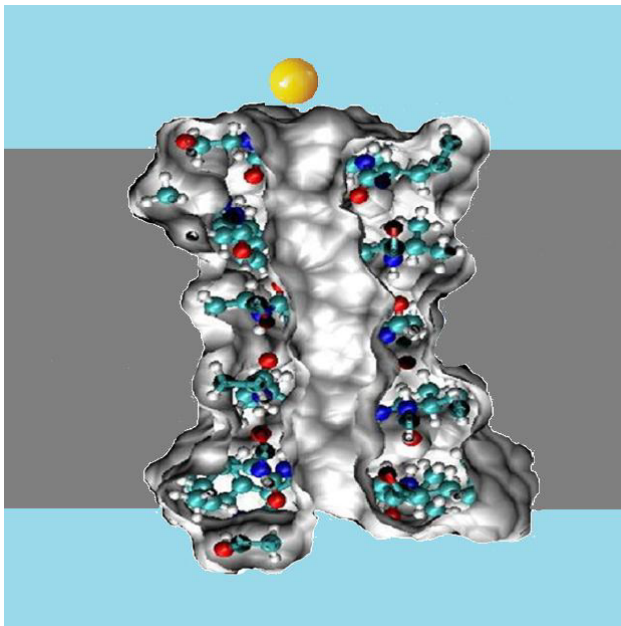


Figure 3.1: An illustration of the MET channel model consisting of GA channel protein, the artificial membrane, and a positive ion which presents the gating effect.

In this work, we design a molecular level prototype to simulate the MET channel gating process in a realistic setting. The GA channel (PDB code: 1MAG), one of the most well-studied ion channels, is employed to represent the channel structure in molecular level. A positively charged atom of radius 1.5\AA , called as a “blocker”, is placed at the mouth region of the channel so that it behaves as a lip, see Fig. 3.1. Since the GA channel is a cation channel, it can be effectively blocked by an additional cation with a pertinent charge. The

computational domain of the MET channel prototype incorporates four different regions such as channel pore, channel protein, bulk regions and membrane as in Fig. 2.1(a).

The channel pore region is placed along the z -axis. The membrane part is added to the geometry from $z = -15\text{\AA}$ to $z = 9\text{\AA}$ (See Fig. 2.1(a)). To demonstrate the blocker's gating behavior, we allow it to move along one direction just outside the channel entry. Then the displacement of the blocker imitates the deflection of a hair bundle [123]. In order to find out the optimal position of the blocker, several locations along the channel axis (z -axis) were tested; as a result, $z_b = -15.95\text{\AA}$ is selected to be the most suitable z -coordinate of the blocker. We fix the y -coordinate of the blocker at 0.1\AA and allow the blocker to move only along the x -direction from $x_b = -0.5\text{\AA}$ to $x_b = 0.9\text{\AA}$, which involves the transition between the open and closed states of the channel model. Additionally, in order to intensify the efficiency of the blocker role, we vary its charge over a certain range in our numerical experiments.

3.2 Computational setup for the PNP systems

The standard PNP model, a relatively simple and computationally inexpensive continuum model, is employed to examine our MET channel prototype, in order to optimize the computational efficiency and to focus on the gating behavior of the prototype. Our earlier work already validated that the standard PNP model simulated the GA channel at the second order accuracy using a number of advanced mathematical techniques, and the simulation prediction showed a good agreement with experimental result from the literature [220]. Further, the PNP model can incorporate with the structural detail of ion channel proteins. In the present simulation study, the molecular structural data of the GA channel with a blocker

is prepared in the procedure as described in our earlier work [220]. Specifically, for each atom in the biomolecule, its van der Waals radius is assigned with the CHARMM22 force field [143] in order to achieve a full all-atom structure. Then partial charges for the channel protein are calculated by the PDB2PQR software [64, 65], which are accounted in the fixed charge density in the Poisson equation (2.8) in our computation. However, partial charges in the membrane layers are neglected to attain a good approximation for ion transport. The molecular surface of the GA channel is generated by the MSMS program with density 10 and probe radius 1.4Å [170] to identify the channel-solvent interface Γ which separates two domains Ω_m and Ω_s .

We need to treat carefully parameters involved in the PNP equations. First, it is necessary to assign pertinent values for the dielectric constant function $\epsilon(\mathbf{r})$ because the Poisson equation (2.8) requires the spatial-dependent dielectric constant. In our computation, we set $\epsilon_m = 2$ for the biomolecular region impermeable to water or ions and $\epsilon_s = 80$ for the aqueous solution region permeable to water and simple ions. Another significant parameter is the diffusion coefficient for each ion species of interest in the solvent region. The diffusion coefficient in bulk region is different from, usually larger than, that in channel pore region. Practically, the overall diffusion coefficient distribution is intricate to be determined, but the bulk values for relatively simple biomolecules are possibly available from experiments [221]. Furthermore, the diffusion coefficient function $D_\alpha(\mathbf{r})$ should be deliberately defined to be differentiable using the buffering zone between the pore and bulk regions as discussed in our earlier work [220].

$$D_\alpha(\mathbf{r}) = \begin{cases} D_\alpha^{\text{pore}}, & \mathbf{r} \in \Omega_s^{\text{pore}} \\ D_\alpha^{\text{pore}} + \left(D_\alpha^{\text{pore}} - D_\alpha^{\text{bulk}}\right) f(\mathbf{r}), & \mathbf{r} \in \Omega_s^{\text{buffering}} \\ D_\alpha^{\text{bulk}}, & \mathbf{r} \in \Omega_s^{\text{bulk}}. \end{cases} \quad (3.1)$$

Here, the function $f(\mathbf{r})$ is defined as

$$f(\mathbf{r}) = f(z) = n \left(\frac{z - z^{\text{pore}}}{z^{\text{bulk}} - z^{\text{pore}}} \right)^{n+1} - (n+1) \left(\frac{z - z^{\text{pore}}}{z^{\text{bulk}} - z^{\text{pore}}} \right)^n, \quad z \in [z^{\text{bulk}}, z^{\text{pore}}], \quad (3.2)$$

where z^{bulk} and z^{pore} , respectively, indicate the bulk region and the channel pore region.

In our computation, we use $D_{\text{K}^+}^{\text{bulk}} = 1.96 \times 10^{-5} \text{cm}^2/\text{s}$ and $D_{\text{Cl}^-}^{\text{bulk}} = 2.06 \times 10^{-5} \text{cm}^2/\text{s}$.

Additionally, the diffusion coefficient for the pore region is $D_{\alpha}^{\text{pore}} = D_{\alpha}^{\text{bulk}}/21$ for each species α [220].

3.3 MET channel prototype simulations

In the present simulation work, we mainly study the electrostatic distribution and transport features of potassium (K^+) chloride (Cl^-) in our channel prototype. In order to verify our prototype, the computational results are compared with the experimental findings from the reference [123].

3.3.1 Experimental data

Experiments were conducted on outer hair cells of Sprague-Dawley rats. At first, the apical and middle turns of the organ of Corti were excised from rats between 6 and 14 days postnatal and then chemically treated as previously reported in the literature [17, 18, 123, 124]. The separated turns were fixed in the experimental chamber and the axial motion of a glass pipette deflects hair bundles, which activates the MET channels. Currents and bundle motions were recorded mostly at the beginning of the apical turn and averages of 10 stimuli were calculated to obtain a standard error of ± 1 [123].

We mainly focus on the MET channel current which reveals the state of the channel. The time course of the MET channel current can be divided into three steps [123]. The first step represents that the channels respond to the bundle motions within microseconds, which proves the direct relationship between bundle motion and channel activation. Then the second part describes fast adaptation, which indicates the process of the channel closure. The third part refers to slow adaptation of the MET channel mechanism, which is related to the restoration of the sensitivity of the hair bundle.

The next significant feature of the MET channel is the normalized current (I/I_{Max}), which can be regarded as the channel open probability. It is also presented in the literature [123]. The relation between the normalized current and the displacement of the bundle shows a nonlinear sigmoidal behavior, which demonstrates the following. The positive deflection (toward the longest stereocilium) increases the open probability; on the contrary, the negative deflection (away from the longest stereocilium) decreases the open probability.

3.3.2 Computational results

We explore the behavior of our MET prototype under various conditions including the applied voltage, bulk ion concentration, and the charge and position of the blocker. One of the fundamental issues is the electrostatic potential profile projected to the channel direction (z -direction) at the middle of the channel pore. Except specified, we set the charge of the blocker as $Q = 2e_c$ with an elementary charge e_c , the bulk concentrations of both ion species as $C^0 = C_{\text{K}^+}^0 = C_{\text{Cl}^-}^0 = 0.1\text{M}$ (molar) and the applied external voltage at the electrode near the channel gate as $\Phi^0 = 0.1\text{V}$. Note that the concentration for both ion species are always identical at the bulk regions.

We first examine the impact of moving the charged blocker along the x -direction. The

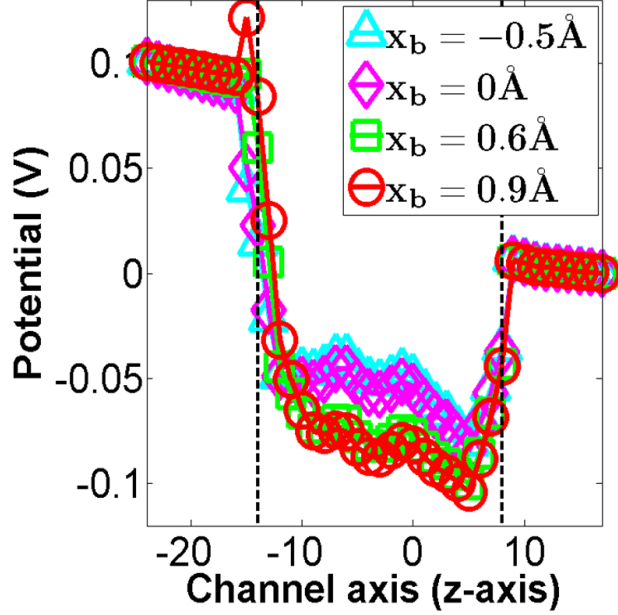


Figure 3.2: Electrostatic potential profiles at different locations x_b of the blocker with charge $Q = 2e_c$ when $C^0 = 0.1\text{M}$ and $\Phi^0 = 0.1\text{V}$. The region between two dashed lines indicates the channel pore region. As the blocker position gets closer to 0.9\AA along the x -direction, the blocker produces a stronger barrier near the channel mouth as shown in the electrostatic potential profile.

goal of this study is to verify whether the proposed MET prototype suitably represents the MET channel in terms of its mechanically sensitive behavior. We transfer the charged blocker from $x_b = -0.5\text{\AA}$ to 0.9\AA with fixing its y - and z -coordinates. As illustrated in Fig. 3.2, at locations $x_b = 0.6\text{\AA}$ and $x_b = 0.9\text{\AA}$, the charged blocker creates a large electrostatic barrier at the channel mouth region, which hinders the inward flow of the cation K^+ . Consequently, the electrostatic potential level inside the channel becomes very lower due to the fact that the positive ions cannot effectively enter through the channel. Therefore, the proposed MET prototype shows a desirable gating effect.

Next, we examine the behavior of our channel model in response to the change in bulk ion concentration C^0 . We place the blocker with the charge of $Q = 2e_c$ at $x_b = 0.9\text{\AA}$. We set $\Phi^0 = 0.1\text{V}$ for the applied voltage. Two different bulk ion concentrations $C^0 = 0.1\text{M}$ and $C^0 = 0.2\text{M}$ are tested in our numerical experiments. Fig. 3.3(a) illustrates the response

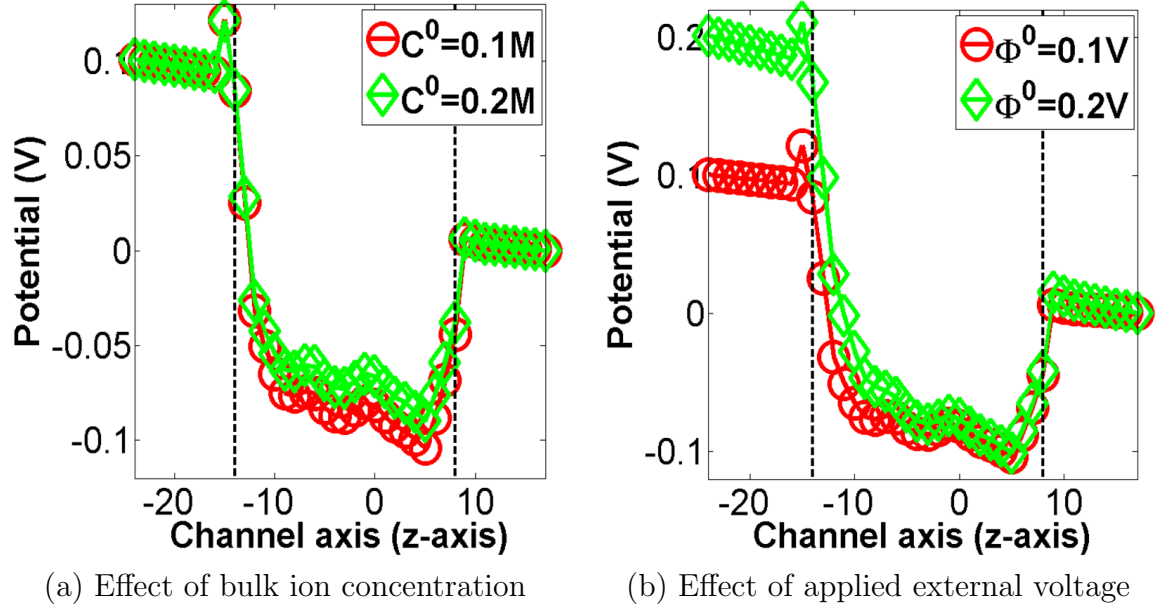


Figure 3.3: Electrostatic potential profiles along the channel direction for the MET prototype (a) at different bulk ion concentrations $C^0 = 0.1\text{M}$ (circles) and $C^0 = 0.2\text{M}$ (diamonds) under the fixed applied voltage $\Phi^0 = 0.1\text{V}$ and (b) at different applied external voltages $\Phi^0 = 0.1\text{V}$ (circles) and $\Phi^0 = 0.2\text{V}$ (diamonds) under the fixed bulk concentration $C^0 = 0.1\text{M}$. In both investigations, we locate the blocker at $x_b = 0.9\text{\AA}$ and set the blocker charge as $Q = 2e_c$. Increase either in the bulk concentration or in the external voltage creates higher potential within the channel.

of the present model at these two bulk ion concentrations by comparing the electrostatic potential curve along the channel pore direction. The variance in the bulk ion concentration has little influence on the electrostatic profile outside of the channel pore region. Especially, the electrostatic property of the outside part is dominated by the applied voltage and also reflects the electrical neutralization of cations and anions. However, the increase in the bulk ion concentration leads a higher concentration of the positive ion to pass through the channel pore region, which enhances the electrostatic potential within the channel as well.

We further investigate the behavior of our model under two different applied voltages. To this end, we set $x_b = 0.9\text{\AA}$, $Q = 2e_c$ and $C^0 = 0.1\text{M}$. The external voltage applied at the electrode near the channel mouth is doubled from $\Phi^0 = 0.1\text{V}$ to $\Phi^0 = 0.2\text{V}$. The electrostatic potential profiles in response to this change are depicted at Fig. 3.3(b). We see an obvious

change in the electrostatic potential in the left bulk region near the channel mouth and in the left part of the channel pore region.

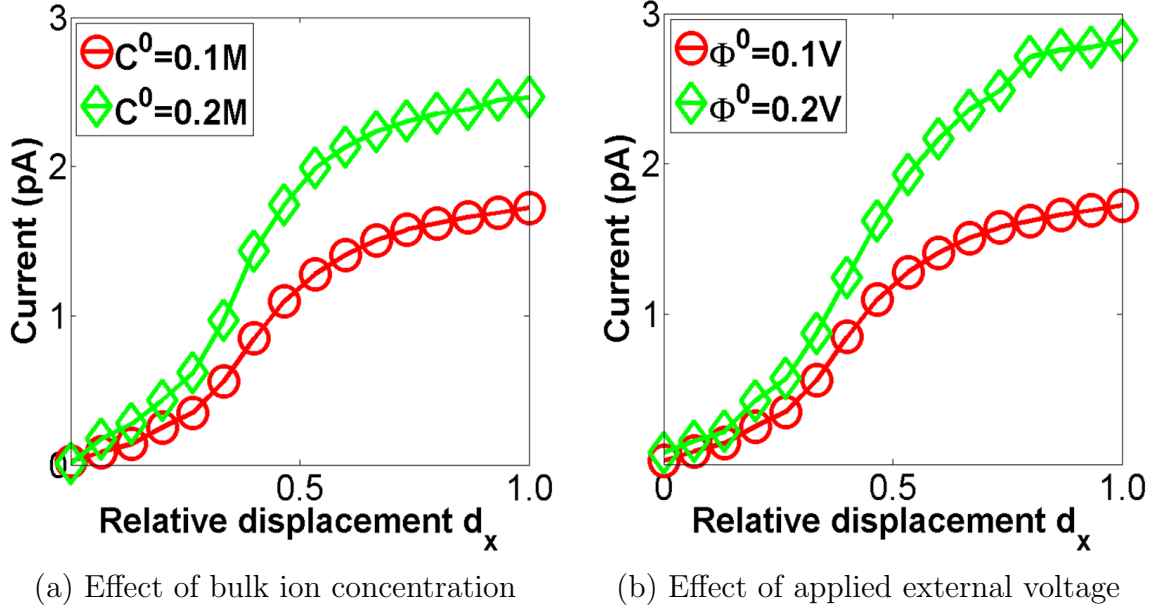


Figure 3.4: The total current versus the relative displacement d_x of the charged blocker. (a) Total current behavior under two bulk ion concentrations $C^0 = 0.1\text{M}$ (circles) and $C^0 = 0.2\text{M}$ (diamonds) when $Q = 2e_c$ and $\Phi^0 = 0.1\text{V}$ are fixed. (b) Total current behavior under two external voltages $\Phi^0 = 0.1\text{V}$ (circles) and $\Phi^0 = 0.2\text{V}$ (diamonds) when $Q = 2e_c$ and $C^0 = 0.1\text{M}$ are fixed. Consequently, increase either in bulk ion concentration or in external voltage induces increase in channel current.

To show the effectiveness of the blocker, we study the impact of the displacement of the blocker along the x -direction under the fixed blocker charge $Q = 2e_c$ as shown in Figure 3.4. We analyze the channel current pattern under two bulk ion concentrations $C^0 = 0.1\text{M}$ and $C^0 = 0.2\text{M}$ as shown in Fig. 3.4(a) and under two applied voltages $\Phi^0 = 0.1\text{V}$ and $\Phi^0 = 0.2\text{V}$ as shown in Fig. 3.4(b). In this numerical experiment, we define a relative displacement d_x as the scaled distance of the blocker from its optimal position. When the relative displacement is zero, i.e., $d_x = 0$, the blocker locates right on top of the channel mouth, which essentially blocks the channel and creates the closed state. When $d_x = 1$, there is no blocking effect and hence the system reaches its normal open state. Clearly, the current across the channel

gets higher as the relative displacement increases. Meanwhile, the channel current increases as the bulk ion concentration increases because of permeating more cations through the channel, which is consistent with the increase in the electrostatic potential within the channel pore region shown in Fig. 3.3(a). Similarly, the channel current increases as the applied external voltage increases due to the increase in the electrostatic potential as shown in Fig. 3.3(b). Moreover, these results agree qualitatively with those of hair bundle deflections in the literature [123, 124].

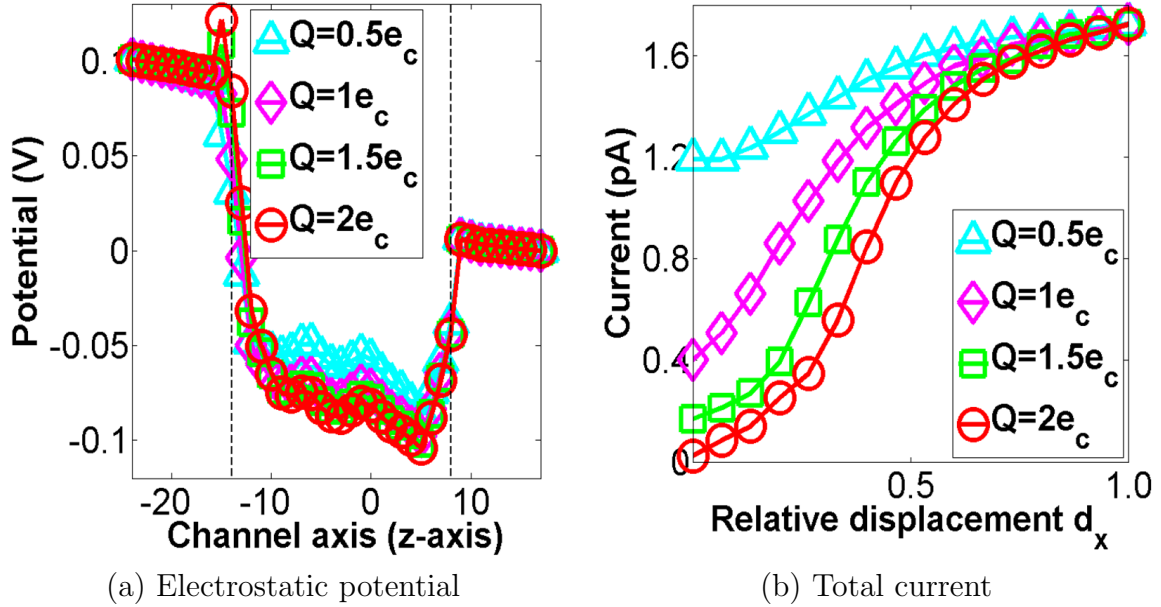


Figure 3.5: (a) Electrostatic potential profiles and (b) total current profiles for four different charges $Q = 0.5e_c$ (triangles), $Q = 1e_c$ (diamonds), $Q = 1.5e_c$ (squares) and $Q = 2e_c$ (circles) when $C^0 = 0.1M$ and $\Phi^0 = 0.1V$ are fixed. The region between two dashed lines indicates the channel pore region in (a). As the blocker charge gets increased, the barrier at the gate of the channel gets higher. In conclusion, the amplitude of the current curve also gets enlarged.

Having established the importance of the blocker position to the channel open-closed transition, we are interested in other properties of the blocker that may contribute to its gating mechanism. Two most relevant properties are the blocker size and charge. In the present system, the change of the molecular size of the blocker is ineffective in the channel behavior because the standard PNP model does not consider the finite volume effect [114, 138].

However, it can be studied how the blocker charge affects the ion conductance through the MET prototype. To this end, we test our model with a number of different atomic charges, namely, $Q = 0.5e_c$, $Q = 1e_c$, $Q = 1.5e_c$ and $Q = 2e_c$, while set $C^0 = 0.1\text{M}$ and $\Phi^0 = 0.1\text{V}$. Our calculation results are presented in Fig. 3.5. In Fig. 3.5(a), the electrostatic potential at the entrance of the channel is dramatically influenced by the magnitude of the blocker charge. A larger charge generates a higher potential barrier, which results in less density of the cation and a lower electrostatic potential within the channel pore region. In Fig. 3.5(b), we illustrate the impact of the blocker charge on the relation between the channel current and the relative blocker displacements d_x . It is interesting to notice that only when the atomic charge reaches an appropriate threshold, the blocker can effectively close the channel gate. Therefore, an ionic current leakage exists when the blocker does not carry sufficient charge or is not located at its optimized position.

It is attractive to compare our model prediction with the experimental finding of the relation between the open probability and the rat hair bundle displacement given in the literature [123]. To this end, we compute the channel open probability P_O at a number of relative displacement d_x with four different atomic charges when we set $C^0 = 0.1\text{M}$ and $\Phi^0 = 0.1\text{V}$. For an explicit comparison, our calculation data are presented in Fig. 3.6 together with experimental data [123]. Amazingly, there is an excellent agreement between our theoretical prediction and experimental measurement when the blocker charge is $Q = 2e_c$. Thus we can conclude that $Q = 2e_c$ is the optimal charge in our molecular level prototype of the MET channel. Our simulation result implies that our molecular level prototype is able to reveal the mechanoelectrical gating mechanism of the MET channel in hair cells.

Finally, our optimal model predictions are obtained with fixed applied voltage and bulk ion concentration. Obviously, it remains to investigate whether our model prediction is

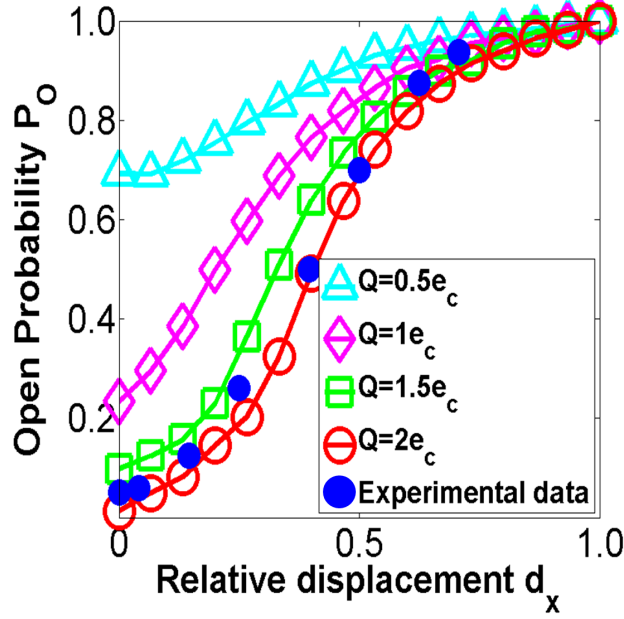


Figure 3.6: Open probability P_O is plotted against the relative displacement d_x under four different atomic charges $Q = 0.5e_c$ (triangles), $Q = 1e_c$ (diamonds), $Q = 1.5e_c$ (squares) and $Q = 2e_c$ (circles) where $C^0 = 0.1M$ and $\Phi^0 = 0.1V$ are set. The solid dots are experimental data of the normalized MET current versus normalized rat hair bundle displacement obtained from the literature [123]. At each blocker charge, the open probability in response to the relative displacement forms a sigmoidal shape and, especially, the charge $Q = 2e_c$ gives a remarkable agreement with the experimental result.

sensitive to the variance of these two experimental conditions. As shown in Fig. 3.7, although bulk ion concentration and applied external voltage are doubled in our numerical simulations, the computational data does not change very much in terms of the open probability. There is still an outstanding consistency between our MET model prediction and experimental measurement [123]. This result further validates the robustness of our molecular level prototype for the rat MET channel.

3.4 Concluding remarks

The auditory system is one of the most significant sensory systems for mammals. Mechano-electrical transducer (MET) is a principal device in mammalian auditory system for the brain

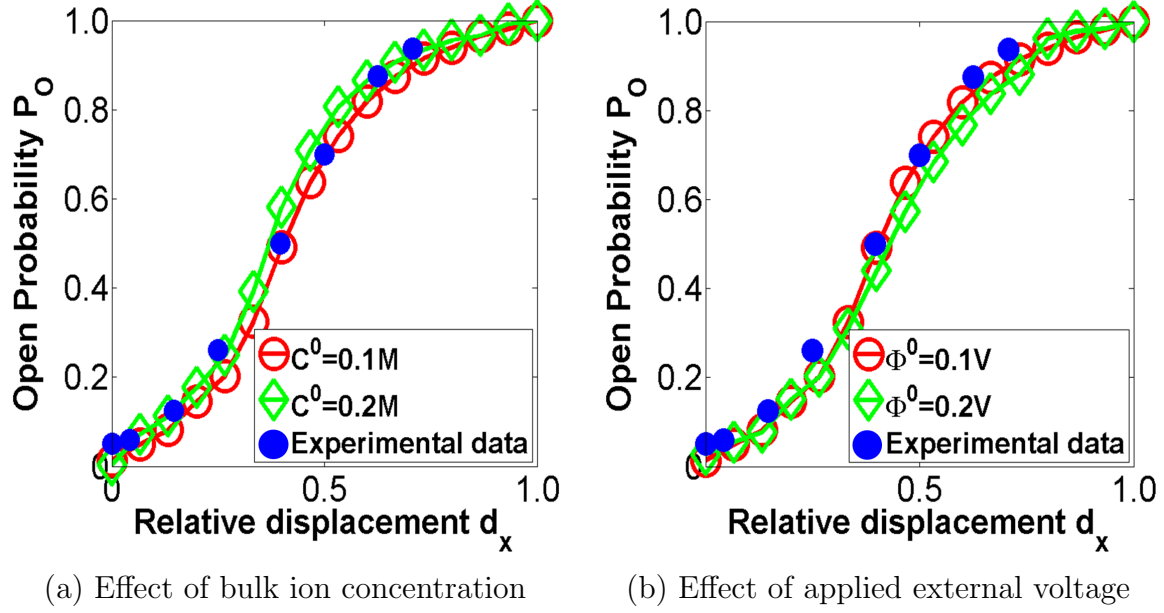


Figure 3.7: Sensitivity test of the molecular level MET model for the prediction of open-closed probability according to the relative blocker displacement when (a) the bulk ion concentration is doubled; (b) the applied external voltage is doubled. Both cases are fairly consistent with the experimental finding [123].

to perceive sounds. It is generally speculated that hair cell deflections regulate the MET channels located at the stereocilia on each hair cell top. However, the molecular building blocks of the MET channel are not yet available to date and hence its gating mechanism is still evasive. In this work, we construct a molecular level prototype for the mammalian MET channel in order to elucidate the mechanoelectrical gating mechanism of mechanotransduction in mammals. Our MET prototype consists of a realistic ion channel, namely, the Gramicidin A (GA) channel, an additional charged lip, called a blocker, which is positioned at the GA channel mouth, and membrane layers.

To explore the physical properties of the proposed MET prototype, we employ a well-tested theoretical model, the Poisson-Nernst-Planck (PNP) model, for three dimensional (3D) numerical simulations of the MET channel transport. Advanced computational techniques which have been well-established in our earlier work, such as Dirichlet-to-Neumann mapping

(DNM) and matched interface and boundary (MIB) method, are utilized for the present numerical simulations. We design extensive numerical experiments to analyze in detail the electrostatic potential and channel current in response to variations of blocker charge, blocker relative displacement, bulk ion concentration and external voltage applied at the electrode in the channel entrance region. Finally, we compare our prototype prediction with experimental measurement from rat outer hair cells [123] in regard to the relation between channel open probability and relative displacement. Remarkable consistency between two data is observed under pertinent physical conditions. We further demonstrate that our molecular based model is insensitive to the change of both ion concentration in bulk region and applied external voltage. Our numerical findings indicate that hair-cell tip links, which connect hair bundles, efficiently convey mechanical force to mechanosensitive transduction channels and manage their opening and closing.

Chapter 4

Modeling and simulating three types of ionic diffusive nanofluidic channels

In this chapter, we introduce a nanofluidic system model to analyze a realistic ionic diffusive nanofluidic channel with atomic charge details and propose a second-order convergent numerical method for nanofluidic problems. First of all, we validate the second-order accuracy of our proposed numerical solver for Poisson-Nernst-Planck (PNP) equations with ionic diffusive nanochannels in three dimensional (3D) realistic settings. Next, we investigate the impact of atomic charge distribution on the fluidic behavior of a few 3D nanoscale channels. We demonstrate that atomic charges give rise to specific and efficient control of nanochannel flows. Furthermore, the change of the distribution in atomic surface charges is orchestrated with the variation of applied external voltage and bulk ion concentration in order to understand nanofluidic currents. Therefore, we are able to elucidate quantitatively the transport phenomena of three types of ionic diffusive nano-scaled channels, including a negatively charged channel, a bipolar channel and a double-well channel. These flow patterns are examined in terms of electrostatic potential profiles, ion concentration distributions and current-voltage characteristics.

The rest of this chapter is organized as follows. In Section 4.1, we introduce an atomic scale nanofluidic structure including a cylindrical channel with atomic charges and two bulk

reservoirs. Section 4.2 is devoted to validate the present PNP calculation with synthetic nanoscale channels. We first test a cylindrical nanochannel with one charged atom at the middle of the channel length and then examine the channel with eight atomic charges that are equally placed around the channel. Since PNP equations admit no analytical solution in general, we design analytical solutions for a modified PNP system, which has the same mathematical characteristics as the standard PNP system. In Section 4.3, we investigate the atomic scale control and regulation of cylindrical nanofluidic systems. Three ionic diffusive nanofluidic channels, such as a negatively charged channel, a bipolar channel and a double-well channel, are inspected in terms of electrostatic potential, ion concentration and current. Finally, this paper ends with concluding remarks in Section 4.4.

4.1 Atomic scale design of an ionic diffusive nanofluidic channel

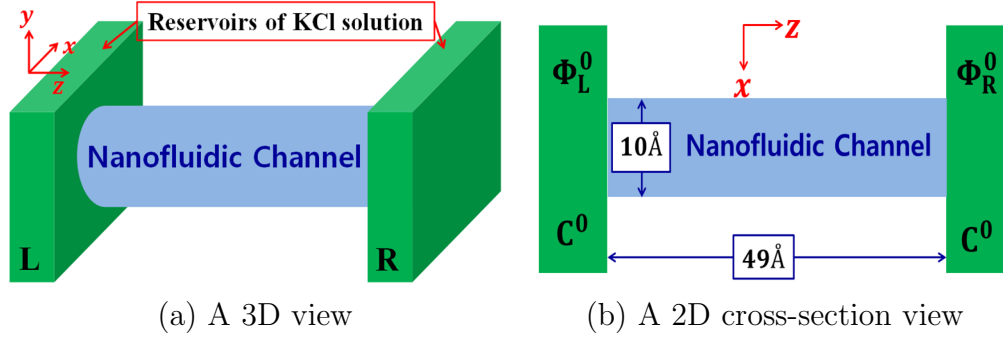


Figure 4.1: Illustration of a nanofluidic system geometry. (a) A 3D view of a schematic cylindrical nanochannel whose ends are connected to two reservoirs of KCl solution. (b) A 2D cross-section view of the cylindrical channel whose diameter is 10\AA and length is 49\AA in the xz -plane. Here, Φ_L^0 and Φ_R^0 , respectively, represent the external voltage applied at the left and right electrodes, and C^0 represents the bulk ion concentration of both K^+ and Cl^- in two reservoirs.

In the present work, we construct a $16 \times 16 \times 56$ cuboid nanofluidic system. It contains an

ionic diffusive cylindrical nanochannel which is placed at the center of the system and whose both ends are connected to reservoirs of potassium chloride (KCl) solution as illustrated in Fig. 4.1(a). The radius of the channel pore is 5\AA and the length of the channel is 49\AA as depicted in Fig. 4.1(b). In our simulation study, the computational domain Ω is the nanofluidic system which is mainly divided into ion inclusion region Ω_s and ion exclusion region Ω_m as in Fig. 2.1(b). The ion inclusion region contains the region inside the channel and two reservoirs where ions may penetrate and travel through, while the ion exclusion region is the rest where there is no mobile ion, but there are fixed charged particles. In contrast to our differential geometry based multiscale models [207, 208, 206], the interface Γ between two regions Ω_s and Ω_m is predetermined by the channel structure and does not change during our simulation.

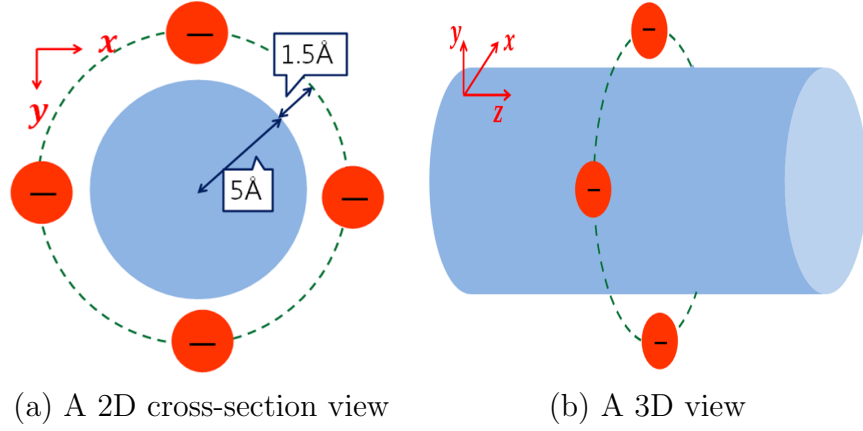


Figure 4.2: Illustration of atomic charge distribution. (a) A 2D cross-section view and (b) a 3D view of schematic diagram consisting of the cylindrical channel and four atomic charges which are equally placed around the nanochannel at $z = 0\text{\AA}$.

A number of properly charged atoms are positioned around the channel at an interval of about 1.8\AA so that the channel flow can be regulated by electrical charges. In reality, these charged atoms can be realized by appropriate dopants. The z -coordinates of the atoms along the channel length are determined first. Then at each cross section perpendicular

to the channel axis, the atomic charges are aligned along a concentric circle whose size is sufficiently bigger than that of the channel pore. The locations of the atoms are equally spaced according to the circumference of the circle. Fig. 4.2 shows an example of placing four negative atomic charges around the cylindrical channel at $z = 0\text{\AA}$. In the cross section on the xy -plane, we divide a concentric circle with radius 6.5\AA into four parts and then locate each anion as described in Fig. 4.2(a). Managing the number, magnitudes and signs of atomic charges enables generating various types of surface charge distribution on the ionic diffusive nanofluidic channel.

4.2 Numerical validation

In our earlier work [220], we develop and verify a second order of PNP solver for proteins and biological ion channels. In this work, we construct analytically solvable solid-state nanofluidic systems to validate the proposed numerical methods. The analytic solution of the PNP equations is unknown for realistic geometries. However, it is a standard procedure to design an analytical solution for slightly modified PNP equations, which share the same mathematical features with the original PNP equations [220]. Consequently, the numerical convergence of the designed solution algorithms can be validated.

First, we consider two simple nanochannel examples, one with a single atomic charge, and the other with eight atomic charges, in order to verify the second order convergence of our numerical methods. Next, both a negatively charged nanofluidic channel and a bipolar nanofluidic channel are utilized to further validate the proposed numerical schemes.

In our computation, we match the nanofluidic system with a cuboid which has the size of $[-8, 8] \times [-8, 8] \times [-28, 28]$. We set $\epsilon_m = 1$ and $\epsilon_s = 80$ in all the numerical tests in

this section. Therefore, there is a sharp discontinuity in the dielectric coefficient across the channel-solvent interface.

4.2.1 Analytical solution system

We consider a set of N_m charged atoms, each of which is placed at $\mathbf{r}_k = (x_k, y_k, z_k)$ in the microscopic channel region Ω_m and possesses a fixed charge Q_k , where $k = 1, 2, \dots, N_m$. The geometry of the analytically solvable system can be arbitrary in principle. However, one can refer to the cylindrical geometry described in Fig. 4.1 and the computational domain illustrated in Fig. 2.1(b). We define the electrostatic potential as follows:

$$\Phi(\mathbf{r}) = \begin{cases} \cos x \cos y \cos z + \sum_{k=1}^{N_m} \frac{Q_k}{\epsilon_m \sqrt{(x-x_k)^2 + (y-y_k)^2 + (z-z_k)^2}}, & \mathbf{r} \in \Omega_m \\ \frac{0.4\pi}{3\epsilon_s} \cos x \cos y \cos z, & \mathbf{r} \in \Omega_s. \end{cases} \quad (4.1)$$

For two mobile ion species, the concentrations are given by

$$C_1(\mathbf{r}) = 0.2 \cos x \cos y \cos z + 0.1 \quad \text{and} \quad C_2(\mathbf{r}) = 0.1 \cos x \cos y \cos z + 0.1 \quad (4.2)$$

for $\mathbf{r} \in \Omega_s$, but $C_1(\mathbf{r}) = C_2(\mathbf{r}) = 0$ for $\mathbf{r} \in \Omega_m$ because ions are able to move only in the solution region Ω_s .

This set of solutions (4.1) and (4.2) satisfies the following PNP-like equations

$$\begin{cases} -\nabla \cdot (\epsilon(\mathbf{r}) \nabla \Phi(\mathbf{r})) = 4\pi \sum_{k=1}^{N_m} Q_k \delta(\mathbf{r} - \mathbf{r}_k) + 4\pi [C_1(\mathbf{r}) - C_2(\mathbf{r})] + R(\mathbf{r}), & \mathbf{r} \in \Omega \\ \nabla \cdot [\nabla C_1(\mathbf{r}) + C_1(\mathbf{r}) \nabla \Phi(\mathbf{r})] = R_1(\mathbf{r}), & \mathbf{r} \in \Omega_s \\ \nabla \cdot [\nabla C_2(\mathbf{r}) - C_2(\mathbf{r}) \nabla \Phi(\mathbf{r})] = R_2(\mathbf{r}), & \mathbf{r} \in \Omega_s. \end{cases} \quad (4.3)$$

Herein, we set, respectively, the charge of two mobile ion species as $q_1 = 1$ and $q_2 = -1$, and their diffusion coefficients as $D_1(\mathbf{r}) = D_2(\mathbf{r}) = 1$ for all $\mathbf{r} \in \Omega_s$. Moreover, for every $\mathbf{r} \in \Omega_s$,

$$\begin{cases} R(\mathbf{r}) = -3 \cos x \cos y \cos z \\ R_1(\mathbf{r}) = -0.6 \cos x \cos y \cos z + \frac{0.4\pi}{3\epsilon_s} \nabla \cdot [(0.2 \cos x \cos y \cos z + 0.1) \nabla (\cos x \cos y \cos z)] \\ R_2(\mathbf{r}) = -0.3 \cos x \cos y \cos z - \frac{0.4\pi}{3\epsilon_s} \nabla \cdot [(0.1 \cos x \cos y \cos z + 0.1) \nabla (\cos x \cos y \cos z)] \end{cases}$$

However, $R(\mathbf{r}) = R_1(\mathbf{r}) = R_2(\mathbf{r}) = 0$ for all $\mathbf{r} \in \Omega_m$. The jump conditions at the interface Γ can be specifically given in the following:

$$\begin{cases} [\Phi(\mathbf{r})] = \Phi^*(\mathbf{r}) + \left(1 - \frac{0.4\pi}{3\epsilon_s}\right) \cos x \cos y \cos z \\ [\epsilon(\mathbf{r}) \nabla \Phi(\mathbf{r})] \cdot \mathbf{n} = \epsilon_m \nabla [\cos x \cos y \cos z + \Phi^*(\mathbf{r})] \cdot \mathbf{n} - \epsilon_s \nabla \left(\frac{0.4\pi}{3\epsilon_s} \cos x \cos y \cos z\right) \cdot \mathbf{n}, \end{cases}$$

where \mathbf{n} is the outward unit normal vector and $\Phi^*(\mathbf{r}) = \sum_{k=1}^{N_m} \frac{Q_k}{\epsilon_m \sqrt{(x - x_k)^2 + (y - y_k)^2 + (z - z_k)^2}}$.

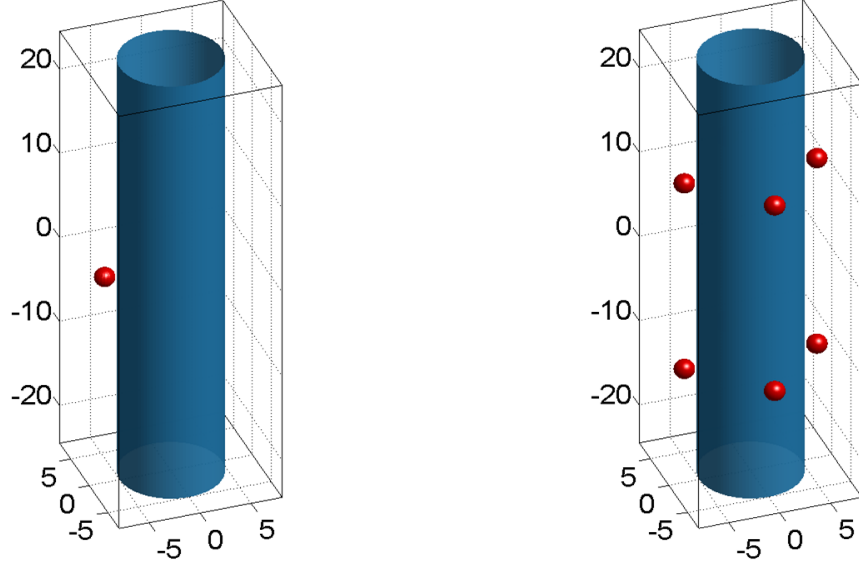
In order to investigate the convergence order, we apply two error measurements

$$L_\infty = \max_{i,j,k} |F_{i,j,k}^{\text{num}} - F_{i,j,k}^{\text{exact}}| \text{ and } L_2 = \sqrt{\frac{1}{N} \sum_{i,j,k} (F_{i,j,k}^{\text{num}} - F_{i,j,k}^{\text{exact}})^2},$$

where $F_{i,j,k}^{\text{num}}$ and $F_{i,j,k}^{\text{exact}}$, respectively, represent the numerical and exact values of a function F at (x_i, y_j, z_k) , and N is the total number of computational nodes.

4.2.2 A cylindrical nanochannel with a single atomic charge

We first test the cylindrical channel with a single atomic charge. The atomic charge is placed at $(6.5, 0, 0)$ and its charge is -0.08 as shown in Fig. 4.3(a). The set of analytical solutions (4.1) and (4.2) of the PNP equations introduced in Subsection 4.2.1 is used to compare with



(a) With a single negative atomic charge (b) With eight negative atomic charges

Figure 4.3: Illustration of the geometries of two simple numerical test cases.

numerical results by solving Eq. (4.3). We calculate the electrostatic potential $\Phi(\mathbf{r})$, the positive ion concentration $C_1(\mathbf{r})$ and the negative ion concentration $C_2(\mathbf{r})$ at four different mesh sizes: $h = 0.4$, $h = 0.32$, $h = 0.2$, and $h = 0.16$. Table 4.1 demonstrates numerical errors and convergence orders for different number of computational nodes. The computational result attains a good second order convergence. Moreover, the errors and orders for both concentrations show little difference.

4.2.3 A cylindrical nanochannel with eight atomic charges

Next, we explore the same dimensional cylindrical nanochannel with eight fixed atoms with a charge of -0.08 over the channel surface as illustrated in Fig. 4.3(b). Consider two cross-sections perpendicular to the channel length at $z = -11$, and $z = 11$. In order to maintain the same distance of each atom from the channel surface and the same angle difference between two adjacent atoms, we employ the polar coordinate system. For each

Table 4.1: Numerical errors and orders for the cylindrical channel with a single atomic charge.

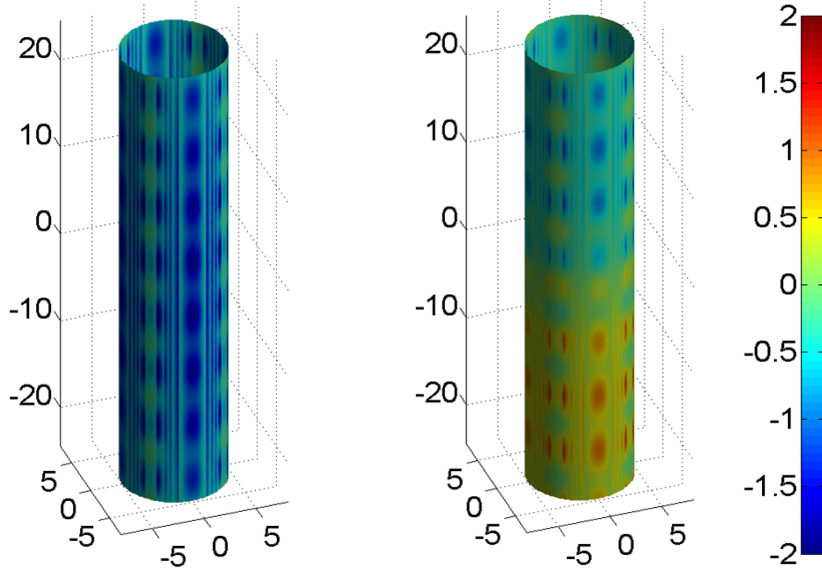
	Mesh size	L_∞		L_2	
		Error	Order	Error	Order
Φ	$h = 0.4$	1.3742E-2	—	3.1647E-3	—
	$h = 0.32$	8.7238E-3	2.0362	2.0215E-3	2.0088
	$h = 0.2$	3.5614E-3	1.9062	8.7926E-4	1.7712
	$h = 0.16$	2.2282E-3	2.1016	5.3548E-4	2.2224
C_1	$h = 0.4$	3.8661E-3	—	1.0406E-3	—
	$h = 0.32$	2.5648E-3	1.8390	6.4972E-4	2.1106
	$h = 0.2$	8.4896E-4	2.3524	2.5014E-4	2.0309
	$h = 0.16$	5.4286E-4	2.0039	1.5920E-4	2.0250
C_2	$h = 0.4$	2.0352E-3	—	5.3493E-4	—
	$h = 0.32$	1.3130E-3	1.9642	3.2772E-4	2.1958
	$h = 0.2$	4.7824E-4	2.1488	1.3661E-4	1.8617
	$h = 0.16$	2.7990E-4	2.4327	8.0089E-5	2.3930

Table 4.2: Numerical errors and orders for the cylindrical channel with eight atomic charges.

	Mesh size	L_∞		L_2	
		Error	Order	Error	Order
Φ	$h = 0.4$	1.3745E-2	—	3.1649E-3	—
	$h = 0.32$	8.7249E-3	2.0369	2.0214E-3	2.0092
	$h = 0.2$	3.5571E-3	1.9090	8.7894E-4	1.7720
	$h = 0.16$	2.2300E-3	2.0925	5.3564E-4	2.2194
C_1	$h = 0.4$	3.8661E-3	—	1.0406E-3	—
	$h = 0.32$	2.5648E-3	1.8390	6.4972E-4	2.1106
	$h = 0.2$	8.4892E-4	2.3525	2.5015E-4	2.0308
	$h = 0.16$	5.4286E-4	2.0037	1.5920E-4	2.0252
C_2	$h = 0.4$	2.0353E-3	—	5.3493E-4	—
	$h = 0.32$	1.3130E-3	1.9643	3.2772E-4	2.1958
	$h = 0.2$	4.7824E-4	2.1488	1.3659E-4	1.8620
	$h = 0.16$	2.7790E-4	2.4326	8.0091E-5	2.3923

atomic charge, the distance from the center of the channel pore is always 6.5\AA and the inter-atomic angle is a right angle. Therefore, the central coordinates of these atoms are $\left(6.5 \cos\left(\frac{\pi}{2}i\right), 6.5 \sin\left(\frac{\pi}{2}i\right), -11\right)$ and $\left(6.5 \cos\left(\frac{\pi}{2}i\right), 6.5 \sin\left(\frac{\pi}{2}i\right), 11\right)$ for $i = 0, 1, 2,$ and 3 . As a result, we obtain four equally spaced atomic charges at each cross section. We test this nanofluidic channel system at four different mesh sizes: $h = 0.4$, $h = 0.32$, $h = 0.2$, and $h = 0.16$. As shown in Table 4.2, the errors and orders in solving the PNP equations with this atomic charge setting generate little difference from those with a single atomic charge. This validation experiment also indicates the second order convergence of our proposed algorithms.

4.2.4 A negatively charged ionic diffusive nanofluidic channel



(a) A negatively charged channel (b) A bipolar channel

Figure 4.4: Surface plot of electrostatic potential profiles on (a) a negatively charged channel and (b) a bipolar channel. As represented in the color bar, blue colors represent negative values, while red colors represent positive values. The negatively charged channel surface is mostly blue, but the color of the bipolar channel surface is changed from red to blue.

Now, we perform another numerical test to verify the convergence and accuracy of the proposed PNP calculation on a more realistic nanofluidic channel. At first, we design a

negatively charged nanochannel, or called a unipolar nanochannel. The channel length on the z -axis is divided into 27 subdivisions and then there are 28 nodes between $z = -23$, and $z = 23$. Thus the distance between two adjacent atoms along the z -direction is about 1.8. On a circular cross section at each node along the z -axis, eight atoms with a charge of -0.08 , all of which are 1.5 apart from the cylinder surface. They are equally spaced in a circular pattern and so the interatomic angular difference is half a right angle. The x - and y -coordinates of each atomic charge are calculated by using the polar coordinate system; consequently, The detailed coordinates of the atomic charge distribution are given in Table 3.

In order to ensure that the channel surface is negatively charged, we first examine colored surface plot and contour plots of the electrostatic potential $\Phi(\mathbf{r})$ by numerically solving Eq. (4.3). The computational results are demonstrated in Fig. 4.4(a) and Fig. 4.5. The colored surface plot is useful to understand the effect of the atomic charge on the nano-scaled channel. Fig. 4.4(a) shows the electrostatic potential profile over the surface of this nanochannel. The greater part of the channel surface has blue colors with a little different darkness. Since the blue colors indicate the negative electrostatic potential values, it is obvious that the channel surface possesses negative charge.

From the boundary line of the channel clearly shown in contour plots in Fig. 4.5, it is interesting to discern that our proposed PNP solver works very well with ion diffusive nanofluidic channels. Three contour plots of the electrostatic potential $\Phi(\mathbf{r})$ at $z = -10$, $z = 0$ and $z = 10$ are described in Fig. 4.5. In every picture, we can notice that the right outside of the channel is dark blue, which implies that the channel surface is negatively charged.

Then we use the same analytical solutions (4.1) and (4.2) to calculate the numerical errors and orders at four different mesh sizes: $h = 0.4$, $h = 0.32$, $h = 0.2$ and $h = 0.16$. The

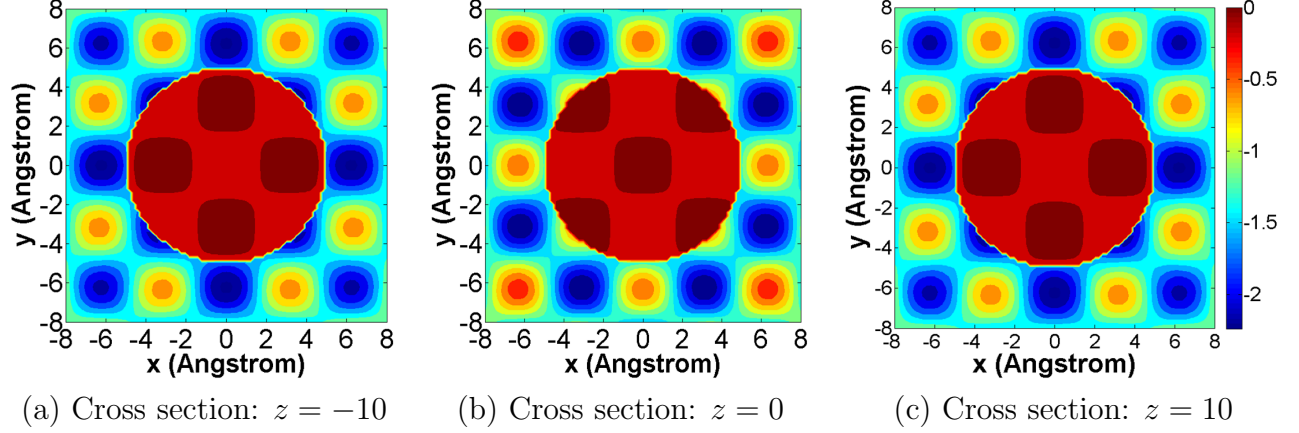


Figure 4.5: Three contour plots of electrostatic potential through the negatively charged channel at $z = -10$, $z = 0$ and $z = 10$ on the xy -plane when the mesh size is $h = 0.2$. The blue colors just outside the channel imply the negative surface charge.

calculation results are given in Table 4.3. Through this numerical observation, we confirm that our proposed PNP numerical schemes achieve the second order accuracy in computing the potential and ion concentrations for the nano-sized channel with negative atomic charges on its surface.

4.2.5 A bipolar ionic diffusive nanofluidic channel

We also consider a bipolar nanofluidic channel which functions as a nanofluidic diode. It is a nano-sized channel whose atomic coordinates are the same as those of the aforementioned negatively charged nanochannel. However, their charges are altered from positive to negative or vice versa at the middle of the channel axis [41, 56]. In our ionic diffusive bipolar channel, the first half cylinder (from $z = -23$ to $z = -0.8519$) is affected by atoms with charge of 0.08 and the atomic charges on the other half (from $z = 0.8519$ to $z = 23$) are -0.08 . Table 4 presents all of the detailed central positions and charges of the atomic charge distribution of this bipolar nanofluidic channel.

The computational results of the electrostatic potential through the bipolar channel are

Table 4.3: Numerical errors and orders for the negatively charged channel.

	Mesh size	L_∞		L_2	
		Error	Order	Error	Order
Φ	$h = 0.4$	1.3803E-2	—	3.1672E-3	—
	$h = 0.32$	8.7573E-3	2.0389	2.0218E-3	2.0116
	$h = 0.2$	3.5184E-3	1.9401	8.7433E-4	1.7836
	$h = 0.16$	2.3190E-3	1.8682	5.3538E-4	2.1980
C_1	$h = 0.4$	3.8725E-3	—	1.0406E-3	—
	$h = 0.32$	2.5664E-3	1.8437	6.4976E-4	2.1103
	$h = 0.2$	8.6571E-4	2.3121	2.5037E-4	2.0291
	$h = 0.16$	5.4302E-4	2.0902	1.5936E-4	2.0244
C_2	$h = 0.4$	2.0402E-3	—	5.3508E-4	—
	$h = 0.32$	1.3126E-3	1.9765	3.2767E-4	2.1978
	$h = 0.2$	4.8312E-4	2.1265	1.3660E-4	1.8615
	$h = 0.16$	2.7784E-4	2.4793	8.0291E-5	2.3816

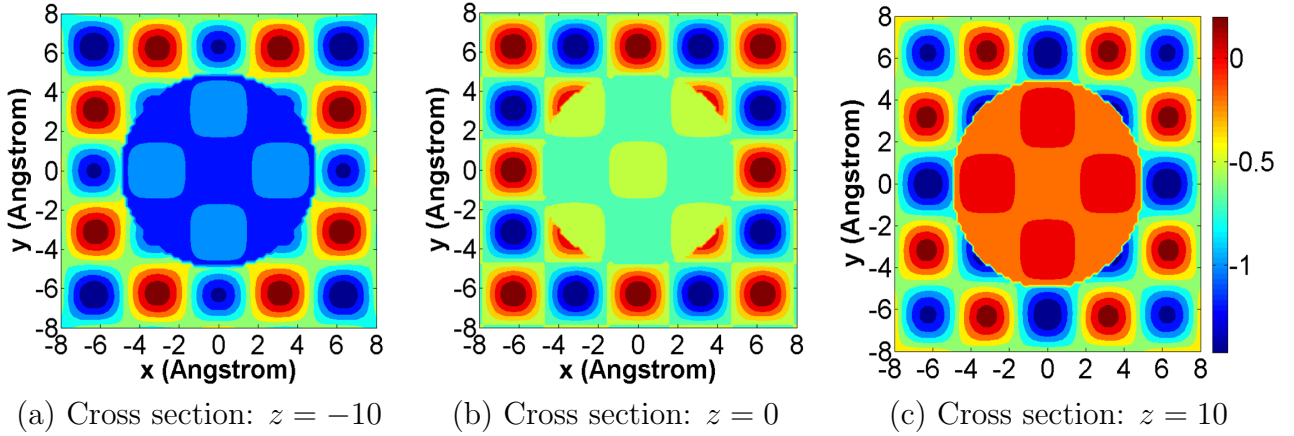


Figure 4.6: Three contour plots of electrostatic potential through the bipolar channel at $z = -10$, $z = 0$ and $z = 10$ on the xy -plane when the mesh size is $h = 0.2$. As indicated in the color bar, blue colors represent negative values, while red colors represent some small positive values. At the cross section of $z = -10$ the inside of the channel is blue (i.e., negatively charged solution), whereas at the cross section of $z = 10$ the inside of the channel is red (i.e., slightly positively charged solution).

shown in Fig. 4.4(b) and Fig. 4.6 by solving the system of equations (4.3). From Fig. 4.4(b), we are able to see that the atomic surface charges are changed from positive to negative along the z -direction. Such properties of the bipolar channel are also clearly manifested in the cross-sectional results in Fig. 4.6. When we compare the contour plots in Fig. 4.6(a) and Fig. 4.6(c), it is a little bit difficult to distinguish the colors of the outside of the

Table 4.4: Numerical errors and orders for the bipolar channel.

	Mesh size	L_∞		L_2	
		Error	Order	Error	Order
Φ	$h = 0.4$	1.3752E-2	—	3.1649E-3	—
	$h = 0.32$	8.7568E-3	2.0227	2.0217E-3	2.0086
	$h = 0.2$	3.5649E-3	1.9121	8.7942E-4	1.7711
	$h = 0.16$	2.2421E-3	2.0782	5.3585E-4	2.2201
C_1	$h = 0.4$	3.8743E-3	—	1.0406E-3	—
	$h = 0.32$	2.5663E-3	1.8458	6.4975E-4	2.1105
	$h = 0.2$	8.5125E-4	2.3479	2.5016E-4	2.0308
	$h = 0.16$	5.4306E-4	2.0143	2.5016E-4	2.0191
C_2	$h = 0.4$	2.0384E-3	—	5.3493E-4	—
	$h = 0.32$	1.3132E-3	1.9706	3.2773E-4	2.1967
	$h = 0.2$	4.8477E-4	2.1203	1.3665E-4	1.8611
	$h = 0.16$	2.7790E-4	2.4935	8.0280E-5	2.3837

bipolar channel. However, the channel inside obviously shows different colors, which indicates that the variation of atomic charges influences the ion transport through the ionic diffusive nanochannel.

The validation of our numerical schemes for the bipolar nanofluidic channel is given in Table 4.4. Again, we compare numerical solutions of Eq. (4.3) and exact solutions (4.1) and (4.2) in this bipolar channel at four different mesh sizes: $h = 0.4$, $h = 0.32$, $h = 0.2$ and $h = 0.16$. As we can see in Table 4.4, the computational result apparently demonstrates a good second-order convergence for this test problem.

4.3 Nanofluidic simulations

Having validated the numerical convergence of our proposed PNP algorithm, we explore the nature of charged ionic diffusive nanofluidic channels under various physical conditions including applied voltage, atomic charge distribution and bulk ion concentration. Specifically, we investigate the electrostatic distribution and transport features of potassium chloride

through the nanochannels. Our advanced numerical solver of the standard PNP theory provides concentration for two ion species K^+ and Cl^- and electrostatic potential at each node in the computational domain. Then the obtained values are averaged over the xy -cross section at each z . Using such calculation process, we investigate ion concentration distributions and electrostatic potential profile along the channel direction (z -direction). We also illustrate current-voltage (I-V) curve in which the current at the center of the channel length is given by Eq. (12). Particularly, ion concentration distribution describes the movements of two different ion species through a channel in detail and current-voltage characteristic clearly shows electrical features of a nanochannel. We examine three kinds of nano-scaled channels, namely a negatively charged channel, a bipolar channel and a double-well channel. We have used the dielectric constants $\epsilon_m = 2$ and $\epsilon_s = 80$ for all simulations in this section. For real physical simulations of biological ion channels and synthetic nanofluidic channels with atomic detail, it is also important to make use of one unit system [220]. Pertinent units that are consistent with fundamental physical laws and central physical constants should be employed so that the computational results can be directly compared with experimental measurements. Thus, we discuss the units of the PNP model in this simulation work in Chapter B.

4.3.1 A negatively charged ionic diffusive nanofluidic channel

In order to clarify the role of atomic charge in ionic diffusive nanofluidic systems, we first consider a negatively charged channel described in Subsection 4.2.4 and the atomic charges of the channel are specified in Table 3. Here, all of the ions placed to generate the atomic surface charge are anions with the same magnitude of charge. We vary the external voltage only at the electrode of the right reservoir and keep bulk ion concentrations of both reservoirs same. Therefore, the applied voltage is a driving force to relocate potassium ions and chloride

ions via the ionic diffusive nanochannel. The atomic charges determine the ion selectivity of the nanochannel and the bulk ion concentration affects the current migrated through the channel.

Effect of applied voltage

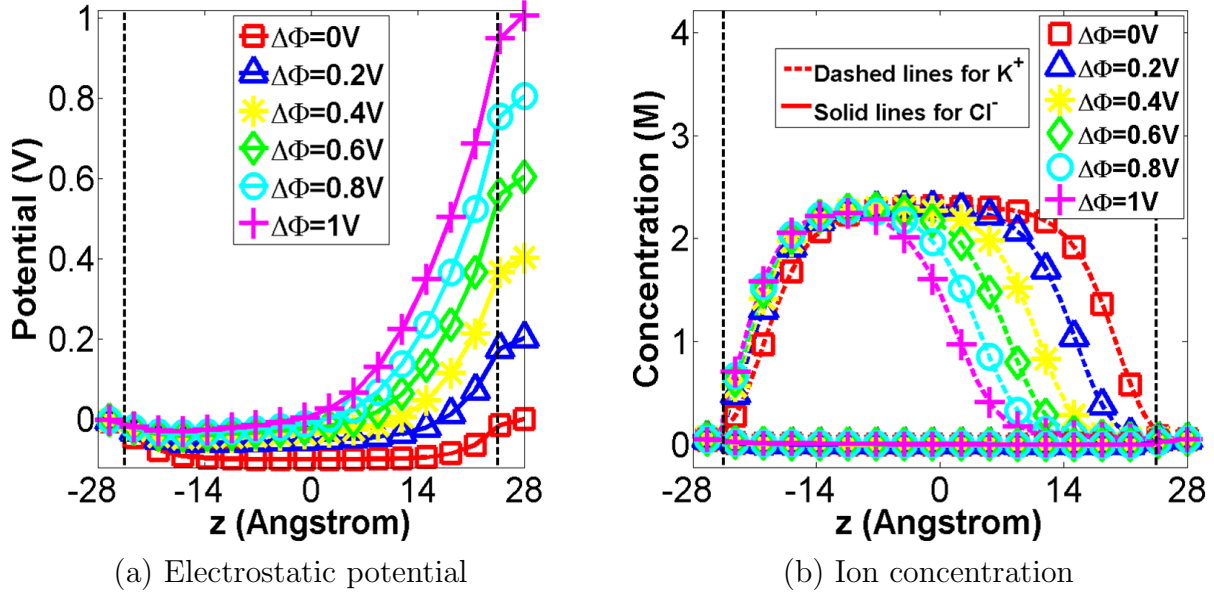


Figure 4.7: Effect of applied voltage on electrostatics and dynamics through the negatively charged nanofluidic channel. (a) Electrostatic potential profiles and (b) ion concentration distributions along the channel length (z -axis). Here $\Delta\Phi$ is varied from 0V (squares), 0.2V (triangles), 0.4V (asterisks), 0.6V (diamonds), 0.8V (circles) to 1V (plus signs), where $\Delta\Phi$ is the difference of the applied voltage between two electrodes. Each surface atomic charge is $Q_k = -0.08e_c$ and bulk concentration is $C^0 = 0.05M$. Two dashed vertical lines indicate the ends of the nanochannel. As the applied voltage difference gets larger, the potential at the right part of the inner channel is increased. Consequently, more K^+ ions (dashed line) are accumulated at the left part of the inner channel. However, there is little change in the concentration of Cl^- ion (solid line).

First, we study the impact of applied external voltage on behavior of ions traveling within a negatively charged nanochannel. We set the ion concentrations of K^+ and Cl^- in both bulk regions as $C^0 = 0.05M$ and each atomic surface charge as $Q_k = -0.08e_c$. The voltage applied at left electrode of the system, Φ_L^0 , is fixed at 0V and the voltage applied at right electrode of the system, Φ_R^0 , is increased gradually from 0V to 1V. The $\Delta\Phi$ represents the difference

between Φ_R^0 and Φ_L^0 , where $\Delta\Phi = \Phi_R^0 - \Phi_L^0$. Figure 4.7 illustrates the electrostatic potential and ion concentrations along the z -axis in response to the external voltage difference. In Fig. 4.7(a), as Φ_R^0 gets increased, the electrostatic potential at the right part of the inner channel becomes dramatically higher. As a result, more cations are accumulated at the left part of the inner channel as shown in Fig. 4.7(b). In contrast, the concentration of Cl^- shows little difference from the bulk concentration. This transport phenomenon is originated from the fact that the negative atomic charges of the channel electrostatically repel anions and attract cations. This electrostatic effect also makes the solution within the channel almost unipolar, which can be more obviously observed with current-voltage characteristic.

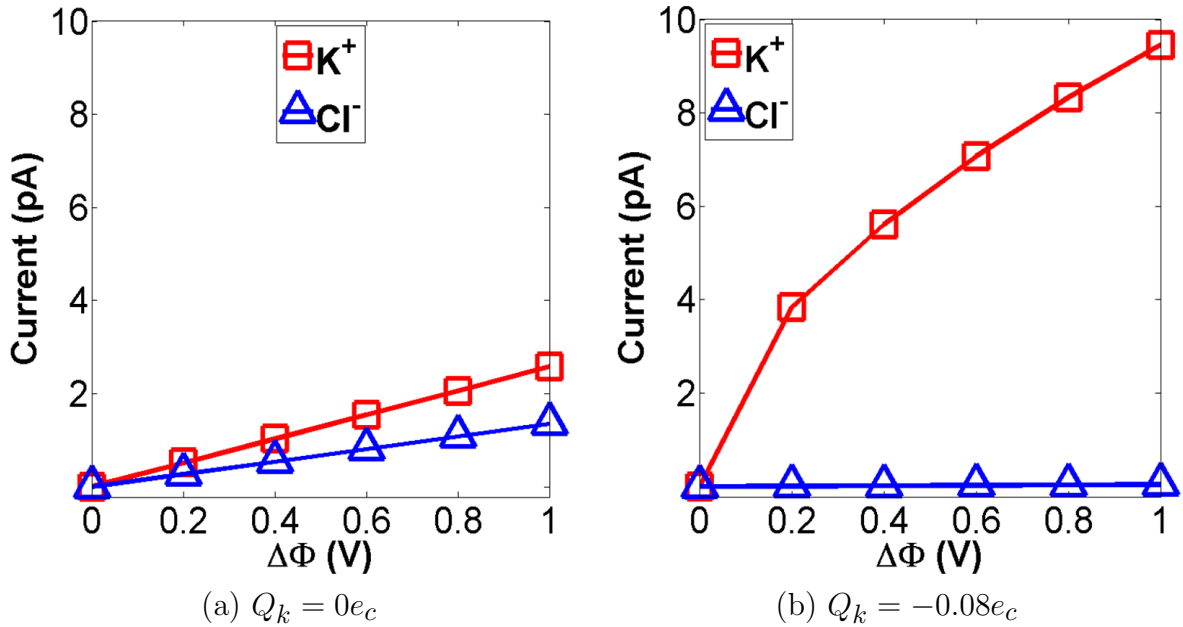


Figure 4.8: Ionic current for each ion species versus the applied potential difference $\Delta\Phi$ through (a) the uncharged nanochannel ($Q_k = 0e_c$) and (b) the negatively charged nanochannel ($Q_k = -0.08e_c$). Here, the bulk ion concentrations at both reservoirs are fixed at $C^0 = 0.05\text{M}$. When $Q_k = 0e_c$, both current-voltage graphs are linear and the positive current (squares) is roughly double of the negative current (triangles). When $Q_k = -0.08e_c$, the positive current-voltage graph (squares) is nonlinear and the negative current-voltage graph (triangles) is almost always zero.

By comparing the current-voltage (I-V) curve of the negatively charged channel with that of an uncharged channel, we are able to clarify the effect of atomic surface charge

on a nanometer channel. In these two graphs, the current values are obtained using Eq. (12) at the circular xy -cross section inside the channel when $z = 0\text{\AA}$. The current at every z -location through the channel is almost constant at steady state and hence the current at the center of the channel axis is usually chosen to elucidate the current-voltage relation. Fig. 4.8(a) gives the relation between current of each ion species and external voltage within the same dimensional nanofluidic channel without atomic charges ($Q_k = 0e_c$). Both of the ionic currents are proportional to the applied voltage and, especially, the K^+ current is roughly double of the Cl^- current. In this case, the nanochannel obeys the Ohm's law and is non-selective. In contrast, the set of negative atomic charges on the channel surface destroys the linearity of the positive current-voltage characteristic, and also generates a large difference between two ionic currents as shown in Fig. 4.8(b). This nonlinearity or deviation from the Ohm's law is closely related to the non-proportionality between the potential change within the channel and the applied voltage [57]. Since the negatively charged channel wall hinders the access of Cl^- ions at the channel gate, the negative current is almost zero for every applied voltage. However, since the negative surface charge strongly attracts K^+ ions and the external potential difference encourages more ions to pass through the channel, the cation current gets increased. From this numerical observation, we can conclude that an ionic diffusive nanochannel with unipolar atomic charge distribution generates a charged current mostly composing of counterions and the current through this channel can be increased by providing more external voltage.

Effect of atomic charge

Next, we examine the effect of atomic surface charge on ionic flow through the negatively charged channel. Except for the magnitude of Q_k , we fix the bulk ion concentrations for

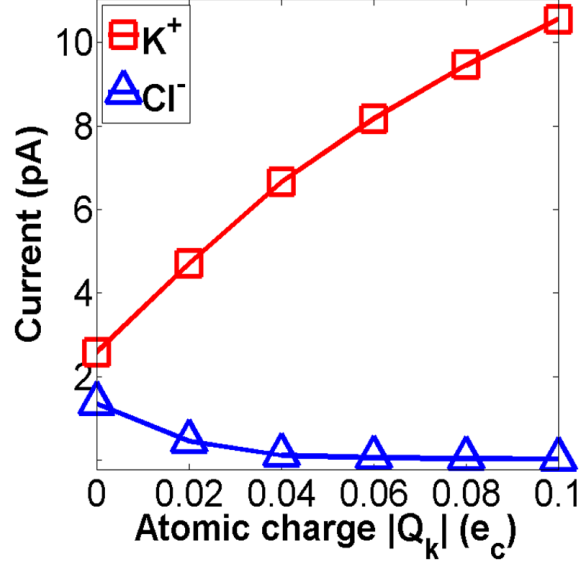


Figure 4.9: Effect of atomic surface charge on ionic current through the negatively charged nanochannel. The ionic currents in response to the change of the atomic charge Q_k are depicted. Six different charges $Q_k = 0e_c$, $Q_k = -0.02e_c$, $Q_k = -0.04e_c$, $Q_k = -0.06e_c$, $Q_k = -0.08e_c$ and $Q_k = -0.1e_c$ are simulated under the fixed bulk concentration $C^0 = 0.05M$ and applied voltage difference $\Delta\Phi = 1V$. Herein, $|Q_k|$ is the magnitude of the charge of the each atom. Stronger atomic charges amplify the K^+ current (squares) sharply, but reduce the Cl^- current (triangles) to near zero.

both ion species at $C^0 = 0.05M$ and the applied voltage difference at $\Delta\Phi = 1V$. A stronger negative atomic charge, i.e., a larger value of $|Q_k|$, promotes the accumulation of the cations inside the channel and prevents the anions from entering the channel gate. As a result, the K^+ current is dramatically increased; however, the Cl^- current is decreased to almost zero. The positive current is not directly proportional to the atomic charge magnitude because of a stronger ionic diffusion induced by the larger concentration gradient [57]. From this study, it is interesting to note that the channel current can be controlled by the atomic charge amplitude. When the amplitude (ΔI) of the current reaches a suitable threshold, almost all ions, which have the same sign of charge with the channel atomic charge, cannot penetrate through the inlet of the nanochannel. Therefore, our proposed nanofluidic channel possesses a near perfect ion selectivity.

Effect of bulk ion concentration

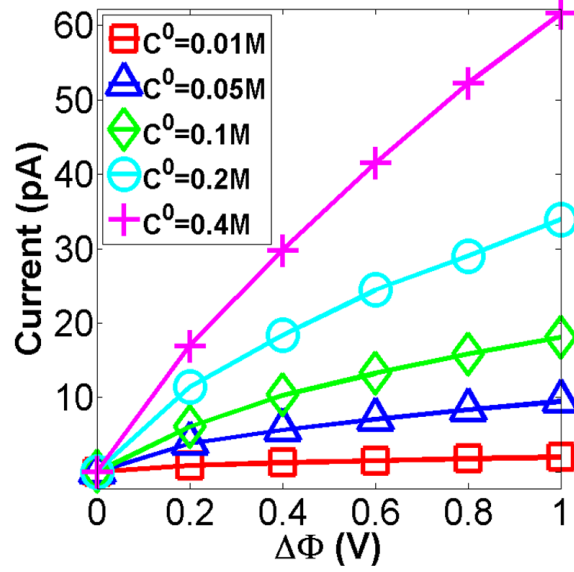


Figure 4.10: Effect of bulk ion concentration on total current through the negatively charged nanochannel. The graphs of total channel current against the external voltage difference (I-V) are shown at five different bulk concentrations $C^0 = 0.01M$ (squares), $C^0 = 0.05M$ (triangles), $C^0 = 0.1M$ (diamonds), $C^0 = 0.2M$ (circles) and $C^0 = 0.4M$ (plus signs) when $Q_k = -0.08e_c$. As the bulk ion concentration is increased, the total current gets higher and, moreover, the I-V characteristic becomes near linear.

Another important aspect, which is also necessary to understand the transport within an ionic diffusive nanofluidic channel, is the bulk ion concentration. The electrical double layer produces a unique difference between a nanofluidic channel and a microfluidic channel. The bulk ion concentration is a crucial factor to determine the thickness of the double layer. When the double layers overlap inside a nanochannel, the aqueous solution confined in the channel expresses charge opposite to the surface charge of the nanochannel [55]. Fig. 4.10 shows the total current as a function of the applied voltage difference for five different bulk ion concentrations $C^0 = 0.01M$, $C^0 = 0.05M$, $C^0 = 0.1M$, $C^0 = 0.2M$ and $C^0 = 0.4M$. Here, the atomic charge Q_k is assumed to be $-0.08e_c$. The increased bulk ion concentration induces more cations to penetrate through the channel, which results in the dramatic increase of the

total channel current. However, a higher bulk ion concentration reduces the double layer and, additionally, the channel surface becomes neutralized by the pulled counterions within the layer [57]. Consequently, the I-V curve is almost linear, in other words, obeys Ohm's law. It is pretty evident that a charged channel with high bulk ion concentration behaves like an uncharged channel due to the decrease in the Debye length.

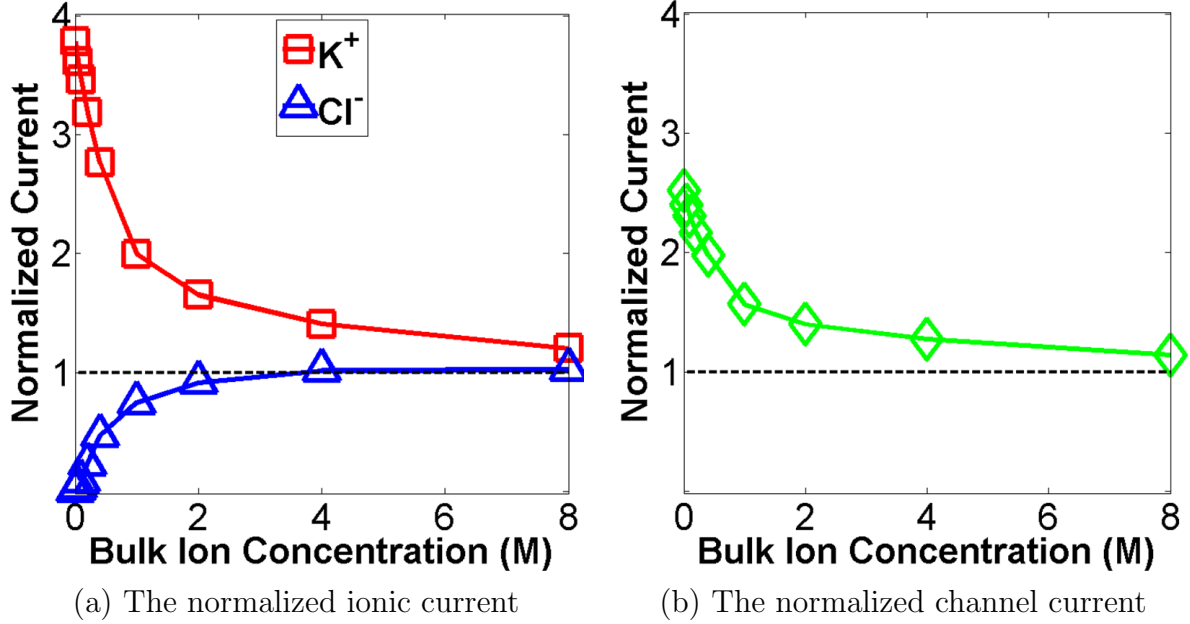


Figure 4.11: The effect of bulk ion concentration on the normalized current through the negatively charged nanochannel. (a) The normalized ionic current and (b) the normalized channel current with respect to the increase in bulk ion concentration when the atomic charge $Q_k = -0.08e_c$ and the applied voltage difference $\Delta\Phi = 1V$ are fixed. The negatively charged channel with a sufficiently larger bulk ion concentration behaves like a uncharged channel because the normalized values becomes one.

The normalized current is considered to assure that a higher bulk ion concentration weakens the role of atomic surface charge. The normalized current is computed by dividing the current through the negatively charged channel by that through the uncharged channel so that we can observe the difference between two channels. Excluding the atomic charges, both channels have the same voltage difference and the bulk ion concentration gets gradually increased at the same time. We calculate the normalized value of each ion species current and

then add them together to obtain the total current. Fig. 4.11(a) represents the normalized ionic current for each ion species and Fig. 4.11(b) shows the normalized total channel current. In both figures, the normalized values get close to one as the bulk ion concentration is increased. This feature implies that the charged channel under a high bulk ion concentration does not demonstrate much atomic charge effect on the nanofluidic transport phenomena.

4.3.2 A bipolar ionic diffusive nanofluidic channel

As the second subject of the nanofluidic simulations, we examine a bipolar ionic diffusive channel whose dimensions and atomic charge constitution are described in Subsection 4.2.5. In this channel, the first half of the channel is positively charged and the second half is negatively charged. Therefore, it is interesting to explore the transport properties of the bipolar nanochannel because a bipolar channel can behave like a p-n junction.

Effect of applied voltage

We first consider three types of voltage bias across the channel length. One case is called no bias ($\Delta\Phi = 0V$) when both electrodes of the system have zero voltage. Another case is named as a forward bias ($\Delta\Phi > 0$) when the voltage applied at the right electrode of the system is greater. The other case, on the contrary, is referred to as a reverse bias ($\Delta\Phi < 0$) when the voltage at the left electrode of the system is greater. To see the impact of external voltage, we fix the bulk ion concentration of KCl at 0.1M, and the atomic charges on left and right halves, respectively, at $0.08e_c$ and $-0.08e_c$. Fig. 4.12 compares the electrostatic potential profiles and ion concentration distributions along the z -direction at three applied voltage differences, including $\Delta\Phi = 0V$, $\Delta\Phi = 1V$ and $\Delta\Phi = -1V$.

As shown in Fig. 4.12(i-a), when $\Delta\Phi = 0V$, the electrostatic potential is high under the

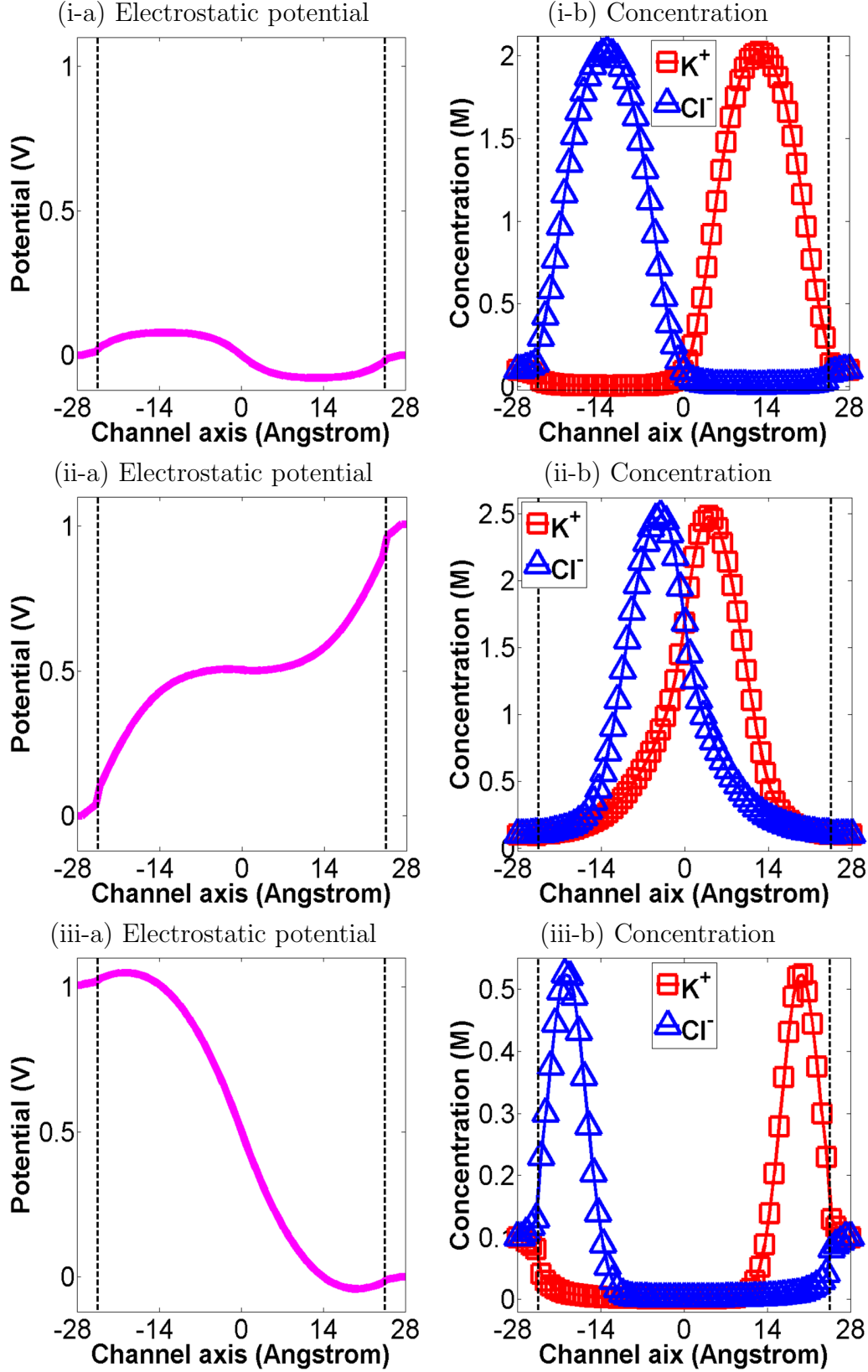


Figure 4.12: (a) Electrostatic and (b) ion concentration profiles of the bipolar nanofluidic channel along the channel axis at (i) no bias $\Delta\Phi = 0\text{V}$, (ii) forward bias $\Delta\Phi = 1\text{V}$ and (iii) reverse bias $\Delta\Phi = -1\text{V}$. Fix the bulk ion concentration $C^0 = 0.1\text{M}$ and the atomic surface charges $|Q_k| = 0.08e_c$.

positive atomic charges, but it is low under the negative atomic charges. Subsequently, the ion concentration is plotted in the opposite way as illustrated in Fig. 4.12(i-b). Generating the potential gap $\Delta\Phi$ between two ends of the system brings about two peculiar phenomena within the bipolar ionic diffusive nanochannel. At the forward bias with $\Delta\Phi = 1\text{V}$, the electrostatic potential is gradually increased as in Fig. 4.12(ii-a), but at the reverse bias with $\Delta\Phi = -1\text{V}$, it is sharply decreased as in Fig. 4.12(iii-a). These two results demonstrate excellent consistency with the ion concentration curves in the way that the flux is invariable along the channel axis at steady state and thus the main factor altering the potential is the ion distribution [56]. As plotted in Fig. 4.12(ii-b), under the forward bias, both ion species are attracted to the junction, so the peak value of the ion concentration is greater than that under no bias. However, under the reverse bias, both ion species are moved away from the junction and each one produces a small pile at the atomic surface charge with opposite sign as presented in Fig. 4.12(iii-b). Accordingly, the forward bias brings about an ion accumulation zone at the channel junction, whereas the reverse bias creates an ion depletion zone there. These concentration patterns influence on current-voltage relation of the bipolar nanofluidic channel.

Figure 4.13 shows the current-voltage relation of each ion species through the bipolar channel. While both ionic current graphs are almost zero at every reverse bias ($\Delta\Phi < 0$), they are monotonically increased under forward bias as the potential difference becomes bigger. This simulation phenomenon is closely related to the two novel transport phenomena within a bipolar nanochannel: the ion-depletion zone under reverse bias and the ion-accumulation zone under forward bias. We already manifest these features in Fig. 4.12(ii-b) and (iii-b), respectively. The ion-depletion zone terminates the flow inside the bipolar nanochannel, but the ion-accumulation zone encourages more ions to penetrate through the nanochannel.

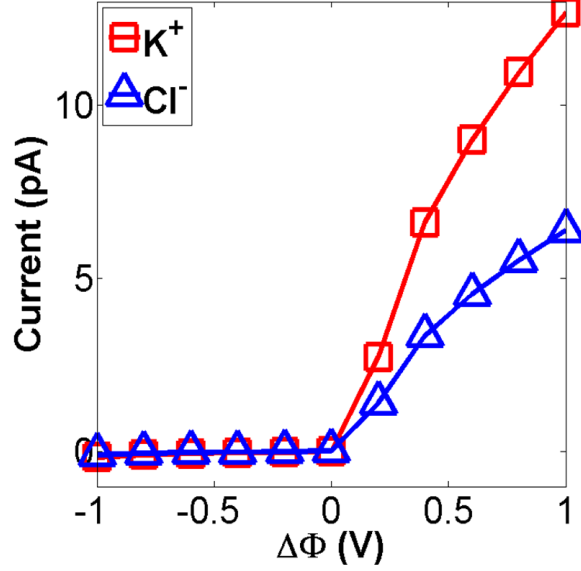


Figure 4.13: Ionic current versus applied voltage difference in the bipolar nanofluidic channel. The atomic charge $|Q_k| = 0.08e_c$ and the bulk ion concentration $C^0 = 0.1M$ are assumed. Under reverse bias, both ion species cannot pass through the channel. However, under forward bias, the currents of both ion species get enlarged. Especially, the cation current (squares) increases faster.

In particular, the positive ionic current enhances more abruptly as in Fig. 4.13. Another remarkable discovery from the current-voltage characteristic is that a higher applied voltage reduces the gradient of the curve $\left(\frac{dI}{d(\Delta\Phi)}\right)$. This feature is relevant to the polarization caused by the concentration gradient, which is analytically discussed in the literature [56]. To sum up, managing the external voltage facilitates turning on and off the current through the bipolar nanochannel.

Effect of atomic charge

Next, we consider how atomic surface charge affects the dynamics inside the nano-scaled channel. Fig. 4.14 depicts the channel currents in response to the applied voltage difference at three different surface charges $|Q_k| = 0.04e_c$, $|Q_k| = 0.08e_c$ and $|Q_k| = 0.12e_c$. In this numerical experiment, we set the bulk ion concentration at two reservoirs to be 0.1M. In every case of atomic charge, the total current gets enlarged as $\Delta\Phi$ gets larger under forward bias,

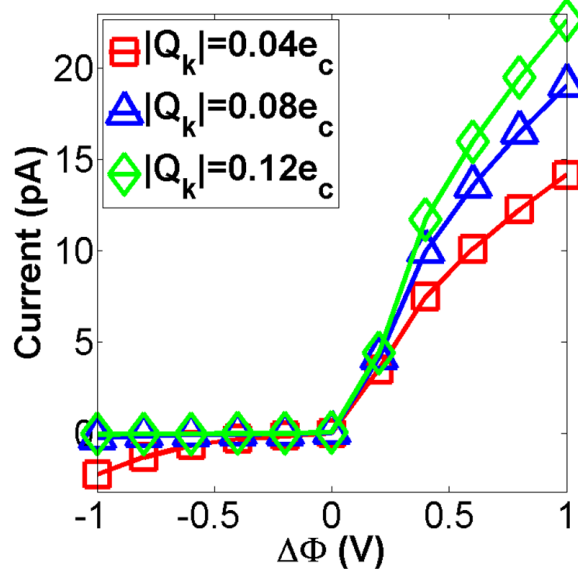


Figure 4.14: Effect of atomic surface charge on the current through the bipolar nanofluidic channel. Three sets of atomic charges, that is, $|Q_k| = 0.04e_c$ (squares), $|Q_k| = 0.08e_c$ (triangles) and $|Q_k| = 0.12e_c$ (diamonds), are studied. Here, the bulk ion concentration C^0 is fixed at 0.1M. All I-V curves increase when $\Delta\Phi$ varies from -1V to 1V . Greater magnitude of the atomic charge results in a higher channel current with forward bias, but insufficient atomic charge may generate a current leakage because it weakens the depletion zone with reverse bias.

but the rate of change of the current with respect to the voltage difference gets moderated.

The highest atomic charge, that is, $|Q_k| = 0.12e_c$, generates the greatest amplitude of the current curve. In contrast, the lowest atomic charge amplitude, that is, $|Q_k| = 0.04e_c$ does not fully draw both ion species to either sides under reverse bias, and subsequently diminishes the ion-depletion zone at the middle of the channel. Thus, the channel current becomes nonzero at some negative voltage differences. From this numerical experiment, it is beneficial to discover that the channel current within a bipolar ionic diffusive nanofluidic channel can be perfectly regulated if the atomic charges on the channel surface satisfy an appropriate threshold.

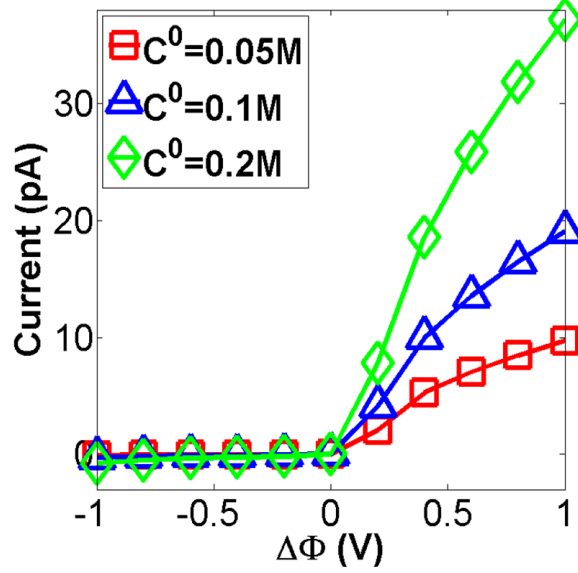


Figure 4.15: Effect of bulk ion concentration on the channel current through the bipolar nanofluidic channel. Three sets of bulk ion concentrations, such as $C^0 = 0.05M$ (squares), $C^0 = 0.1M$ (triangles) and $C^0 = 0.2M$ (diamonds), are explored in terms of the current-voltage relation. The atomic charges are given by $|Q_k| = 0.08e_c$. As the bulk ion concentration gets higher, the amplitude and gradient of the current-voltage relationship gets maximized.

Effect of bulk ion concentration

We also test our bipolar ionic diffusive channel at two more different bulk ion concentrations, namely, $C^0 = 0.05M$ and $C^0 = 0.2M$, in order to observe the impact of bulk ion concentration on the transport feature. Then we compare the total current-voltage graphs with that at $C^0 = 0.1M$ as described in Fig. 4.15. Every current-voltage curve nearly vanishes when $\Delta\Phi$ is negative, but significantly increases when $\Delta\Phi$ is positive. As the bulk ion concentration is doubled, more ions are accumulated at the junction of the bipolar nanofluidic channel under forward bias, so the total current gets almost doubled. Moreover, the amplitude (ΔI) and gradient of the current alteration with respect to the external voltage difference $\left(\frac{dI}{d(\Delta\Phi)}\right)$ are increased as well. To this end, it is expected to surmise that bulk ion concentration promotes the quantity of the total current through the bipolar nanochannel. Amazingly, our computational outcomes are in a good agreement with other numerical studies in the

literature [56].

4.3.3 A double-well ionic diffusive nanofluidic channel

Finally, we investigate the transport phenomena within a double-well nanofluidic channel, which is named after the shape of the electrostatic potential curve across the channel length. The electrostatic potential within a cylindrical nanofluidic channel may have several potential wells by modifying atomic charge distribution on the channel surface. Actually, the irregular partial charges of biological ion channel proteins induce electrostatic potential wells. For instance, Gramicidin A channel, one of the most well-known biological channels, is a double-well transmembrane ion channel [220]. In this numerical observation, we design a new cylindrical channel with the same dimensions by varying atomic surface charges so the electrostatic potential profile has a double-well structure. As illustrated in Fig. 4.16, only the middle section (from $z = -7.67\text{\AA}$ to $z = 7.67\text{\AA}$) of the channel axis is positively charged, but the other parts of the channel are negatively charged. The detailed atomic charge distribution of this channel is given in Table 5.

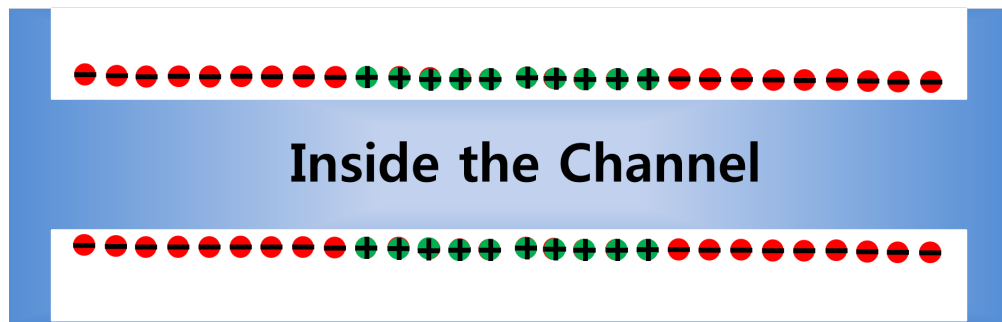


Figure 4.16: The schematic diagram of a three-dimensional double-well nanofluidic channel. The channel length is divided into three parts. The first and last parts are negatively charged, but the middle part is positively charged. The red dots indicate atoms with negative charge $Q_k = -0.12e_c$ and the green dots indicate atoms with positive charge $Q_k = 0.04e_c$.

Effect of applied voltage

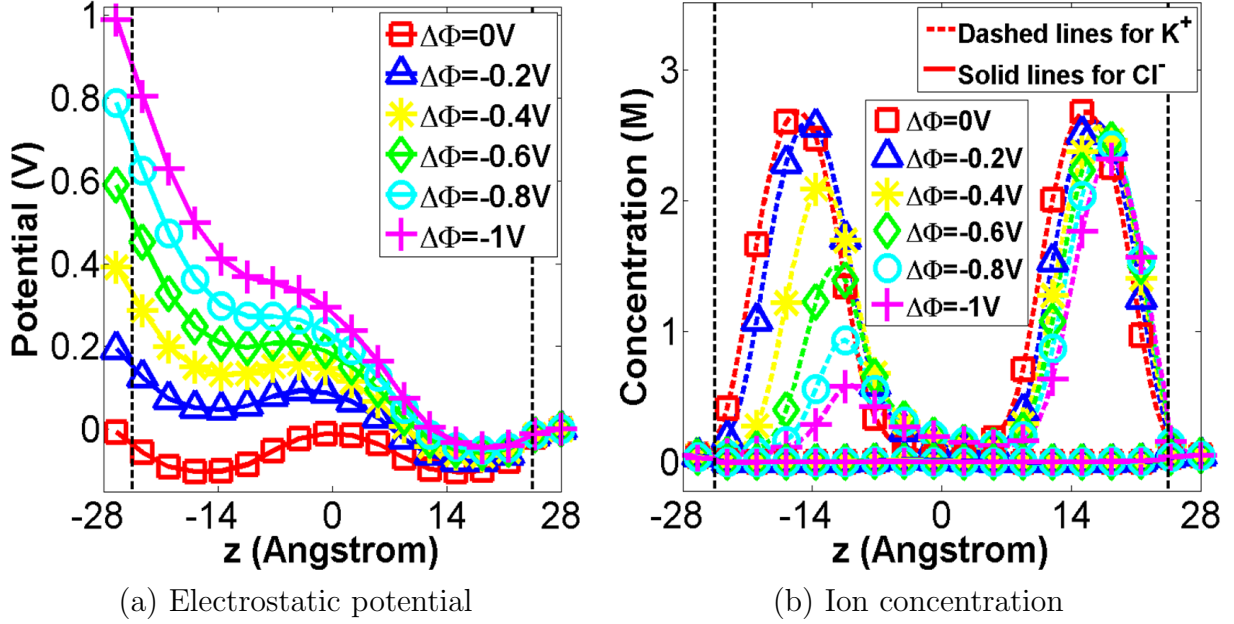


Figure 4.17: Effect of applied voltage on electrostatics and dynamics through the double-well nanofluidic channel. (a) Electrostatic potential profiles and (b) ion concentration distributions along the channel length (z -axis). Here $\Delta\Phi$ is varied from 0V (squares), -0.2V (triangles), -0.4V (asterisks), -0.6V (diamonds), -0.8V (circles) to -1V (plus signs), where $\Delta\Phi$ is the difference of the applied voltage between two ends of the system. The bulk concentration is $C^0 = 0.05M$ for both ions K^+ and Cl^- . Two dashed vertical lines indicate the ends of the cylindrical channel. Each electrostatic potential graph shows two potential wells, which brings about two piles of K^+ ions along the channel axis. Moreover, higher applied voltage at the left end of the system, Φ_L^0 , breaks the symmetry of the potential wells. The left well becomes weaker and the right well becomes stronger.

At first, we alter only the applied voltage, but fix bulk ion concentration at $C^0 = 0.05M$. In this study, Φ_R^0 is set to be 0V and Φ_L^0 is increased gradually from 0V to 1V. Fig. 4.17 presents the electrostatic potential profiles and ionic concentration distributions along the channel length at five different external voltages, that is, $\Delta\Phi = 0V$, $\Delta\Phi = -0.2V$, $\Delta\Phi = -0.4V$, $\Delta\Phi = -0.6V$, $\Delta\Phi = -0.8V$ and $\Delta\Phi = -1V$. With no external voltage bias ($\Delta\Phi = 0V$), the electrostatic potential has two symmetric wells, which brings about two symmetric piles of the K^+ ions. The increase of the voltage applied at the left end of the system leads for the electrostatic potential to get dramatically higher on the left hand side of the inner channel.

As a result, the left potential well is moderated as in Fig. 4.17(a). Parallel to this variation, the positive ion concentration shows a dramatic change on the left hand side (See Figure 4.17(b)). On the contrary, the light change in the potential at the right hand side of the channel inside corresponds to the light change in the concentration profile of cation on the right. The negative atomic charges located around the channel gate electrostatically inhibits the entering of anions, so the concentration distribution of Cl^- is almost always zero as shown in Fig. 4.17(b).

Effect of bulk ion concentration

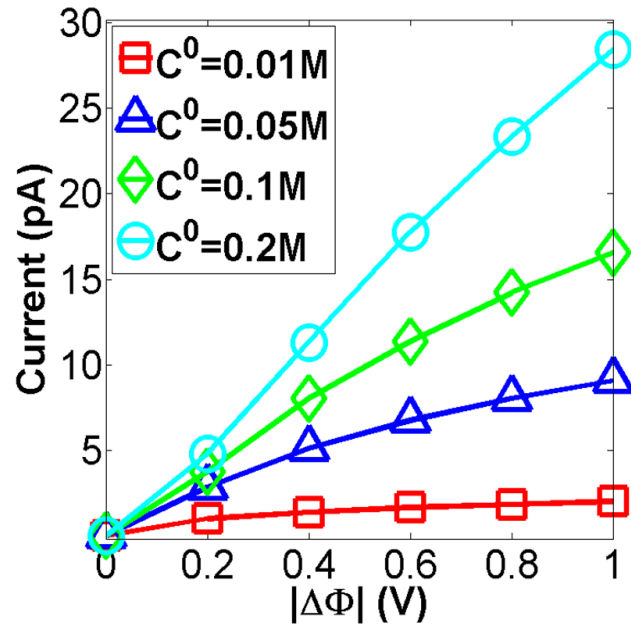


Figure 4.18: Effect of bulk ion concentration on the channel current through the double-well nanofluidic channel. The graphs of total channel current against the external voltage difference (I-V) are studied at four different bulk concentrations: $C^0 = 0.01\text{M}$ (squares), $C^0 = 0.05\text{M}$ (triangles), $C^0 = 0.1\text{M}$ (diamonds), and $C^0 = 0.2\text{M}$ (circles). Higher bulk ion concentration encourages the total current to increase and the I-V characteristic to become linear.

We preform another numerical test with our designed double-well channel. In this test, we only change bulk ion concentration, which is already proved to be an important factor to determine the ion conductance with previous two ion diffusive nanofluidic channels. Herein,

we compare the current-voltage curves at four different bulk ion concentrations, including $C^0 = 0.01\text{M}$, $C^0 = 0.05\text{M}$, $C^0 = 0.1\text{M}$ and $C^0 = 0.2\text{M}$. As in Fig. 4.18, the increase in the total current through the double-well nanochannel is derived from the increase in the bulk ion concentration because more ions are passes from the reservoir to the channel inside. Like the negatively charged channel, the I-V relation becomes linear as the bulk ion concentration gets multiplied because higher bulk ion concentration weakens the double layer within the channel.

The numerical observations of the electrostatic potential, concentration and current through our double-well ionic diffusive nanochannel are qualitatively consistent with those observed from both numerical simulations [220] and experimental measurements [25] of the Gramicidin A channel. Therefore, the present study manifests a great possibility of the atomic design of three dimensional nanofluidic channels in that the synthetic nanofluidic channels with atomic surface charge distribution can be used to study biological channels, which is particularly valuable when the structure is not available.

4.4 Concluding remarks

Recently the dynamics and transport of synthetic nanofluidic channels have received great attention. Parallel to this trend, related experimental techniques and theoretical methods have been substantially promoted in the past two decades [14, 15, 202]. Nanofluidic channels are utilized for a vast variety of scientific and engineering applications, including separation, detection, analysis and synthesis of not only chemicals but also biomolecules. Additionally, inorganic nanochannels are manufactured to imitate biological channels, which is of great significance in elucidating ion selectivity and ion current controllability in response to an

applied field in membrane channels [153, 185]. Molecular and atomic mechanisms are the key ingredients in the design and fabrication of nanofluidic channels. However, atomic details are scarcely considered in nanofluidic modeling and simulation, to our knowledge. Previous simulations of transport in nanofluidic channels have been rarely carried out with three-dimensional (3D) realistic physical geometry.

Present work introduces atomistic design of 3D realistic ionic diffusive nanofluidic channels. The proposed mathematical model and numerical methods are employed for 3D realistic simulations of such nanofluidic systems. Three distinct nanofluidic channels, including a negatively charged nanochannel, a bipolar nanochannel and a double-well nanochannel, are constructed to explore the capability and impact of atomic charges near the channel interface on the channel fluid flow. We design a cylindrical nanofluidic channel of 49\AA in length and 10\AA in diameter. Several charged atoms of about 1.8\AA gap are equally located at 1.5\AA from the channel surface in order to regulate nanofluidic patterns. For a negatively charged channel, all of the atoms on the channel surface have the negative sign with the same charge, whereas for a bipolar channel, half of them has the negative sign and the other half has the positive sign, except that all the charges have the same magnitude. Finally, a double-well channel has positively charged atoms at the middle and negatively charged atoms on the remaining part of the channel surface. Each end of the channel is connected to a reservoir of KCl solution and both reservoirs have the same bulk ion concentration. Asymmetry in the applied electrostatic potentials at the electrodes gives rise to current through these three nanochannels. We perform a number of numerical experiments to explore electrostatic potential, ion concentration and current through each type of ionic diffusive channel under the influence of applied voltage, atomic charge and bulk ion concentration.

The negatively charged channel generates a unipolar charged current because the negative

atomic surface charge attracts counterions, but repels coions. The current measure within this nano-sized channel increases when external voltage, magnitude of atomic charges on the channel surface and/or bulk ion concentration increase. However, the bulk ion concentration has a limitation in its growth. A larger bulk ion concentration shortens the Debye length; thus, the charged channel may behave like an uncharged one showing the Ohm's law in the current-voltage relation. The bipolar channel can create accumulation or depletion of both ions in response to the current direction. When the right electrode has a higher voltage, namely, with forward bias, both ions are stored at the junction of the channel length. On the contrary, when the left electrode has a higher voltage, that is, with reverse bias, both ions are moved away from the junction. External voltage applied at the ends of the system, atomic surface charge and bulk ion concentration affect the amplitude and gradient of the current-voltage characteristic. At last, the special atomic charge distribution of the double-well channel produces the electrostatic potential profile with two potential wells. Increasing applied voltage at the left hand side of the system results in an obvious change both in the left potential well and in the left part of the K^+ concentration.

The present study concludes that properties and quantity of the current through an ionic diffusive nanochannel can be effectively manipulated by carefully altering applied voltage, atomic surface charge and/or bulk ion concentration. Our computational observations are compared well with those of experimental measurements and theoretical analysis in the literature. Since the physical size of our channel model is close to that of realistic transmembrane channels, the proposed nanofluidic model can be utilized not only for ionic diffusive nanofluidic design and simulations, but also for the prediction of membrane channel properties when the structure of the channel protein is not available or changed due to the mutation.

Chapter 5

Thesis achievements and future work

The primary contributions of this dissertation are the mathematical modeling and simulations of a mechanoelectrical transducer (MET) channel prototype and three types of ionic diffusive nanofluidic channels. Both channel models are designed at the microscopic scale and, especially, the atomic charges are employed to explain the gating or surface charge effect. The present thesis study mainly focuses on the electrostatic and transport properties of these channels under several physical conditions, such as applied potential, bulk ion concentration and properties of an atomic charge. In order to explore the dynamics within both channel models, we conduct various three dimensional numerical experiments using an electrodiffusion continuum model, Poisson-Nernst-Planck (PNP) theory. Since these two channel models have similar physical features, they have common mathematical interests and computational challenges. At first, we propose the generalized Poisson-Nernst-Planck model to include non-electrostatic interactions, which are significant factors to determine the transport phenomena within a small nanometer-sized channel. Furthermore, several excellent computational skills are employed to overcome singularities and interface problems.

Most of the materials of this dissertation work are based on the following publications:

- **Jinkyong Park**, Kelin Xia and Guo-Wei Wei, “Atomic scale design and three-dimensional simulation of ionic diffusive nanofluidic channels”, submitted to *Microfluidics and Nanofluidics*

- **Jinkyong Park** and Guo-Wei Wei, “A molecular level prototype for mechanoelectrical transducer in mammalian hair cells, *Journal of Computational Neuroscience*, 35, 231-241, (2013)

5.1 Contributions

5.1.1 On the modeling and simulating a MET channel in mammalian hair cells

In ion channel modeling, one of the most difficult, but vigorous, challenges is to obtain structural information about a target channel in molecular detail. The molecular composition of a biological ion channel is essential to comprehend its major functions including ion selectivity and gating mechanism. In particular, the computational study of the mechanosensitive channel in hair cell has several constraints to elucidate the intrinsic principles of mechanical gating mechanism due to the lack of its molecular building blocks. In this respect, a molecular level channel prototype, which we propose in the present work, contributes to the studies on the MET channel in mammalian hair cells with the following aspects.

First of all, it is the first time to design a MET channel prototype in atomic detail, to our knowledge. In our MET prototype, we incorporate an appropriately charged atom, called a blocker, into the molecular structure of Gramicidin A (GA) channel. The GA channel is very suitable to employ as the channel part of our MET prototype because of its well-established molecular building blocks. Additionally, its structure is comparatively simple and safe to add an ion without worrying about any unexpected complication. Herein, the blocker phenomenologically plays a role of the channel gate because its positive charge prevents the

inward flow of positive ions through this cation channel. The blocker displacement expresses hair bundle deflection, which is believed to activate the MET channel. This molecular-level MET channel model gives a great opportunity to account for the gating mechanism closely.

Secondly, we perform realistic three dimensional simulations of the MET channel transport using the PNP theory. Our group has developed novel mathematical algorithms and useful simulation skills, including Dirichlet to Neumann mapping and the matched interface and boundary method, in order to investigate several proteins and ion channels in the past. In this study, we employ the already proven PNP solver to demonstrate the electrostatic potential profile and current-displacement characteristic through our MET channel prototype. These simulation results in three dimensions can explain the gating principles of the MET channel.

Third, our numerical findings confirm that tip links, which connect hair bundles, are involved in opening and closing the mechanosensitive transduction channels in hair cells. We conduct a number of numerical experiments to analyze electrostatic potential and current under the influence of an external voltage, blocker charge and displacement, and bulk ion concentration. These computational results validate the usefulness and robustness of our proposed MET channel model. Critically, when we compare our results with experimental measurements in the literature, there is a remarkable consistency in terms of the relation between channel open probability and relative displacement. This supports the idea that the tip link is directly connected to the activation of the channel.

5.1.2 On the modeling and simulating charged nanofluidic channels

Nanofluidic channels are studied for diverse scientific and engineering purposes, including separation, detection, analysis and synthesis of chemicals and biomolecules. Although molecular and atomic mechanisms are crucial in designing nanofluidic channels, these details are rarely explained in modeling and simulations to date. In addition, most transport simulations in nanofluidic systems are carried out in one or two dimensional settings. Thus, the second subject of the present study contributes to theoretical nanofluidic studies with the following aspects.

First of all, we introduce the atomistic design of a three dimensional realistic ionic diffusive nanofluidic channel. In our ionic diffusive nanofluidic system, atomic charges are utilized to generate the surface charge of a channel. A number of charged atoms with the same size are equally distributed around the channel structure boundary. One of the greatest strengths of our nanochannel design is the simplicity to create a variety of surface charge distribution. Since individual ions are used to express the fixed charges in the channel structure, we only need to vary the sign and magnitude of each atomic charge. This design method enables treating the surface charge effect more delicately.

Secondly, we propose a variational multiscale framework to facilitate the microscopic description of nanochannel structures, including atomic surface charge, and the macroscopic continuum treatment of the solvent and mobile ions. In this work, we generalize the Poisson-Nernst-Planck model for solid-state nanofluidic channel simulations. We employ a characteristic function \mathcal{S} to identify the channel-solution interface using the predetermined nanofluidic channel structure. Then we incorporate the non-electrostatic interaction term U into the

total energy functional so that the generalized PNP theory is able to simulate very narrow nanochannel. Further, we demonstrate the second order accuracy of our numerical algorithms to solve the standard PNP equations with synthetic ionic diffusive nanochannels, including the negatively charged channel and the bipolar channel.

Finally, we validate the usefulness and great feasibility of our channel model by simulating three types of nanofluidic channels, namely, a negatively charged channel, a bipolar channel and a double-well channel. Our simulation results, including electrostatic potential profile, ion concentration distribution and current-voltage relation through these ionic diffusive channels, show a great agreement with other observations in the literature. These features are very helpful not only to understand the physical properties, but also to predict the functions for each channel type. Especially, the transport behavior through the double-well nanofluidic channel resembles that through a realistic biological ion channel, Gramicidin A channel. This finding opens a great possibility to simulate ion channels when their structures are unknown.

5.2 Future work

Although the Poisson-Nernst-Planck theory is the one of the most widely used microscopic approaches to describe electrokinetic processes in both biological ion channels and artificial nanofluidic channels, it has several limitations. Especially, it ignores non-electrostatic interactions between ions, ion-water and ion-protein, and steric effects which are critical to determine the transport patterns due to a strong confinement or a dilute solution [12, 26, 52, 114]. As much as we understand these inter-particle interactions and atomic physical features, we are able to design a more reasonable mathematical theory and to simulate ion transport through a small pore more quantitatively.

For our future work, modeling and simulation can be substantially developed by incorporating the principles of the following well-established frameworks in the literature. For example, Chen and his colleagues set up the free energy functional of short-range interactions between proton-proton, proton-other mobile ions, proton-water and proton-protein in order to describe the generalized correlation in the proton transport [33]. Each interaction is expressed as a product of the number densities of related particles and the corresponding interaction kernel. Similarly, we can incarnate non-electrostatic interactions between ions, ion-water and ion-protein. As another fruitful computational framework, the density functional theory and its variations have been employed to describe not only equilibrium, but also time-dependent microscopic dynamics [211]. Especially, the time-dependent density functional successfully elucidates the steric effects and intermolecular correlations [111]. Further, its combination with the PNP theory describes well the electrolyte dynamics through a dilute solution [128], and the chemical potentials of ions and the size selectivity of biological ion channels [87, 167]. By including this powerful mathematical insight to our dynamics model, we can simulate more realistic nanofluidic systems.

APPENDICES

A Mathematical algorithms

A.1 Dirichlet to Neumann mapping

Numerical treatment of the Dirac delta function in the Poisson equation may reduce the order of accuracy as well as restrict the mesh size [85]. The Green's function formulation for the singular charges has been adopted for a higher-order interface scheme in the literature [42, 217, 221, 220, 227]. First, the electrostatic potential $\Phi(\mathbf{r})$ is divided into the regular part $\tilde{\Phi}(\mathbf{r})$ and the singular part $\bar{\Phi}(\mathbf{r})$ so that the delta function is eliminated from Eq. (2.8). Here, the singular part $\bar{\Phi}(\mathbf{r})$ is composed of an essential solution of the Poisson equation $\Phi^*(\mathbf{r})$ and a harmonic function $\hat{\Phi}(\mathbf{r})$ [85]. The singular part is only defined in the ion-exclusion region Ω_m because the fixed charges occur only in this region [221]. Specifically, the Green's function is

$$\Phi^*(\mathbf{r}) = \sum_{k=1}^{N_m} \frac{Q_k}{\epsilon_m |\mathbf{r} - \mathbf{r}_k|} \quad (1)$$

and $\hat{\Phi}(\mathbf{r})$ satisfies the Laplace equation with a Dirichlet boundary condition

$$\begin{cases} \nabla^2 \hat{\Phi}(\mathbf{r}) = 0, & \mathbf{r} \in \Omega_m \\ \hat{\Phi}(\mathbf{r}) = -\Phi^*(\mathbf{r}), & \mathbf{r} \in \Gamma. \end{cases} \quad (2)$$

Finally, this decomposition gives the Poisson equation of the regular part $\tilde{\Phi}(\mathbf{r})$ without charge singularities which is

$$-\nabla \cdot (\epsilon(\mathbf{r}) \nabla \tilde{\Phi}(\mathbf{r})) = 4\pi(1 - \chi(\mathbf{r})) \sum_{\alpha=1}^{N_s} q_\alpha C_\alpha(\mathbf{r}), \quad \mathbf{r} \in \Omega, \quad (3)$$

where a factor of 4π is due to the selection of unit [220].

Furthermore, the following two jump conditions at the solvent-channel interface Γ should be enforced in order to ensure the well-posedness of the problem [85].

$$[\tilde{\Phi}(\mathbf{r})] = 0 \quad (4)$$

$$[\epsilon(\mathbf{r})\nabla\tilde{\Phi}(\mathbf{r})] \cdot \mathbf{n} = \epsilon_m \nabla \left(\Phi^*(\mathbf{r}) + \hat{\Phi}(\mathbf{r}) \right) \cdot \mathbf{n}, \quad (5)$$

where \mathbf{n} is the outward normal direction from the interface.

A.2 Matched interface and boundary (MIB) method

The resulting equations (2) and (3) from the DNM algorithm involve material interface Γ and three dimensional irregular geometry. Additionally, their solutions are still non-trivial if the jump conditions (4) and (5) are to be properly enforced for arbitrarily complex interface geometries. If the jump conditions are ignored, discontinuous coefficients and complex geometry may reduce the order of convergence of the numerical scheme to at most one [220]. Our group has proposed and developed an excellent numerical scheme, the matched and interface boundary (MIB) method, to treat not only biological ion channels but also nanofluidic systems with a higher order of accuracy [34, 32, 220]. In this section, we will briefly elucidate the fundamental principles about the MIB method.

At first, every node in a computation domain is classified as either an irregular point or a regular point. A point near the interface or boundary is called an irregular point, but otherwise, it is called a regular point. The standard second order central finite difference method is enough to interpolate at regular points. However, the application of the seven-point finite difference scheme at an irregular point may result in divergence or reduce the order of convergence due to the discontinuity of the functions involved. Thus, we need to carefully

deal with these points to obtain the convergence at the desired order of accuracy, especially the second order of accuracy, in this dissertation work. If a discretization of $\widehat{\Phi}$ in Eq. (2) involves any value from the region Ω_s , it is replaced by the function value at the intersecting node between the interface Γ and a Cartesian grid line. The difference scheme of Eq. (2.19) is precisely modified according to the local geometry and the type of boundary condition and, additionally, the detailed equations are discussed in the references [217, 220]. To calculate $\widetilde{\Phi}(\mathbf{r})$ numerically at irregular points from the interface problem (3), the MIB algorithm employs fictitious values and auxiliary points.

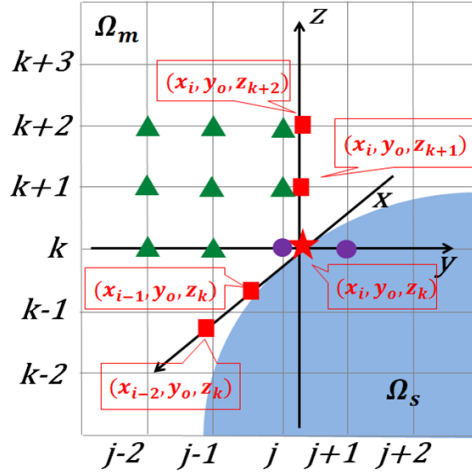


Figure 1: An illustration of the MIB method for an irregular geometry. The k th grid line intersects the interface at (x_i, y_o, z_k) (star), which involves two irregular points (circle) (x_i, y_j, z_k) and (x_i, y_{j+1}, z_k) . Here (x_i, y_o, z_{k+2}) and (x_i, y_o, z_{k+1}) (square) are two auxiliary points needed to discretize $(\epsilon\widetilde{\Phi}_z)_z$ and (x_{i-1}, y_o, z_k) and (x_{i-2}, y_o, z_k) (square) are two auxiliary points needed to discretize $(\epsilon\widetilde{\Phi}_x)_x$. The other points (triangle) indicate the points selected to interpolate $\widetilde{\Phi}$ along the y -grid lines at (x_i, y_o, z_k) , (x_i, y_o, z_{k+1}) and (x_i, y_o, z_{k+2}) .

For example, if the interface crosses the k th mesh line as illustrated in Fig. 1, then (x_i, y_j, z_k) and (x_i, y_{j+1}, z_k) are irregular points. The discretizations of $(\epsilon\widetilde{\Phi}_y)_y$ at these two irregular points contain two fictitious values $f_{i,j,k}$ and $f_{i,j+1,k}$ to extend the domain as

follows:

$$\begin{aligned}
(\epsilon \tilde{\Phi}_y)_y &= \frac{\epsilon_{i,j-\frac{1}{2},k} \tilde{\Phi}_{i,j-1,k} - (\epsilon_{i,j-\frac{1}{2},k} + \epsilon_{i,j+\frac{1}{2},k}) \tilde{\Phi}_{i,j,k} + \epsilon_{i,j+\frac{1}{2},k} f_{i,j+1,k}}{(\Delta y)^2} \quad \text{at } (x_i, y_j, z_k) \\
(\epsilon \tilde{\Phi}_y)_y &= \frac{\epsilon_{i,j+\frac{1}{2},k} f_{i,j,k} - (\epsilon_{i,j+\frac{1}{2},k} + \epsilon_{i,j+\frac{3}{2},k}) \tilde{\Phi}_{i,j+1,k} + \epsilon_{i,j+\frac{3}{2},k} \tilde{\Phi}_{i,j+2,k}}{(\Delta y)^2} \quad \text{at } (x_i, y_{j+1}, z_k).
\end{aligned}$$

Herein, the fictitious values are determined by the jump conditions (4) and (5) at the point of intersection (x_i, y_o, z_k) between the interface and the y -mesh line.

Since the normal direction from the interface Γ changes according to the position of the intersecting point, we employ a local coordinate (ξ, η, ζ) at this point, where ξ is the normal direction, η is the tangential direction and ζ is the binormal direction. This introduction of a local coordinate system leads the interface problem to become a one-dimensional problem [217]. At the point (x_i, y_o, z_k) , the standard coordinate system is converted to a new coordinate system using the following matrix equation

$$\begin{bmatrix} \xi \\ \eta \\ \zeta \end{bmatrix} = T \begin{bmatrix} x \\ y \\ z \end{bmatrix} = \begin{bmatrix} \sin \phi \cos \theta & \sin \phi \sin \theta & \cos \phi \\ -\sin \theta & \cos \theta & 0 \\ -\cos \phi \cos \theta & -\cos \phi \sin \theta & \sin \phi \end{bmatrix} \begin{bmatrix} x \\ y \\ z \end{bmatrix},$$

where ϕ and θ are, respectively, the azimuth and zenith angles determined by the normal direction \mathbf{n} . This transformation also results in three jump conditions at each direction:

$$[\epsilon \tilde{\Phi}_\xi] = T_{11}(\epsilon_s \tilde{\Phi}_x^s - \epsilon_m \tilde{\Phi}_x^m) + T_{12}(\epsilon_s \tilde{\Phi}_y^s - \epsilon_m \tilde{\Phi}_y^m) + T_{13}(\epsilon_s \tilde{\Phi}_z^s - \epsilon_m \tilde{\Phi}_z^m) \quad (6)$$

$$[\tilde{\Phi}_\eta] = T_{21}(\tilde{\Phi}_x^s - \tilde{\Phi}_x^m) + T_{22}(\tilde{\Phi}_y^s - \tilde{\Phi}_y^m) \quad (7)$$

$$[\tilde{\Phi}_\zeta] = T_{31}(\tilde{\Phi}_x^s - \tilde{\Phi}_x^m) + T_{32}(\tilde{\Phi}_y^s - \tilde{\Phi}_y^m) + T_{33}(\tilde{\Phi}_z^s - \tilde{\Phi}_z^m), \quad (8)$$

where T_{ij} is the element in the i th row and j th column of the matrix T . $[\epsilon\tilde{\Phi}_\xi]$ is from the equation (5), but $[\tilde{\Phi}_\eta]$ and $[\tilde{\Phi}_\zeta]$ are obtained by differentiating the equation (4) [217]. These jump conditions involve six partial derivatives $\tilde{\Phi}_x^s, \tilde{\Phi}_y^s, \tilde{\Phi}_z^s, \tilde{\Phi}_x^m, \tilde{\Phi}_y^m$ and $\tilde{\Phi}_z^m$. When the geometry is non-smooth or complex, some of them may be quite challenging to calculate. We obtain four jump conditions from (4) through (8) that we can use, but the number of the fictitious values we need to find is only two. Therefore, we do not need to find all of the above six partial derivatives. In this respect, we want to remove two partial derivatives which are the most difficult to discretize by two jump conditions [217]. In Fig. 1, $\tilde{\Phi}_x^s$ and $\tilde{\Phi}_z^s$ are chosen to be eliminated, which leads to

$$a_1[\epsilon\tilde{\Phi}_\xi] + a_2[\tilde{\Phi}_\eta] + a_3[\tilde{\Phi}_\zeta] = c_1\tilde{\Phi}_x^m + c_2\tilde{\Phi}_y^m + c_3\tilde{\Phi}_y^s + c_4\tilde{\Phi}_z^m, \quad (9)$$

where $a_1 = T_{21}T_{33}$, $a_2 = \epsilon_s(T_{31}T_{13} - T_{33}T_{11})$ and $a_3 = -\epsilon_s T_{13}T_{21}$. Then the discretizations of the remaining four partial derivatives require several auxiliary points. Finally, solving a system of equations (4) and (9) produces the values of $f_{i,j,k}$ and $f_{i,j+1,k}$. More comprehensive details are available in the literature [217, 224]. In summary, the MIB scheme manages interface problems in a well-organized way by using fictitious values, simple Cartesian coordinate, typical finite difference methods and lower order physical jump conditions [221].

A.3 Iterations of Poisson and Nernst-Planck equations

In our modeling, we employ the following iterative procedure which is also concisely described in the flowchart (See Fig. 2). First, the boundary value problem of Eq. (2) is required to solve for $\hat{\Phi}$ only at the first step because this equation does not involve ionic concentrations C_α . Next, the equations (2.19) and (3) are solved iteratively with suitable boundary conditions of

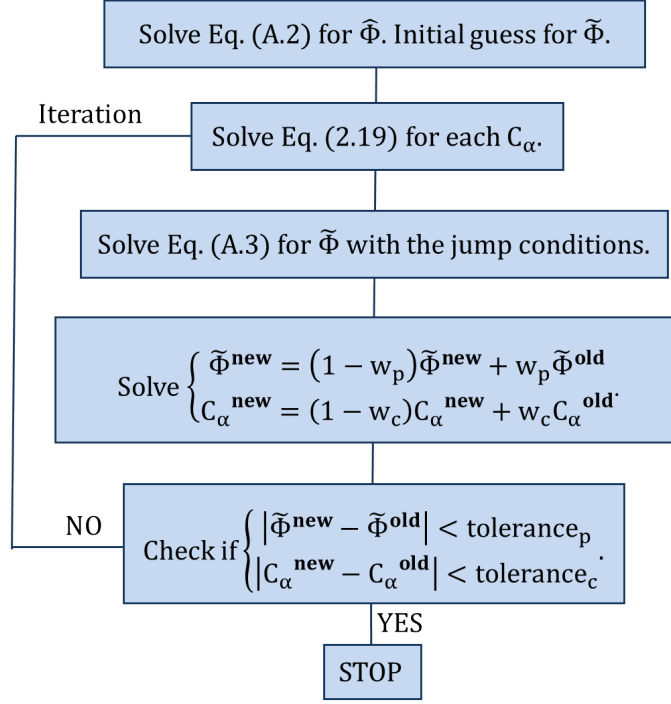


Figure 2: Flowchart of the numerical implementation to solve the standard PNP system

applied voltage and bulk ion concentration until the designated tolerances for $\tilde{\Phi}$ and C_α are reached. To ensure that the numerical process is convergent, $\tilde{\Phi}$ and C_α are updated by a successive over relaxation (SOR)-like iterations

$$\tilde{\Phi}^{\text{new}} = (1 - w_p) \tilde{\Phi}^{\text{new}} + w_p \tilde{\Phi}^{\text{old}} \quad (10)$$

$$C_\alpha^{\text{new}} = (1 - w_c) C_\alpha^{\text{new}} + w_c C_\alpha^{\text{old}}, \quad (11)$$

where w_p and w_c are appropriately selected between 0 and 1. This procedure has been already proved to be efficient for ion channel problems with the second order of accuracy [220].

After the electrostatic potential Φ and the ionic concentration C_α are obtained by solving Eqs. (2.19), (2) and (3), the electric current is computed at each circular cross section inside

the channel along the channel axis [220]. For each ionic species α , its current is calculated by

$$I_\alpha = q_\alpha \int_S D_\alpha \left[\frac{\partial C_\alpha}{\partial z} + \frac{q_\alpha}{k_B T} C_\alpha \frac{\partial \Phi}{\partial z} \right] dx dy, \quad (12)$$

where S is the cross section in the xy -plane. Further, the total channel current is the sum of two ionic currents.

B Unit system

For real physical simulations with atomic detail, such as biological ion channels and synthetic nanofluidic channels, the PNP equations cannot be directly treated as a dimensionless problem [220]. Pertinent units, which are consistent with fundamental physical laws and central physical constants, should be employed. Consequently, the quantities computed from the PNP system can be directly compared with experimental observations and measurements. To this end, we discuss the units of the PNP model in our simulation work.

Table 1: Centimeter-Gram-Second system of units

Abbr.	Unit	Represents
cm	centimeter	distance
esu	electrostatic unit	charge
mol	mole	quantity
K	Kelvin	temperature

In electrostatics, the essential units are based on the centimeter-gram-second system shown in Table 1 [102]. In our work, we employ the Gaussian units introduced in Table 2 so that we construct the dimensionless electrostatic potential $u(\mathbf{r})$ and the dimensionless charges \bar{q}_α and \bar{Q}_k [102, 220]. Moreover, the required parameters are Avagadro’s number $N_A = 6.0220450 \times 10^{23}$, Boltzmann’s constant $k_B = 1.3806620 \times 10^{-16}$ erg/K and elementary charge $e_c = 4.80320425 \times 10^{-10}$ esu.

Table 2: Gaussian units

Abbr.	Unit	Represents	Equivalent Expressions
Å	angstrom	distance	10^{-8}cm
l	liter	volume	cm^3
M	molar	concentration	mol/l
dyn	dyne	force	esu^2/cm^2
erg	erg	energy	$\text{dyn}\cdot\text{cm}$

In our simulation system, the radii of all atoms and the structural dimensions are given in terms of angstrom (Å). Then the applied voltage is in the unit of volt (V) and the concentration for each ion species is provided in molar (M).

For the unit conversion as mentioned in our earlier work [220], we define the dimensionless electrostatic potential $u(\mathbf{r}) = \frac{e_c \Phi(\mathbf{r})}{k_B T}$ and the dimensionless partial charge $\bar{Q}_k = \frac{Q_k}{e_c}$ at k th atomic component of the channel region. For each ion species α , the dimensionless charge and the dimensionless concentration are, respectively, defined as $\bar{q}_\alpha = \frac{q_\alpha}{e_c}$ and $\bar{C}_\alpha(\mathbf{r}) = \frac{e_c^2}{k_B T} C_\alpha(\mathbf{r})$. Then the electrical charges for K^+ and Cl^- are, respectively, denoted by $\bar{q}_1 = \bar{q}_{\text{K}^+} = 1$ and $\bar{q}_2 = \bar{q}_{\text{Cl}^-} = -1$. The Dirichlet boundary conditions for the electrostatic potential and ionic concentration are modified in the following way:

$$u_L^0 = \frac{\Phi_L^0 e_c}{300 k_B T}, \quad u_R^0 = \frac{\Phi_R^0 e_c}{300 k_B T} \quad \text{and} \quad \bar{C}_\alpha^0 = \frac{C_\alpha^0 N_A \text{\AA}^2 e_c^2}{1000 k_B T}.$$

Finally, the PNP equations (3) and (2.19) are transformed into

$$\begin{cases} -\nabla \cdot (\epsilon(\mathbf{r}) \nabla \tilde{u}(\mathbf{r})) = 4\pi \sum_{\alpha=1}^{N_s} \bar{q}_\alpha \bar{C}_\alpha(\mathbf{r}), & \mathbf{r} \in \Omega \\ \nabla \cdot D_\alpha(\mathbf{r}) [\nabla \bar{C}_\alpha(\mathbf{r}) + \bar{q}_\alpha \bar{C}_\alpha(\mathbf{r}) \nabla \tilde{u}(\mathbf{r})] = 0, & \mathbf{r} \in \Omega_s \end{cases} \quad (13)$$

together with the Laplace equation for the microscopic channel composition

$$\begin{cases} \nabla^2 \hat{u}(\mathbf{r}) = 0, & \mathbf{r} \in \Omega_m \\ \hat{u}(\mathbf{r}) = -u^*(\mathbf{r}), & \mathbf{r} \in \Gamma, \end{cases} \quad (14)$$

where $u^*(\mathbf{r}) = \sum_{k=1}^{N_m} \frac{\bar{Q}_k}{\epsilon_m |\mathbf{r} - \mathbf{r}_k|}$. In our simulations of two subjects, i.e. the MET prototype and ionic diffusive nanofluidic channels, we solve the above three equations with the interface

jump conditions $[\tilde{u}(\mathbf{r})]$ and $[\epsilon(\mathbf{r})\tilde{u}(\mathbf{r})]$ from Eqs. (4) and (5), and proper boundary conditions. In addition, we utilize the dimensionless values of the dielectric function $\epsilon(\mathbf{r})$ which are empirically determined [102].

$$\epsilon(\mathbf{r}) = \begin{cases} \epsilon_s = 80, & \mathbf{r} \in \Omega_s \\ \epsilon_m = 2, & \mathbf{r} \in \Omega_m. \end{cases} \quad (15)$$

It is also significant to deal with boundary conditions for the electrostatic potential and concentrations carefully. Theoretically, the electrostatic potential $u(\mathbf{r})$ satisfies the far field boundary condition, that is, $\lim_{x \rightarrow \pm\infty} u(\mathbf{r}) = 0$. In our computation, we need mixed boundary conditions. Specifically, the Poisson equation uses Dirichlet boundary condition at two electrodes of $\partial\Omega$ where the external voltage is applied [220], i.e., $u(\mathbf{r}) = u_L^0$ at anode and $u(\mathbf{r}) = u_R^0$ at cathode. Neumann boundary conditions are considered on the other parts of $\partial\Omega$. In practice, the boundary conditions except the applied voltages are somewhat irrelevant as long as boundaries are sufficiently far from the channel pore [220, 221].

Mixed boundary conditions are also applied to Nernst-Planck equations for all ion species. Since the Nernst-Planck equation is only defined in the ion inclusion region Ω_s , it is enough to consider the boundary of Ω_s . On $\partial\Omega \cap \partial\Omega_s$, $\bar{C}_\alpha = \bar{C}_\alpha^0$, where \bar{C}_α^0 represents the bulk ion concentration for species α . However, at the interface $\Gamma = \Omega_s \cap \Omega_m$, the concentration satisfies the following zero-flux condition $-D_\alpha(\mathbf{r}) [\nabla \bar{C}_\alpha(\mathbf{r}) + \bar{q}_\alpha \bar{C}_\alpha(\mathbf{r}) \nabla \tilde{u}(\mathbf{r})] = \mathbf{0}$, where $\mathbf{0} = (0, 0, 0)$ is a null vector.

C Atomic charge distribution

C.1 A negatively charged channel

Table 3: Positions and charges of all atomic charges in the negatively charged channel.

k	$x(\text{\AA})$	$y(\text{\AA})$	$z(\text{\AA})$	$Q_k(e_c)$	k	$x(\text{\AA})$	$y(\text{\AA})$	$z(\text{\AA})$	$Q_k(e_c)$	k	$x(\text{\AA})$	$y(\text{\AA})$	$z(\text{\AA})$	$Q_k(e_c)$	k	$x(\text{\AA})$	$y(\text{\AA})$	$z(\text{\AA})$	$Q_k(e_c)$
1	6.5000	0.0000	-23.0000	-0.08	57	6.5000	0.0000	-11.0741	-0.08	113	6.5000	0.0000	0.8519	-0.08	169	6.5000	0.0000	12.7778	-0.08
2	4.5962	4.5962	-23.0000	-0.08	58	4.5962	4.5962	-11.0741	-0.08	114	4.5962	4.5962	0.8519	-0.08	170	4.5962	4.5962	12.7778	-0.08
3	0.0000	6.5000	-23.0000	-0.08	59	0.0000	6.5000	-11.0741	-0.08	115	0.0000	6.5000	0.8519	-0.08	171	0.0000	6.5000	12.7778	-0.08
4	-4.5962	4.5962	-23.0000	-0.08	60	-4.5962	4.5962	-11.0741	-0.08	116	-4.5962	4.5962	0.8519	-0.08	172	-4.5962	4.5962	12.7778	-0.08
5	-6.5000	0.0000	-23.0000	-0.08	61	-6.5000	0.0000	-11.0741	-0.08	117	-6.5000	0.0000	0.8519	-0.08	173	-6.5000	0.0000	12.7778	-0.08
6	-4.5962	-4.5962	-23.0000	-0.08	62	-4.5962	-4.5962	-11.0741	-0.08	118	-4.5962	-4.5962	0.8519	-0.08	174	-4.5962	-4.5962	12.7778	-0.08
7	0.0000	-6.5000	-23.0000	-0.08	63	0.0000	-6.5000	-11.0741	-0.08	119	0.0000	-6.5000	0.8519	-0.08	175	0.0000	-6.5000	12.7778	-0.08
8	4.5962	-4.5962	-23.0000	-0.08	64	4.5962	-4.5962	-11.0741	-0.08	120	4.5962	-4.5962	0.8519	-0.08	176	4.5962	-4.5962	12.7778	-0.08
9	6.5000	0.0000	-21.2963	-0.08	65	6.5000	0.0000	-9.3704	-0.08	121	6.5000	0.0000	2.5556	-0.08	177	6.5000	0.0000	14.4815	-0.08
10	4.5962	4.5962	-21.2963	-0.08	66	4.5962	4.5962	-9.3704	-0.08	122	4.5962	4.5962	2.5556	-0.08	178	4.5962	4.5962	14.4815	-0.08
11	0.0000	6.5000	-21.2963	-0.08	67	0.0000	6.5000	-9.3704	-0.08	123	0.0000	6.5000	2.5556	-0.08	179	0.0000	6.5000	14.4815	-0.08
12	-4.5962	4.5962	-21.2963	-0.08	68	-4.5962	4.5962	-9.3704	-0.08	124	-4.5962	4.5962	2.5556	-0.08	180	-4.5962	4.5962	14.4815	-0.08
13	-6.5000	0.0000	-21.2963	-0.08	69	-6.5000	0.0000	-9.3704	-0.08	125	-6.5000	0.0000	2.5556	-0.08	181	-6.5000	0.0000	14.4815	-0.08
14	-4.5962	-4.5962	-21.2963	-0.08	70	-4.5962	-4.5962	-9.3704	-0.08	126	-4.5962	-4.5962	2.5556	-0.08	182	-4.5962	-4.5962	14.4815	-0.08
15	0.0000	-6.5000	-21.2963	-0.08	71	0.0000	-6.5000	-9.3704	-0.08	127	0.0000	-6.5000	2.5556	-0.08	183	0.0000	-6.5000	14.4815	-0.08
16	4.5962	-4.5962	-21.2963	-0.08	72	4.5962	-4.5962	-9.3704	-0.08	128	4.5962	-4.5962	2.5556	-0.08	184	4.5962	-4.5962	14.4815	-0.08
17	6.5000	0.0000	-19.5926	-0.08	73	6.5000	0.0000	-7.6667	-0.08	129	6.5000	0.0000	4.2593	-0.08	185	6.5000	0.0000	16.1852	-0.08
18	4.5962	4.5962	-19.5926	-0.08	74	4.5962	4.5962	-7.6667	-0.08	130	4.5962	4.5962	4.2593	-0.08	186	4.5962	4.5962	16.1852	-0.08
19	0.0000	6.5000	-19.5926	-0.08	75	0.0000	6.5000	-7.6667	-0.08	131	0.0000	6.5000	4.2593	-0.08	187	0.0000	6.5000	16.1852	-0.08
20	-4.5962	4.5962	-19.5926	-0.08	76	-4.5962	4.5962	-7.6667	-0.08	132	-4.5962	4.5962	4.2593	-0.08	188	-4.5962	4.5962	16.1852	-0.08
21	-6.5000	0.0000	-19.5926	-0.08	77	-6.5000	0.0000	-7.6667	-0.08	133	-6.5000	0.0000	4.2593	-0.08	189	-6.5000	0.0000	16.1852	-0.08
22	-4.5962	-4.5962	-19.5926	-0.08	78	-4.5962	-4.5962	-7.6667	-0.08	134	-4.5962	-4.5962	4.2593	-0.08	190	-4.5962	-4.5962	16.1852	-0.08
23	0.0000	-6.5000	-19.5926	-0.08	79	0.0000	-6.5000	-7.6667	-0.08	135	0.0000	-6.5000	4.2593	-0.08	191	0.0000	-6.5000	16.1852	-0.08
24	4.5962	-4.5962	-19.5926	-0.08	80	4.5962	-4.5962	-7.6667	-0.08	136	4.5962	-4.5962	4.2593	-0.08	192	4.5962	-4.5962	16.1852	-0.08
25	6.5000	0.0000	-17.8889	-0.08	81	6.5000	0.0000	-5.9630	-0.08	137	6.5000	0.0000	5.9630	-0.08	193	6.5000	0.0000	17.8889	-0.08
26	4.5962	4.5962	-17.8889	-0.08	82	4.5962	4.5962	-5.9630	-0.08	138	4.5962	4.5962	5.9630	-0.08	194	4.5962	4.5962	17.8889	-0.08
27	0.0000	6.5000	-17.8889	-0.08	83	0.0000	6.5000	-5.9630	-0.08	139	0.0000	6.5000	5.9630	-0.08	195	0.0000	6.5000	17.8889	-0.08
28	-4.5962	4.5962	-17.8889	-0.08	84	-4.5962	4.5962	-5.9630	-0.08	140	-4.5962	4.5962	5.9630	-0.08	196	-4.5962	4.5962	17.8889	-0.08
29	-6.5000	0.0000	-17.8889	-0.08	85	-6.5000	0.0000	-5.9630	-0.08	141	-6.5000	0.0000	5.9630	-0.08	197	-6.5000	0.0000	17.8889	-0.08
30	-4.5962	-4.5962	-17.8889	-0.08	86	-4.5962	-4.5962	-5.9630	-0.08	142	-4.5962	-4.5962	5.9630	-0.08	198	-4.5962	-4.5962	17.8889	-0.08
31	0.0000	-6.5000	-17.8889	-0.08	87	0.0000	-6.5000	-5.9630	-0.08	143	0.0000	-6.5000	5.9630	-0.08	199	0.0000	-6.5000	17.8889	-0.08
32	4.5962	-4.5962	-17.8889	-0.08	88	4.5962	-4.5962	-5.9630	-0.08	144	4.5962	-4.5962	5.9630	-0.08	200	4.5962	-4.5962	17.8889	-0.08
33	6.5000	0.0000	-16.1852	-0.08	89	6.5000	0.0000	-4.2593	-0.08	145	6.5000	0.0000	7.6667	-0.08	201	6.5000	0.0000	19.5926	-0.08
34	4.5962	4.5962	-16.1852	-0.08	90	4.5962	4.5962	-4.2593	-0.08	146	4.5962	4.5962	7.6667	-0.08	202	4.5962	4.5962	19.5926	-0.08
35	0.0000	6.5000	-16.1852	-0.08	91	0.0000	6.5000	-4.2593	-0.08	147	0.0000	6.5000	7.6667	-0.08	203	0.0000	6.5000	19.5926	-0.08
36	-4.5962	4.5962	-16.1852	-0.08	92	-4.5962	4.5962	-4.2593	-0.08	148	-4.5962	4.5962	7.6667	-0.08	204	-4.5962	4.5962	19.5926	-0.08
37	-6.5000	0.0000	-16.1852	-0.08	93	-6.5000	0.0000	-4.2593	-0.08	149	-6.5000	0.0000	7.6667	-0.08	205	-6.5000	0.0000	19.5926	-0.08
38	-4.5962	-4.5962	-16.1852	-0.08	94	-4.5962	-4.5962	-4.2593	-0.08	150	-4.5962	-4.5962	7.6667	-0.08	206	-4.5962	-4.5962	19.5926	-0.08
39	0.0000	-6.5000	-16.1852	-0.08	95	0.0000	-6.5000	-4.2593	-0.08	151	0.0000	-6.5000	7.6667	-0.08	207	0.0000	-6.5000	19.5926	-0.08
40	4.5962	-4.5962	-16.1852	-0.08	96	4.5962	-4.5962	-4.2593	-0.08	152	4.5962	-4.5962	7.6667	-0.08	208	4.5962	-4.5962	19.5926	-0.08
41	6.5000	0.0000	-14.4815	-0.08	97	6.5000	0.0000	-2.5556	-0.08	153	6.5000	0.0000	9.3704	-0.08	209	6.5000	0.0000	21.2963	-0.08
42	4.5962	4.5962	-14.4815	-0.08	98	4.5962	4.5962	-2.5556	-0.08	154	4.5962	4.5962	9.3704	-0.08	210	4.5962	4.5962	21.2963	-0.08
43	0.0000	6.5000	-14.4815	-0.08	99	0.0000	6.5000	-2.5556	-0.08	155	0.0000	6.5000	9.3704	-0.08	211	0.0000	6.5000	21.2963	-0.08
44	-4.5962	4.5962	-14.4815	-0.08	100	-4.5962	4.5962	-2.5556	-0.08	156	-4.5962	4.5962	9.3704	-0.08	212	-4.5962	4.5962	21.2963	-0.08
45	-6.5000	0.0000	-14.4815	-0.08	101	-6.5000	0.0000	-2.5556	-0.08	157	-6.5000	0.0000	9.3704	-0.08	213	-6.5000	0.0000	21.2963	-0.08
46	-4.5962	-4.5962	-14.4815	-0.08	102	-4.5962	-4.5962	-2.5556	-0.08	158	-4.5962	-4.5962	9.3704	-0.08	214	-4.5962	-4.5962	21.2963	-0.08
47	0.0000	-6.5000	-14.4815	-0.08	103	0.0000	-6.5000	-2.5556	-0.08	159	0.0000	-6.5000	9.3704	-0.08	215	0.0000	-6.5000	21.2963	-0.08
48	4.5962	-4.5962	-14.4815	-0.08	104	4.5962	-4.5962	-2.5556	-0.08	160	4.5962	-4.5962	9.3704	-0.08	216	4.5962	-4.5962	21.2963	-0.08
49	6.5000	0.0000	-12.7778	-0.08	105	6.5000	0.0000	-0.8519	-0.08	161	6.5000	0.0000	11.0741	-0.08	217	6.5000	0.0000	23.0000	-0.08
50	4.5962	4.5962	-12.7778	-0.08	106	4.5962	-4.5962	-0.8519	-0.08	162	4.5962	4.5962	11.0741	-0.08	218	4.5962	4.5962	23.0000	-0.08
51	0.0000	6.5000	-12.7778	-0.08	107	0.0000	-6.5000	-0.8519	-0.08	163	0.0000	6.5000	11.0741	-0.08	219	0.0000	6.5000	23.0000	-0.08
52	-4.5962	4.5962	-12.7778	-0.08	108	-4.5962	4.5962	-0.8519	-0.08	164	-4.5962	4.5962	11.0741	-0.08	220	-4.5962	4.5962	23.0000	-0.08
53	-6.5000	0.0000	-12.7778	-0.08	109	-6.5000	0.0000	-0.8519	-0.08	165	-6.5000	0.0000	11.0741	-0.08	221	-6.5000	0.0000	23.0000	-0.08
54	-4.5962	-4.5962	-12.7778	-0.08	110	-4.5962	-4.5962	-0.8519	-0.08	166	-4.5962	-4.5962	11.0741	-0.08	222	-4.5962	-4.5962	23.0000	-0.08
55	0.0000	-6.5000	-12.7778	-0.08	111	0.0000	-6.5000	-0.8519	-0.08	167	0.0000	-6.5000	11.0741	-0.08	223	0.0000	-6.5000	23.0000	-0.08
56	4.5962	-4.5962	-12.7778	-0.08	112	4.5962	-4.5962	-0.8519	-0.08	168	4.5962	-4.5962	11.0741	-0.08	224	4.5962	-4.5962	23.0000	-0.08

C.2 A bipolar channel

Table 4: Positions and charges of all atomic charges in the bipolar channel.

k	$x(\text{\AA})$	$y(\text{\AA})$	$z(\text{\AA})$	$Q_k(e_c)$	k	$x(\text{\AA})$	$y(\text{\AA})$	$z(\text{\AA})$	$Q_k(e_c)$	k	$x(\text{\AA})$	$y(\text{\AA})$	$z(\text{\AA})$	$Q_k(e_c)$	k	$x(\text{\AA})$	$y(\text{\AA})$	$z(\text{\AA})$	$Q_k(e_c)$
1	6.5000	0.0000	-23.0000	0.08	57	6.5000	0.0000	-11.0741	0.08	113	6.5000	0.0000	0.8519	-0.08	169	6.5000	0.0000	12.7778	-0.08
2	4.5962	4.5962	-23.0000	0.08	58	4.5962	4.5962	-11.0741	0.08	114	4.5962	4.5962	0.8519	-0.08	170	4.5962	4.5962	12.7778	-0.08
3	0.0000	6.5000	-23.0000	0.08	59	0.0000	6.5000	-11.0741	0.08	115	0.0000	6.5000	0.8519	-0.08	171	0.0000	6.5000	12.7778	-0.08
4	-4.5962	4.5962	-23.0000	0.08	60	-4.5962	4.5962	-11.0741	0.08	116	-4.5962	4.5962	0.8519	-0.08	172	-4.5962	4.5962	12.7778	-0.08
5	-6.5000	0.0000	-23.0000	0.08	61	-6.5000	0.0000	-11.0741	0.08	117	-6.5000	0.0000	0.8519	-0.08	173	-6.5000	0.0000	12.7778	-0.08
6	-4.5962	-4.5962	-23.0000	0.08	62	-4.5962	-4.5962	-11.0741	0.08	118	-4.5962	-4.5962	0.8519	-0.08	174	-4.5962	-4.5962	12.7778	-0.08
7	0.0000	-6.5000	-23.0000	0.08	63	0.0000	-6.5000	-11.0741	0.08	119	0.0000	-6.5000	0.8519	-0.08	175	0.0000	-6.5000	12.7778	-0.08
8	4.5962	-4.5962	-23.0000	0.08	64	4.5962	-4.5962	-11.0741	0.08	120	4.5962	-4.5962	0.8519	-0.08	176	4.5962	-4.5962	12.7778	-0.08
9	6.5000	0.0000	-21.2963	0.08	65	6.5000	0.0000	-9.3704	0.08	121	6.5000	0.0000	2.5556	-0.08	177	6.5000	0.0000	14.4815	-0.08
10	4.5962	4.5962	-21.2963	0.08	66	4.5962	4.5962	-9.3704	0.08	122	4.5962	4.5962	2.5556	-0.08	178	4.5962	4.5962	14.4815	-0.08
11	0.0000	6.5000	-21.2963	0.08	67	0.0000	6.5000	-9.3704	0.08	123	0.0000	6.5000	2.5556	-0.08	179	0.0000	6.5000	14.4815	-0.08
12	-4.5962	4.5962	-21.2963	0.08	68	-4.5962	4.5962	-9.3704	0.08	124	-4.5962	4.5962	2.5556	-0.08	180	-4.5962	4.5962	14.4815	-0.08
13	-6.5000	0.0000	-21.2963	0.08	69	-6.5000	0.0000	-9.3704	0.08	125	-6.5000	0.0000	2.5556	-0.08	181	-6.5000	0.0000	14.4815	-0.08
14	-4.5962	-4.5962	-21.2963	0.08	70	-4.5962	-4.5962	-9.3704	0.08	126	-4.5962	-4.5962	2.5556	-0.08	182	-4.5962	-4.5962	14.4815	-0.08
15	0.0000	-6.5000	-21.2963	0.08	71	0.0000	-6.5000	-9.3704	0.08	127	0.0000	-6.5000	2.5556	-0.08	183	0.0000	-6.5000	14.4815	-0.08
16	4.5962	-4.5962	-21.2963	0.08	72	4.5962	-4.5962	-9.3704	0.08	128	4.5962	-4.5962	2.5556	-0.08	184	4.5962	-4.5962	14.4815	-0.08
17	6.5000	0.0000	-19.5926	0.08	73	6.5000	0.0000	-7.6667	0.08	129	6.5000	0.0000	4.2593	-0.08	185	6.5000	0.0000	16.1852	-0.08
18	4.5962	4.5962	-19.5926	0.08	74	4.5962	4.5962	-7.6667	0.08	130	4.5962	4.5962	4.2593	-0.08	186	4.5962	4.5962	16.1852	-0.08
19	0.0000	6.5000	-19.5926	0.08	75	0.0000	6.5000	-7.6667	0.08	131	0.0000	6.5000	4.2593	-0.08	187	0.0000	6.5000	16.1852	-0.08
20	-4.5962	4.5962	-19.5926	0.08	76	-4.5962	4.5962	-7.6667	0.08	132	-4.5962	4.5962	4.2593	-0.08	188	-4.5962	4.5962	16.1852	-0.08
21	-6.5000	0.0000	-19.5926	0.08	77	-6.5000	0.0000	-7.6667	0.08	133	-6.5000	0.0000	4.2593	-0.08	189	-6.5000	0.0000	16.1852	-0.08
22	-4.5962	-4.5962	-19.5926	0.08	78	-4.5962	-4.5962	-7.6667	0.08	134	-4.5962	-4.5962	4.2593	-0.08	190	-4.5962	-4.5962	16.1852	-0.08
23	0.0000	-6.5000	-19.5926	0.08	79	0.0000	-6.5000	-7.6667	0.08	135	0.0000	-6.5000	4.2593	-0.08	191	0.0000	-6.5000	16.1852	-0.08
24	4.5962	-4.5962	-19.5926	0.08	80	4.5962	-4.5962	-7.6667	0.08	136	4.5962	-4.5962	4.2593	-0.08	192	4.5962	-4.5962	16.1852	-0.08
25	6.5000	0.0000	-17.8889	0.08	81	6.5000	0.0000	-5.9630	0.08	137	6.5000	0.0000	5.9630	-0.08	193	6.5000	0.0000	17.8889	-0.08
26	4.5962	4.5962	-17.8889	0.08	82	4.5962	4.5962	-5.9630	0.08	138	4.5962	4.5962	5.9630	-0.08	194	4.5962	4.5962	17.8889	-0.08
27	0.0000	6.5000	-17.8889	0.08	83	0.0000	6.5000	-5.9630	0.08	139	0.0000	6.5000	5.9630	-0.08	195	0.0000	6.5000	17.8889	-0.08
28	-4.5962	4.5962	-17.8889	0.08	84	-4.5962	4.5962	-5.9630	0.08	140	-4.5962	4.5962	5.9630	-0.08	196	-4.5962	4.5962	17.8889	-0.08
29	-6.5000	0.0000	-17.8889	0.08	85	-6.5000	0.0000	-5.9630	0.08	141	-6.5000	0.0000	5.9630	-0.08	197	-6.5000	0.0000	17.8889	-0.08
30	-4.5962	-4.5962	-17.8889	0.08	86	-4.5962	-4.5962	-5.9630	0.08	142	-4.5962	-4.5962	5.9630	-0.08	198	-4.5962	-4.5962	17.8889	-0.08
31	0.0000	-6.5000	-17.8889	0.08	87	0.0000	-6.5000	-5.9630	0.08	143	0.0000	-6.5000	5.9630	-0.08	199	0.0000	-6.5000	17.8889	-0.08
32	4.5962	-4.5962	-17.8889	0.08	88	4.5962	-4.5962	-5.9630	0.08	144	4.5962	-4.5962	5.9630	-0.08	200	4.5962	-4.5962	17.8889	-0.08
33	6.5000	0.0000	-16.1852	0.08	89	6.5000	0.0000	-4.2593	0.08	145	6.5000	0.0000	7.6667	-0.08	201	6.5000	0.0000	19.5926	-0.08
34	4.5962	4.5962	-16.1852	0.08	90	4.5962	4.5962	-4.2593	0.08	146	4.5962	4.5962	7.6667	-0.08	202	4.5962	4.5962	19.5926	-0.08
35	0.0000	6.5000	-16.1852	0.08	91	0.0000	6.5000	-4.2593	0.08	147	0.0000	6.5000	7.6667	-0.08	203	0.0000	6.5000	19.5926	-0.08
36	-4.5962	4.5962	-16.1852	0.08	92	-4.5962	4.5962	-4.2593	0.08	148	-4.5962	4.5962	7.6667	-0.08	204	-4.5962	4.5962	19.5926	-0.08
37	-6.5000	0.0000	-16.1852	0.08	93	-6.5000	0.0000	-4.2593	0.08	149	-6.5000	0.0000	7.6667	-0.08	205	-6.5000	0.0000	19.5926	-0.08
38	-4.5962	-4.5962	-16.1852	0.08	94	-4.5962	-4.5962	-4.2593	0.08	150	-4.5962	-4.5962	7.6667	-0.08	206	-4.5962	-4.5962	19.5926	-0.08
39	0.0000	-6.5000	-16.1852	0.08	95	0.0000	-6.5000	-4.2593	0.08	151	0.0000	-6.5000	7.6667	-0.08	207	0.0000	-6.5000	19.5926	-0.08
40	4.5962	-4.5962	-16.1852	0.08	96	4.5962	-4.5962	-4.2593	0.08	152	4.5962	-4.5962	7.6667	-0.08	208	4.5962	-4.5962	19.5926	-0.08
41	6.5000	0.0000	-14.4815	0.08	97	6.5000	0.0000	-2.5556	0.08	153	6.5000	0.0000	9.3704	-0.08	209	6.5000	0.0000	21.2963	-0.08
42	4.5962	4.5962	-14.4815	0.08	98	4.5962	4.5962	-2.5556	0.08	154	4.5962	4.5962	9.3704	-0.08	210	4.5962	4.5962	21.2963	-0.08
43	0.0000	6.5000	-14.4815	0.08	99	0.0000	6.5000	-2.5556	0.08	155	0.0000	6.5000	9.3704	-0.08	211	0.0000	6.5000	21.2963	-0.08
44	-4.5962	4.5962	-14.4815	0.08	100	-4.5962	4.5962	-2.5556	0.08	156	-4.5962	4.5962	9.3704	-0.08	212	-4.5962	4.5962	21.2963	-0.08
45	-6.5000	0.0000	-14.4815	0.08	101	-6.5000	0.0000	-2.5556	0.08	157	-6.5000	0.0000	9.3704	-0.08	213	-6.5000	0.0000	21.2963	-0.08
46	-4.5962	-4.5962	-14.4815	0.08	102	-4.5962	-4.5962	-2.5556	0.08	158	-4.5962	-4.5962	9.3704	-0.08	214	-4.5962	-4.5962	21.2963	-0.08
47	0.0000	-6.5000	-14.4815	0.08	103	0.0000	-6.5000	-2.5556	0.08	159	0.0000	-6.5000	9.3704	-0.08	215	0.0000	-6.5000	21.2963	-0.08
48	4.5962	-4.5962	-14.4815	0.08	104	4.5962	-4.5962	-2.5556	0.08	160	4.5962	-4.5962	9.3704	-0.08	216	4.5962	-4.5962	21.2963	-0.08
49	6.5000	0.0000	-12.7778	0.08	105	6.5000	0.0000	-0.8519	0.08	161	6.5000	0.0000	11.0741	-0.08	217	6.5000	0.0000	23.0000	-0.08
50	4.5962	4.5962	-12.7778	0.08	106	4.5962	-4.5962	-0.8519	0.08	162	4.5962	4.5962	11.0741	-0.08	218	4.5962	4.5962	23.0000	-0.08
51	0.0000	6.5000	-12.7778	0.08	107	0.0000	-6.5000	-0.8519	0.08	163	0.0000	6.5000	11.0741	-0.08	219	0.0000	6.5000	23.0000	-0.08
52	-4.5962	4.5962	-12.7778	0.08	108	-4.5962	-4.5962	-0.8519	0.08	164	-4.5962	4.5962	11.0741	-0.08	220	-4.5962	4.5962	23.0000	-0.08
53	-6.5000	0.0000	-12.7778	0.08	109	-6.5000	0.0000	-0.8519	0.08	165	-6.5000	0.0000	11.0741	-0.08	221	-6.5000	0.0000	23.0000	-0.08
54	-4.5962	-4.5962	-12.7778	0.08	110	-4.5962	-4.5962	-0.8519	0.08	166	-4.5962	-4.5962	11.0741	-0.08	222	-4.5962	-4.5962	23.0000	-0.08
55	0.0000	-6.5000	-12.7778	0.08	111	0.0000	-6.5000	-0.8519	0.08	167	0.0000	-6.5000	11.0741	-0.08	223	0.0000	-6.5000	23.0000	-0.08
56	4.5962	-4.5962	-12.7778	0.08	112	4.5962	-4.5962	-0.8519	0.08	168	4.5962	-4.5962	11.0741	-0.08	224	4.5962	-4.5962	23.0000	-0.08

C.3 A double-well channel

Table 5: Positions and charges of all atomic charges in the double well channel.

k	$x(\text{\AA})$	$y(\text{\AA})$	$z(\text{\AA})$	$Q_k(e_c)$	k	$x(\text{\AA})$	$y(\text{\AA})$	$z(\text{\AA})$	$Q_k(e_c)$	k	$x(\text{\AA})$	$y(\text{\AA})$	$z(\text{\AA})$	$Q_k(e_c)$	k	$x(\text{\AA})$	$y(\text{\AA})$	$z(\text{\AA})$	$Q_k(e_c)$
1	6.5000	0.0000	-23.0000	-0.12	57	6.5000	0.0000	-11.0741	-0.12	113	6.5000	0.0000	0.8519	0.04	169	6.5000	0.0000	12.7778	-0.12
2	4.5962	4.5962	-23.0000	-0.12	58	4.5962	4.5962	-11.0741	-0.12	114	4.5962	4.5962	0.8519	0.04	170	4.5962	4.5962	12.7778	-0.12
3	0.0000	6.5000	-23.0000	-0.12	59	0.0000	6.5000	-11.0741	-0.12	115	0.0000	6.5000	0.8519	0.04	171	0.0000	6.5000	12.7778	-0.12
4	-4.5962	4.5962	-23.0000	-0.12	60	-4.5962	4.5962	-11.0741	-0.12	116	-4.5962	4.5962	0.8519	0.04	172	-4.5962	4.5962	12.7778	-0.12
5	-6.5000	0.0000	-23.0000	-0.12	61	-6.5000	0.0000	-11.0741	-0.12	117	-6.5000	0.0000	0.8519	0.04	173	-6.5000	0.0000	12.7778	-0.12
6	-4.5962	-4.5962	-23.0000	-0.12	62	-4.5962	-4.5962	-11.0741	-0.12	118	-4.5962	-4.5962	0.8519	0.04	174	-4.5962	-4.5962	12.7778	-0.12
7	0.0000	-6.5000	-23.0000	-0.12	63	0.0000	-6.5000	-11.0741	-0.12	119	0.0000	-6.5000	0.8519	0.04	175	0.0000	-6.5000	12.7778	-0.12
8	4.5962	-4.5962	-23.0000	-0.12	64	4.5962	-4.5962	-11.0741	-0.12	120	4.5962	-4.5962	0.8519	0.04	176	4.5962	-4.5962	12.7778	-0.12
9	6.5000	0.0000	-21.2963	-0.12	65	6.5000	0.0000	-9.3704	-0.12	121	6.5000	0.0000	2.5556	0.04	177	6.5000	0.0000	14.4815	-0.12
10	4.5962	4.5962	-21.2963	-0.12	66	4.5962	4.5962	-9.3704	-0.12	122	4.5962	4.5962	2.5556	0.04	178	4.5962	4.5962	14.4815	-0.12
11	0.0000	6.5000	-21.2963	-0.12	67	0.0000	6.5000	-9.3704	-0.12	123	0.0000	6.5000	2.5556	0.04	179	0.0000	6.5000	14.4815	-0.12
12	-4.5962	4.5962	-21.2963	-0.12	68	-4.5962	4.5962	-9.3704	-0.12	124	-4.5962	4.5962	2.5556	0.04	180	-4.5962	4.5962	14.4815	-0.12
13	-6.5000	0.0000	-21.2963	-0.12	69	-6.5000	0.0000	-9.3704	-0.12	125	-6.5000	0.0000	2.5556	0.04	181	-6.5000	0.0000	14.4815	-0.12
14	-4.5962	-4.5962	-21.2963	-0.12	70	-4.5962	-4.5962	-9.3704	-0.12	126	-4.5962	-4.5962	2.5556	0.04	182	-4.5962	-4.5962	14.4815	-0.12
15	0.0000	-6.5000	-21.2963	-0.12	71	0.0000	-6.5000	-9.3704	-0.12	127	0.0000	-6.5000	2.5556	0.04	183	0.0000	-6.5000	14.4815	-0.12
16	4.5962	-4.5962	-21.2963	-0.12	72	4.5962	-4.5962	-9.3704	-0.12	128	4.5962	-4.5962	2.5556	0.04	184	4.5962	-4.5962	14.4815	-0.12
17	6.5000	0.0000	-19.5926	-0.12	73	6.5000	0.0000	-7.6667	0.04	129	6.5000	0.0000	4.2593	0.04	185	6.5000	0.0000	16.1852	-0.12
18	4.5962	4.5962	-19.5926	-0.12	74	4.5962	4.5962	-7.6667	0.04	130	4.5962	4.5962	4.2593	0.04	186	4.5962	4.5962	16.1852	-0.12
19	0.0000	6.5000	-19.5926	-0.12	75	0.0000	6.5000	-7.6667	0.04	131	0.0000	6.5000	4.2593	0.04	187	0.0000	6.5000	16.1852	-0.12
20	-4.5962	4.5962	-19.5926	-0.12	76	-4.5962	4.5962	-7.6667	0.04	132	-4.5962	4.5962	4.2593	0.04	188	-4.5962	4.5962	16.1852	-0.12
21	-6.5000	0.0000	-19.5926	-0.12	77	-6.5000	0.0000	-7.6667	0.04	133	-6.5000	0.0000	4.2593	0.04	189	-6.5000	0.0000	16.1852	-0.12
22	-4.5962	-4.5962	-19.5926	-0.12	78	-4.5962	-4.5962	-7.6667	0.04	134	-4.5962	-4.5962	4.2593	0.04	190	-4.5962	-4.5962	16.1852	-0.12
23	0.0000	-6.5000	-19.5926	-0.12	79	0.0000	-6.5000	-7.6667	0.04	135	0.0000	-6.5000	4.2593	0.04	191	0.0000	-6.5000	16.1852	-0.12
24	4.5962	-4.5962	-19.5926	-0.12	80	4.5962	-4.5962	-7.6667	0.04	136	4.5962	-4.5962	4.2593	0.04	192	4.5962	-4.5962	16.1852	-0.12
25	6.5000	0.0000	-17.8889	-0.12	81	6.5000	0.0000	-5.9630	0.04	137	6.5000	0.0000	5.9630	0.04	193	6.5000	0.0000	17.8889	-0.12
26	4.5962	4.5962	-17.8889	-0.12	82	4.5962	4.5962	-5.9630	0.04	138	4.5962	4.5962	5.9630	0.04	194	4.5962	4.5962	17.8889	-0.12
27	0.0000	6.5000	-17.8889	-0.12	83	0.0000	6.5000	-5.9630	0.04	139	0.0000	6.5000	5.9630	0.04	195	0.0000	6.5000	17.8889	-0.12
28	-4.5962	4.5962	-17.8889	-0.12	84	-4.5962	4.5962	-5.9630	0.04	140	-4.5962	4.5962	5.9630	0.04	196	-4.5962	4.5962	17.8889	-0.12
29	-6.5000	0.0000	-17.8889	-0.12	85	-6.5000	0.0000	-5.9630	0.04	141	-6.5000	0.0000	5.9630	0.04	197	-6.5000	0.0000	17.8889	-0.12
30	-4.5962	-4.5962	-17.8889	-0.12	86	-4.5962	-4.5962	-5.9630	0.04	142	-4.5962	-4.5962	5.9630	0.04	198	-4.5962	-4.5962	17.8889	-0.12
31	0.0000	-6.5000	-17.8889	-0.12	87	0.0000	-6.5000	-5.9630	0.04	143	0.0000	-6.5000	5.9630	0.04	199	0.0000	-6.5000	17.8889	-0.12
32	4.5962	-4.5962	-17.8889	-0.12	88	4.5962	-4.5962	-5.9630	0.04	144	4.5962	-4.5962	5.9630	0.04	200	4.5962	-4.5962	17.8889	-0.12
33	6.5000	0.0000	-16.1852	-0.12	89	6.5000	0.0000	-4.2593	0.04	145	6.5000	0.0000	7.6667	0.04	201	6.5000	0.0000	19.5926	-0.12
34	4.5962	4.5962	-16.1852	-0.12	90	4.5962	4.5962	-4.2593	0.04	146	4.5962	4.5962	7.6667	0.04	202	4.5962	4.5962	19.5926	-0.12
35	0.0000	6.5000	-16.1852	-0.12	91	0.0000	6.5000	-4.2593	0.04	147	0.0000	6.5000	7.6667	0.04	203	0.0000	6.5000	19.5926	-0.12
36	-4.5962	4.5962	-16.1852	-0.12	92	-4.5962	4.5962	-4.2593	0.04	148	-4.5962	4.5962	7.6667	0.04	204	-4.5962	4.5962	19.5926	-0.12
37	-6.5000	0.0000	-16.1852	-0.12	93	-6.5000	0.0000	-4.2593	0.04	149	-6.5000	0.0000	7.6667	0.04	205	-6.5000	0.0000	19.5926	-0.12
38	-4.5962	-4.5962	-16.1852	-0.12	94	-4.5962	-4.5962	-4.2593	0.04	150	-4.5962	-4.5962	7.6667	0.04	206	-4.5962	-4.5962	19.5926	-0.12
39	0.0000	-6.5000	-16.1852	-0.12	95	0.0000	-6.5000	-4.2593	0.04	151	0.0000	-6.5000	7.6667	0.04	207	0.0000	-6.5000	19.5926	-0.12
40	4.5962	-4.5962	-16.1852	-0.12	96	4.5962	-4.5962	-4.2593	0.04	152	4.5962	-4.5962	7.6667	0.04	208	4.5962	-4.5962	19.5926	-0.12
41	6.5000	0.0000	-14.4815	-0.12	97	6.5000	0.0000	-2.5556	0.04	153	6.5000	0.0000	9.3704	-0.12	209	6.5000	0.0000	21.2963	-0.12
42	4.5962	4.5962	-14.4815	-0.12	98	4.5962	4.5962	-2.5556	0.04	154	4.5962	4.5962	9.3704	-0.12	210	4.5962	4.5962	21.2963	-0.12
43	0.0000	6.5000	-14.4815	-0.12	99	0.0000	6.5000	-2.5556	0.04	155	0.0000	6.5000	9.3704	-0.12	211	0.0000	6.5000	21.2963	-0.12
44	-4.5962	4.5962	-14.4815	-0.12	100	-4.5962	4.5962	-2.5556	0.04	156	-4.5962	4.5962	9.3704	-0.12	212	-4.5962	4.5962	21.2963	-0.12
45	-6.5000	0.0000	-14.4815	-0.12	101	-6.5000	0.0000	-2.5556	0.04	157	-6.5000	0.0000	9.3704	-0.12	213	-6.5000	0.0000	21.2963	-0.12
46	-4.5962	-4.5962	-14.4815	-0.12	102	-4.5962	-4.5962	-2.5556	0.04	158	-4.5962	-4.5962	9.3704	-0.12	214	-4.5962	-4.5962	21.2963	-0.12
47	0.0000	-6.5000	-14.4815	-0.12	103	0.0000	-6.5000	-2.5556	0.04	159	0.0000	-6.5000	9.3704	-0.12	215	0.0000	-6.5000	21.2963	-0.12
48	4.5962	-4.5962	-14.4815	-0.12	104	4.5962	-4.5962	-2.5556	0.04	160	4.5962	-4.5962	9.3704	-0.12	216	4.5962	-4.5962	21.2963	-0.12
49	6.5000	0.0000	-12.7778	-0.12	105	6.5000	0.0000	-0.8519	0.04	161	6.5000	0.0000	11.0741	-0.12	217	6.5000	0.0000	23.0000	-0.12
50	4.5962	4.5962	-12.7778	-0.12	106	4.5962	-4.5962	-0.8519	0.04	162	4.5962	4.5962	11.0741	-0.12	218	4.5962	4.5962	23.0000	-0.12
51	0.0000	6.5000	-12.7778	-0.12	107	0.0000	-6.5000	-0.8519	0.04	163	0.0000	6.5000	11.0741	-0.12	219	0.0000	6.5000	23.0000	-0.12
52	-4.5962	4.5962	-12.7778	-0.12	108	-4.5962	-4.5962	-0.8519	0.04	164	-4.5962	4.5962	11.0741	-0.12	220	-4.5962	4.5962	23.0000	-0.12
53	-6.5000	0.0000	-12.7778	-0.12	109	-6.5000	0.0000	-0.8519	0.04	165	-6.5000	0.0000	11.0741	-0.12	221	-6.5000	0.0000	23.0000	-0.12
54	-4.5962	-4.5962	-12.7778	-0.12	110	-4.5962	-4.5962	-0.8519	0.04	166	-4.5962	-4.5962	11.0741	-0.12	222	-4.5962	-4.5962	23.0000	-0.12
55	0.0000	-6.5000	-12.7778	-0.12	111	0.0000	-6.5000	-0.8519	0.04	167	0.0000	-6.5000	11.0741	-0.12	223	0.0000	-6.5000	23.0000	-0.12
56	4.5962	-4.5962	-12.7778	-0.12	112	4.5962	-4.5962	-0.8519	0.04	168	4.5962	-4.5962	11.0741	-0.12	224	4.5962	-4.5962	23.0000	-0.12

BIBLIOGRAPHY

BIBLIOGRAPHY

- [1] P. Abgrall and N. T. Nguyen. Nanofluidic devices and their applications. *Analytical chemistry*, 80(7):2326–2341, 2008.
- [2] H. Adalsteinsson, B. J. Debuschere, K. R. Long, and H. N. Najm. Components for atomistic-to-continuum multiscale modeling of flow in micro-and nanofluidic systems. *Scientific Programming*, 16(4):297–313, 2008.
- [3] M. Aguilera-Arzo, J. J. García-Celma, J. Cervera, A. Alcaraz, and V. M. Aguilera. Electrostatic properties and macroscopic electrodiffusion in OmpF porin and mutants. *Bioelectrochemistry*, 70(2):320–327, 2007.
- [4] A. Aksimentiev and K. Schulten. Imaging α -hemolysin with molecular dynamics: Ionic conductance, osmotic permeability, and the electrostatic potential map. *Biophysical journal*, 88(6):3745–3761, 2005.
- [5] W. L. Ash, M. R. Zlomislic, E. O. Oloo, and D. P. Tieleman. Computer simulations of membrane proteins. *Biochimica et Biophysica Acta (BBA)-Biomembranes*, 1666(1):158–189, 2004.
- [6] A. J. Bard and L. R. Faulkner. *Electrochemical methods: fundamentals and applications*, volume 2. Wiley New York, 1980.
- [7] G. Barreiro, C. R. W. Guimarães, and R. B. de Alencastro. A molecular dynamics study of an L-type calcium channel model. *Protein engineering*, 15(2):109–122, 2002.
- [8] D. Bashford and D. A. Case. Generalized Born models of macromolecular solvation effects. *Annual Review of Physical Chemistry*, 51(1):129–152, 2000.
- [9] R. B. Bass, P. Strop, M. Barclay, and D. C. Rees. Crystal structure of Escherichia coli MscS, a voltage-modulated and mechanosensitive channel. *Science*, 298(5598):1582–1587, 2002.
- [10] P. Bates, Z. Chen, Y. Sun, G.-W. Wei, and S. Zhao. Geometric and potential driving formation and evolution of biomolecular surfaces. *Journal of mathematical biology*, 59(2):193–231, 2009.
- [11] P. Bates, G.-W. Wei, and S. Zhao. Minimal molecular surfaces and their applications. *Journal of Computational Chemistry*, 29(3):380–391, 2008.
- [12] M. Z. Bazant, M. S. Kilic, B. D. Storey, and A. Ajdari. Towards an understanding of induced-charge electrokinetics at large applied voltages in concentrated solutions. *Advances in colloid and interface science*, 152(1):48–88, 2009.

- [13] M. Z. Bazant, B. D. Storey, and A. A. Kornyshev. Double layer in ionic liquids: Overscreening versus crowding. *Physical Review Letters*, 106(4):046102, 2011.
- [14] M. Z. Bazant, K. Thornton, and A. Ajdari. Diffuse-charge dynamics in electrochemical systems. *Physical review E*, 70(2):021506, 2004.
- [15] P. Belgrader, M. Okuzumi, F. Pourahmadi, D. A. Borkholder, and M. A. Northrup. A microfluidic cartridge to prepare spores for PCR analysis. *Biosensors and bioelectronics*, 14(10):849–852, 2000.
- [16] M. Beurg, R. Fettiplace, J.-H. Nam, and A. J. Ricci. Localization of inner hair cell mechanotransducer channels using high-speed calcium imaging. *Nature neuroscience*, 12(5):553–558, 2009.
- [17] M. Beurg, J.-H. Nam, Q. Chen, and R. Fettiplace. Calcium balance and mechanotransduction in rat cochlear hair cells. *Journal of neurophysiology*, 104(1):18–34, 2010.
- [18] M. Beurg, J.-H. Nam, A. Crawford, and R. Fettiplace. The actions of calcium on hair bundle mechanics in mammalian cochlear hair cells. *Biophysical journal*, 94(7):2639–2653, 2008.
- [19] F. Bezanilla. Ion channels: from conductance to structure. *Neuron*, 60(3):456–468, 2008.
- [20] I. Biró, S. Pezeshki, H. Weingart, M. Winterhalter, and U. Kleinekathöfer. Comparing the temperature-dependent conductance of the two structurally similar E. coli Porins OmpC and OmpF. *Biophysical journal*, 98(9):1830–1839, 2010.
- [21] A. Borisyuk. Physiology and mathematical modeling of the auditory system. In *Tutorials in Mathematical Biosciences I*, pages 107–168. Springer, 2005.
- [22] D. Branton, D. W. Deamer, A. Marziali, H. Bayley, S. A. Benner, T. Butler, M. Di Ventra, S. Garaj, A. Hibbs, X. Huang, et al. The potential and challenges of nanopore sequencing. *Nature biotechnology*, 26(10):1146–1153, 2008.
- [23] B. R. Brooks, R. E. Bruccoleri, B. D. Olafson, D. J. States, S. Swaminathan, and M. Karplus. Charmm: A program for macromolecular energy, minimization, and dynamics calculations. *Journal of computational chemistry*, 4(2):187–217, 1983.
- [24] D. Burch and M. Z. Bazant. Size-dependent spinodal and miscibility gaps for intercalation in nanoparticles. *Nano letters*, 9(11):3795–3800, 2009.
- [25] D. D. Busath, C. D. Thulin, R. W. Hendershot, L. R. Phillips, P. Maughan, C. D. Cole, N. C. Bingham, S. Morrison, L. C. Baird, R. J. Hendershot, et al. Noncontact dipole effects on channel permeation. I. Experiments with (5F-Indole) Trp Gramicidin A channels. *Biophysical journal*, 75(6):2830–2844, 1998.
- [26] H.-J. Butt, K. Graf, and M. Kappl. *Physics and chemistry of interfaces*. John Wiley & Sons, 2006.

- [27] J. Cervera, B. Schiedt, and P. Ramirez. A Poisson/Nernst-Planck model for ionic transport through synthetic conical nanopores. *EPL (Europhysics Letters)*, 71(1):35, 2005.
- [28] G. Chang, R. H. Spencer, A. T. Lee, M. T. Barclay, and D. C. Rees. Structure of the MscL homolog from *Mycobacterium tuberculosis*: a gated mechanosensitive ion channel. *Science*, 282(5397):2220–2226, 1998.
- [29] D. L. Chapman. A contribution to the theory of electrocapillarity. *The London, Edinburgh, and Dublin Philosophical Magazine and Journal of Science*, 25(148):475–481, 1913.
- [30] D. Chen, Z. Chen, and G.-W. Wei. Quantum dynamics in continuum for proton transport II: Variational solvent–solute interface. *International journal for numerical methods in biomedical engineering*, 28(1):25–51, 2012.
- [31] D. Chen and R. Eisenberg. Charges, currents, and potentials in ionic channels of one conformation. *Biophysical journal*, 64(5):1405–1421, 1993.
- [32] D. Chen and G.-W. Wei. Modeling and simulation of electronic structure, material interface and random doping in nano-electronic devices. *Journal of computational physics*, 229(12):4431–4460, 2010.
- [33] D. Chen and G.-W. Wei. Quantum dynamics in continuum for proton transport – Generalized correlation. *The Journal of chemical physics*, 136(13):134109, 2012.
- [34] D. Chen and G.-W. Wei. Quantum dynamics in continuum for proton transport I: Basic formulation. *Communications in computational physics*, 13(1):285, 2013.
- [35] D. P. Chen, R. S. Eisenberg, J. W. Jerome, and C.-W. Shu. Hydrodynamic model of temperature change in open ionic channels. *Biophysical journal*, 69(6):2304–2322, 1995.
- [36] L. Chen and A. Conlisk. Electroosmotic flow and particle transport in micro/nano nozzles and diffusers. *Biomedical microdevices*, 10(2):289–298, 2008.
- [37] S. Chen and G. D. Doolen. Lattice Boltzmann method for fluid flows. *Annual review of fluid mechanics*, 30(1):329–364, 1998.
- [38] Z. Chen, N. A. Baker, and G. Wei. Differential geometry based solvation model II: Lagrangian formulation. *Journal of mathematical biology*, 63(6):1139–1200, 2011.
- [39] Z. Chen, N. A. Baker, and G.-W. Wei. Differential geometry based solvation model I: Eulerian formulation. *Journal of computational physics*, 229(22):8231–8258, 2010.
- [40] Z. Chen, S. Zhao, J. Chun, D. G. Thomas, N. A. Baker, P. W. Bates, and G. Wei. Variational approach for nonpolar solvation analysis. *The Journal of chemical physics*, 137(8):084101, 2012.
- [41] L.-J. Cheng and L. J. Guo. Nanofluidic diodes. *Chemical Society Reviews*, 39(3):923–938, 2010.

- [42] I.-L. Chern, J.-G. Liu, W.-C. Wang, et al. Accurate evaluation of electrostatics for macromolecules in solution. *Methods and Applications of Analysis*, 10(2):309–328, 2003.
- [43] Y. S. Choi and S. J. Kim. Electrokinetic flow-induced currents in silica nanofluidic channels. *Journal of colloid and interface science*, 333(2):672–678, 2009.
- [44] T. Chou. Enhancement of charged macromolecule capture by nanopores in a salt gradient. *The Journal of chemical physics*, 131(3):034703, 2009.
- [45] K. T. Chu and M. Z. Bazant. Nonlinear electrochemical relaxation around conductors. *Physical Review E*, 74(1):011501, 2006.
- [46] S.-H. Chung and B. Corry. Three computational methods for studying permeation, selectivity and dynamics in biological ion channels. *Soft Matter*, 1(6):417–427, 2005.
- [47] S.-H. Chung, M. Hoyles, T. Allen, and S. Kuyucak. Study of ionic currents across a model membrane channel using Brownian dynamics. *Biophysical Journal*, 75(2):793–809, 1998.
- [48] S.-H. Chung and S. Kuyucak. Recent advances in ion channel research. *Biochimica et Biophysica Acta (BBA)-Biomembranes*, 1565(2):267–286, 2002.
- [49] R. D. Coalson and M. G. Kurnikova. Poisson–Nernst–Planck theory approach to the calculation of current through biological ion channels. *IEEE transactions on nanobioscience*, 4(1):81–93, 2005.
- [50] D. Constantin and Z. S. Siwy. Poisson-Nernst-Planck model of ion current rectification through a nanofluidic diode. *Physical Review E*, 76(4):041202, 2007.
- [51] W. D. Cornell, P. Cieplak, C. I. Bayly, I. R. Gould, K. M. Merz, D. M. Ferguson, D. C. Spellmeyer, T. Fox, J. W. Caldwell, and P. A. Kollman. A second generation force field for the simulation of proteins, nucleic acids, and organic molecules. *Journal of the American Chemical Society*, 117(19):5179–5197, 1995.
- [52] B. Corry, S. Kuyucak, and S.-H. Chung. Tests of continuum theories as models of ion channels. II. Poisson–Nernst–Planck theory versus Brownian dynamics. *Biophysical Journal*, 78(5):2364–2381, 2000.
- [53] E. R. Cruz-Chu, A. Aksimentiev, and K. Schulten. Ionic current rectification through silica nanopores. *The Journal of Physical Chemistry C*, 113(5):1850–1862, 2009.
- [54] É. Csányi, D. Boda, D. Gillespie, and T. Kristóf. Current and selectivity in a model sodium channel under physiological conditions: Dynamic Monte Carlo simulations. *Biochimica et Biophysica Acta (BBA)-Biomembranes*, 1818(3):592–600, 2012.
- [55] H. Daiguji. Ion transport in nanofluidic channels. *Chemical Society Reviews*, 39(3):901–911, 2010.
- [56] H. Daiguji, Y. Oka, and K. Shirono. Nanofluidic diode and bipolar transistor. *Nano Letters*, 5(11):2274–2280, 2005.

- [57] H. Daiguji, P. Yang, and A. Majumdar. Ion transport in nanofluidic channels. *Nano Letters*, 4(1):137–142, 2004.
- [58] H. Daiguji, P. Yang, A. J. Szeri, and A. Majumdar. Electrochemomechanical energy conversion in nanofluidic channels. *Nano letters*, 4(12):2315–2321, 2004.
- [59] M. E. Davis and J. A. McCammon. Electrostatics in biomolecular structure and dynamics. *Chemical Reviews*, 90(3):509–521, 1990.
- [60] B. L. de Groot and H. Grubmüller. Water permeation across biological membranes: mechanism and dynamics of aquaporin-1 and GlpF. *Science*, 294(5550):2353–2357, 2001.
- [61] P. Debye and E. Hückel. The theory of electrolytes. I. Lowering of freezing point and related phenomena. *Phys. Z*, 24:185–206, 1923.
- [62] W. Denk, J. R. Holt, G. M. Shepherd, and D. P. Corey. Calcium imaging of single stereocilia in hair cells: Localization of transduction channels at both ends of tip links. *Neuron*, 15(6):1311–1321, 1995.
- [63] B. Derjaguin and L. Landau. Theory of the stability of strongly charged lyophobic sols and of the adhesion of strongly charged particles in solutions of electrolytes. *Progress in Surface Science*, 43(1):30–59, 1993.
- [64] T. J. Dolinsky, P. Czodrowski, H. Li, J. E. Nielsen, J. H. Jensen, G. Klebe, and N. A. Baker. PDB2PQR: expanding and upgrading automated preparation of biomolecular structures for molecular simulations. *Nucleic acids research*, 35(suppl 2):W522–W525, 2007.
- [65] T. J. Dolinsky, J. E. Nielsen, J. A. McCammon, and N. A. Baker. PDB2PQR: an automated pipeline for the setup of Poisson–Boltzmann electrostatics calculations. *Nucleic acids research*, 32(suppl 2):W665–W667, 2004.
- [66] B. N. Dominy and C. L. Brooks. Development of a generalized Born model parametrization for proteins and nucleic acids. *The Journal of Physical Chemistry B*, 103(18):3765–3773, 1999.
- [67] D. A. Doyle, J. M. Cabral, R. A. Pfuetzner, A. Kuo, J. M. Gulbis, S. L. Cohen, B. T. Chait, and R. MacKinnon. The structure of the potassium channel: molecular basis of K⁺ conduction and selectivity. *science*, 280(5360):69–77, 1998.
- [68] C. Duan, W. Wang, and Q. Xie. Review article: Fabrication of nanofluidic devices. *Biomicrofluidics*, 7(2):026501, 2013.
- [69] R. Dutzler, E. B. Campbell, M. Cadene, B. T. Chait, and R. MacKinnon. X-ray structure of a ClC chloride channel at 3.0 Å reveals the molecular basis of anion selectivity. *Nature*, 415(6869):287–294, 2002.
- [70] J. C. Eijkel and A. Van Den Berg. Nanofluidics: what is it and what can we expect from it? *Microfluidics and Nanofluidics*, 1(3):249–267, 2005.

- [71] B. Eisenberg, Y. Hyon, and C. Liu. Energy variational analysis of ions in water and channels: Field theory for primitive models of complex ionic fluids. *The Journal of chemical physics*, 133(10):104104, 2010.
- [72] R. Eisenberg and D. Chen. Poisson–Nernst–Planck theory of an open ionic channel. *Biophysical Journal*, 64(2):A22–A22, 1993.
- [73] D. Erickson, T. Rockwood, T. Emery, A. Scherer, and D. Psaltis. Nanofluidic tuning of photonic crystal circuits. In *Integrated Optoelectronic Devices 2007*, pages 647513–647513. International Society for Optics and Photonics, 2007.
- [74] H. Farris, C. LeBlanc, J. Goswami, and A. Ricci. Probing the pore of the auditory hair cell mechanotransducer channel in turtle. *The Journal of physiology*, 558(3):769–792, 2004.
- [75] X. Feng, K. Xia, Z. Chen, Y. Tong, and G.-W. Wei. Multiscale geometric modeling of macromolecules II: Lagrangian representation. *Journal of computational chemistry*, 34(24):2100–2120, 2013.
- [76] X. Feng, K. Xia, Y. Tong, and G.-W. Wei. Geometric modeling of subcellular structures, organelles, and multiprotein complexes. *International journal for numerical methods in biomedical engineering*, 28(12):1198–1223, 2012.
- [77] R. Fettiplace. Defining features of the hair cell mechanoelectrical transducer channel. *Pflügers Archiv-European Journal of Physiology*, 458(6):1115–1123, 2009.
- [78] R. Fettiplace and C. M. Hackney. The sensory and motor roles of auditory hair cells. *Nature Reviews Neuroscience*, 7(1):19–29, 2006.
- [79] R. Fettiplace and K. X. Kim. The physiology of mechanoelectrical transduction channels in hearing. *Physiological reviews*, 94(3):951–986, 2014.
- [80] F. Fogolari and J. M. Briggs. On the variational approach to Poisson–Boltzmann free energies. *Chemical Physics Letters*, 281(1):135–139, 1997.
- [81] F. Fogolari, A. Brigo, and H. Molinari. The Poisson–Boltzmann equation for biomolecular electrostatics: a tool for structural biology. *Journal of Molecular Recognition*, 15(6):377–392, 2002.
- [82] J. Fu, R. B. Schoch, A. L. Stevens, S. R. Tannenbaum, and J. Han. A patterned anisotropic nanofluidic sieving structure for continuous-flow separation of DNA and proteins. *Nature nanotechnology*, 2(2):121–128, 2007.
- [83] M. Gad-el Hak. The fluid mechanics of microdevices - The Freeman scholar lecture. *Journal of Fluids Engineering*, 121(1):5–33, 1999.
- [84] W. Geng and G.-W. Wei. Multiscale molecular dynamics using the matched interface and boundary method. *Journal of computational physics*, 230(2):435–457, 2011.

- [85] W. Geng, S. Yu, and G. Wei. Treatment of charge singularities in implicit solvent models. *The Journal of chemical physics*, 127(11):114106, 2007.
- [86] D. Gillespie. Energetics of divalent selectivity in a calcium channel: the ryanodine receptor case study. *Biophysical journal*, 94(4):1169–1184, 2008.
- [87] D. Gillespie, W. Nonner, and R. S. Eisenberg. Coupling Poisson–Nernst–Planck and density functional theory to calculate ion flux. *Journal of Physics: Condensed Matter*, 14(46):12129, 2002.
- [88] P. G. Gillespie and U. Müller. Mechanotransduction by hair cells: models, molecules, and mechanisms. *Cell*, 139(1):33–44, 2009.
- [89] M. K. Gilson, M. E. Davis, B. A. Luty, and J. A. McCammon. Computation of electrostatic forces on solvated molecules using the Poisson–Boltzmann equation. *The Journal of Physical Chemistry*, 97(14):3591–3600, 1993.
- [90] G. Gouy. Constitution of the electric charge at the surface of an electrolyte. *J. phys*, 9(4):457–467, 1910.
- [91] D. C. Grahame. The electrical double layer and the theory of electrocapillarity. *Chemical Reviews*, 41(3):441–501, 1947.
- [92] P. Grochowski and J. Trylska. Continuum molecular electrostatics, salt effects, and counterion binding – a review of the Poisson–Boltzmann theory and its modifications. *Biopolymers*, 89(2):93–113, 2008.
- [93] W. Guan, S. X. Li, and M. A. Reed. Voltage gated ion and molecule transport in engineered nanochannels: theory, fabrication and applications. *Nanotechnology*, 25(12):122001, 2014.
- [94] M. Hacker, W. S. Messer II, and K. A. Bachmann. *Pharmacology: principles and practice*. Academic Press, 2009.
- [95] J. Han, S. Turner, and H. Craighead. Entropic trapping and escape of long DNA molecules at submicron size constriction. *Physical review letters*, 83(8):1688, 1999.
- [96] Y. He, D. Gillespie, D. Boda, I. Vlassiouk, R. S. Eisenberg, and Z. S. Siwy. Tuning transport properties of nanofluidic devices with local charge inversion. *Journal of the American Chemical Society*, 131(14):5194–5202, 2009.
- [97] J. Hermans, H. J. Berendsen, W. F. Van Gunsteren, and J. P. Postma. A consistent empirical potential for water–protein interactions. *Biopolymers*, 23(8):1513–1518, 1984.
- [98] B. Hille. *Ion channels of excitable membranes*, volume 507. Sinauer Sunderland, MA, 2001.
- [99] A. L. Hodgkin and A. F. Huxley. The dual effect of membrane potential on sodium conductance in the giant axon of *Loligo*. *The Journal of physiology*, 116(4):497–506, 1952.

- [100] A. L. Hodgkin and A. F. Huxley. A quantitative description of membrane current and its application to conduction and excitation in nerve. *The Journal of physiology*, 117(4):500, 1952.
- [101] U. Hollerbach, D.-P. Chen, and R. S. Eisenberg. Two-and three-dimensional Poisson–Nernst–Planck simulations of current flow through Gramicidin A. *Journal of Scientific Computing*, 16(4):373–409, 2001.
- [102] M. J. Holst. *The Poisson-Boltzmann Equation: Analysis and Multilevel Numerical Solution*. PhD thesis, Numerical Computing Group, University of Illinois at Urbana-Champaign, 1994.
- [103] B. Honig and A. Nicholls. Classical electrostatics in biology and chemistry. *SCIENCE-NEW YORK THEN WASHINGTON-*, pages 1144–1144, 1995.
- [104] J. Howard and A. Hudspeth. Compliance of the hair bundle associated with gating of mechanoelectrical transduction channels in the bullfrog’s saccular hair cell. *Neuron*, 1(3):189–199, 1988.
- [105] G. Hu and D. Li. Multiscale phenomena in microfluidics and nanofluidics. *Chemical Engineering Science*, 62(13):3443–3454, 2007.
- [106] Y. Hyon, B. Eisenberg, and C. Liu. A mathematical model for the hard sphere repulsion in ionic solutions. *Commun. Math. Sci*, 9(2):459–475, 2011.
- [107] W. Im and B. Roux. Ion permeation and selectivity of OmpF porin: a theoretical study based on molecular dynamics, Brownian dynamics, and continuum electrodiffusion theory. *Journal of molecular biology*, 322(4):851–869, 2002.
- [108] W. Im, S. Seefeld, and B. Roux. A Grand Canonical Monte Carlo–Brownian dynamics algorithm for simulating ion channels. *Biophysical Journal*, 79(2):788–801, 2000.
- [109] F. Jaramillo and A. Hudspeth. Localization of the hair cell’s transduction channels at the hair bundle’s top by iontophoretic application of a channel blocker. *Neuron*, 7(3):409–420, 1991.
- [110] J. W. Jerome. *Analysis of charge transport*. Springer, 1996.
- [111] J. Jiang, D. Cao, D.-e. Jiang, and J. Wu. Time-dependent density functional theory for ion diffusion in electrochemical systems. *Journal of Physics: Condensed Matter*, 26(28):284102, 2014.
- [112] P. C. Jordan. Fifty years of progress in ion channel research. *NanoBioscience, IEEE Transactions on*, 4(1):3–9, 2005.
- [113] W. L. Jorgensen, D. S. Maxwell, and J. Tirado-Rives. Development and testing of the OPLS all-atom force field on conformational energetics and properties of organic liquids. *Journal of the American Chemical Society*, 118(45):11225–11236, 1996.

- [114] Y.-W. Jung, B. Lu, and M. Mascagni. A computational study of ion conductance in the KcsA K^+ channel using a nernst–planck model with explicit resident ions. *The Journal of chemical physics*, 131(21):215101, 2009.
- [115] R. Karnik, K. Castelino, R. Fan, P. Yang, and A. Majumdar. Effects of biological reactions and modifications on conductance of nanofluidic channels. *Nano letters*, 5(9):1638–1642, 2005.
- [116] R. Karnik, K. Castelino, and A. Majumdar. Field-effect control of protein transport in a nanofluidic transistor circuit. *Applied Physics Letters*, 88(12):123114, 2006.
- [117] R. Karnik, C. Duan, K. Castelino, H. Daiguji, and A. Majumdar. Rectification of ionic current in a nanofluidic diode. *Nano letters*, 7(3):547–551, 2007.
- [118] R. Karnik, R. Fan, M. Yue, D. Li, P. Yang, and A. Majumdar. Electrostatic control of ions and molecules in nanofluidic transistors. *Nano letters*, 5(5):943–948, 2005.
- [119] M. Karplus and J. A. McCammon. Molecular dynamics simulations of biomolecules. *Nature Structural & Molecular Biology*, 9(9):646–652, 2002.
- [120] J. J. Kasianowicz, E. Brandin, D. Branton, and D. W. Deamer. Characterization of individual polynucleotide molecules using a membrane channel. *Proceedings of the National Academy of Sciences*, 93(24):13770–13773, 1996.
- [121] P. Kazmierczak and U. Müller. Sensing sound: molecules that orchestrate mechanotransduction by hair cells. *Trends in neurosciences*, 35(4):220–229, 2012.
- [122] P. Kazmierczak, H. Sakaguchi, J. Tokita, E. M. Wilson-Kubalek, R. A. Milligan, U. Müller, and B. Kachar. Cadherin 23 and protocadherin 15 interact to form tip-link filaments in sensory hair cells. *Nature*, 449(7158):87–91, 2007.
- [123] H. Kennedy, A. Crawford, and R. Fettiplace. Force generation by mammalian hair bundles supports a role in cochlear amplification. *Nature*, 433(7028):880–883, 2005.
- [124] H. J. Kennedy, M. G. Evans, A. C. Crawford, and R. Fettiplace. Fast adaptation of mechanoelectrical transducer channels in mammalian cochlear hair cells. *Nature neuroscience*, 6(8):832–836, 2003.
- [125] F. Khalili-Araghi, J. Gumbart, P.-C. Wen, M. Sotomayor, E. Tajkhorshid, and K. Schulten. Molecular dynamics simulations of membrane channels and transporters. *Current opinion in structural biology*, 19(2):128–137, 2009.
- [126] F. Khalili-Araghi, E. Tajkhorshid, and K. Schulten. Dynamics of K^+ ion conduction through Kv1. 2. *Biophysical journal*, 91(6):L72–L74, 2006.
- [127] M. S. Kilic, M. Z. Bazant, and A. Ajdari. Steric effects in the dynamics of electrolytes at large applied voltages. I. Double-layer charging. *Physical Review E*, 75(2):021502, 2007.

- [128] M. S. Kilic, M. Z. Bazant, and A. Ajdari. Steric effects in the dynamics of electrolytes at large applied voltages. II. Modified Poisson–Nernst–Planck equations. *Physical Review E*, 75(2):021503, 2007.
- [129] M. G. Kurnikova, R. D. Coalson, P. Graf, and A. Nitzan. A lattice relaxation algorithm for three–dimensional Poisson–Nernst–Planck theory with application to ion transport through the Gramicidin A channel. *Biophysical Journal*, 76(2):642–656, 1999.
- [130] G. Lamm. The Poisson–Boltzmann equation. *Reviews in Computational Chemistry*, 19:147–333, 2003.
- [131] K. I. Lee, H. Rui, R. W. Pastor, and W. Im. Brownian dynamics simulations of ion transport through the VDAC. *Biophysical journal*, 100(3):611–619, 2011.
- [132] Y. Levin. Electrostatic correlations: from plasma to biology. *Reports on progress in physics*, 65(11):1577, 2002.
- [133] D. G. Levitt. Modeling of ion channels. *The Journal of general physiology*, 113(6):789–794, 1999.
- [134] J. Li, M. Gershow, D. Stein, E. Brandin, and J. Golovchenko. DNA molecules and configurations in a solid-state nanopore microscope. *Nature materials*, 2(9):611–615, 2003.
- [135] S. B. Long, E. B. Campbell, and R. MacKinnon. Crystal structure of a mammalian voltage-dependent shaker family K^+ channel. *Science*, 309(5736):897–903, 2005.
- [136] C. D. Lorenz, P. S. Crozier, J. A. Anderson, and A. Travasset. Molecular dynamics of ionic transport and electrokinetic effects in realistic silica channels. *The Journal of Physical Chemistry C*, 112(27):10222–10232, 2008.
- [137] C. D. Lorenz and A. Travasset. Charge inversion of divalent ionic solutions in silica channels. *Physical Review E*, 75(6):061202, 2007.
- [138] B. Lu and Y. Zhou. Poisson–Nernst–Planck equations for simulating biomolecular diffusion–reaction processes II: size effects on ionic distributions and diffusion–reaction rates. *Biophysical journal*, 100(10):2475–2485, 2011.
- [139] B. Lu, Y. Zhou, M. Holst, and J. McCammon. Recent progress in numerical methods for the Poisson–Boltzmann equation in biophysical applications. *Commun Comput Phys*, 3(5):973–1009, 2008.
- [140] B. Lu, Y. Zhou, G. A. Huber, S. D. Bond, M. J. Holst, and J. A. McCammon. Electrodifusion: A continuum modeling framework for biomolecular systems with realistic spatiotemporal resolution. *The Journal of chemical physics*, 127(13):135102, 2007.
- [141] R. Lynden-Bell and J. C. Rasaiah. Mobility and solvation of ions in channels. *The Journal of chemical physics*, 105(20):9266–9280, 1996.

- [142] D. Mackay, P. H. Berens, K. R. Wilson, and A. Hagler. Structure and dynamics of ion transport through Gramicidin A. *Biophysical journal*, 46(2):229–248, 1984.
- [143] A. D. MacKerell, D. Bashford, M. Bellott, R. Dunbrack, J. Evanseck, M. J. Field, S. Fischer, J. Gao, H. Guo, S. a. Ha, et al. All-atom empirical potential for molecular modeling and dynamics studies of proteins. *The Journal of Physical Chemistry B*, 102(18):3586–3616, 1998.
- [144] R. MacKinnon. Potassium channels and the atomic basis of selective ion conduction (Nobel Lecture). *Angewandte Chemie International Edition*, 43(33):4265–4277, 2004.
- [145] C. Maffeo and A. Aksimentiev. Structure, dynamics, and ion conductance of the phospholamban pentamer. *Biophysical journal*, 96(12):4853–4865, 2009.
- [146] C. Maffeo, S. Bhattacharya, J. Yoo, D. Wells, and A. Aksimentiev. Modeling and simulation of ion channels. *Chemical reviews*, 112(12):6250–6284, 2012.
- [147] M. Manciu and E. Ruckenstein. On the chemical free energy of the electrical double layer. *Langmuir*, 19(4):1114–1120, 2003.
- [148] D. Marx and J. Hutter. Ab initio molecular dynamics: Theory and implementation. *Modern methods and algorithms of quantum chemistry*, 1:301–449, 2000.
- [149] J. A. McCammon, B. R. Gelin, and M. Karplus. Dynamics of folded proteins. *Nature*, 267:585–590, 1977.
- [150] Y. Mei, C. Ji, and J. Z. Zhang. A new quantum method for electrostatic solvation energy of protein. *The Journal of chemical physics*, 125(9):094906, 2006.
- [151] D. Mijatovic, J. Eijkel, and A. Van Den Berg. Technologies for nanofluidic systems: top-down vs. bottom-up – a review. *Lab on a Chip*, 5(5):492–500, 2005.
- [152] N. Modi, P. R. Singh, K. R. Mahendran, R. Schulz, M. Winterhalter, and U. Kleinekathofer. Probing the transport of ionic liquids in aqueous solution through nanopores. *The Journal of Physical Chemistry Letters*, 2(18):2331–2336, 2011.
- [153] N. Modi, M. Winterhalter, and U. Kleinekathoefer. Computational modeling of ion transport through nanopores. *Nanoscale*, 4(20):6166–6180, 2012.
- [154] M. R. Mohamadi, L. Mahmoudian, N. Kaji, M. Tokeshi, H. Chuman, and Y. Baba. Nanotechnology for genomics & proteomics. *Nano Today*, 1(1):38–45, 2006.
- [155] M. T. Neves-Petersen and S. B. Petersen. Protein electrostatics: a review of the equations and methods used to model electrostatic equations in biomolecules–applications in biotechnology. *Biotechnology annual review*, 9:315–395, 2003.
- [156] H. Ohmori. Mechano-electrical transduction currents in isolated vestibular hair cells of the chick. *The Journal of Physiology*, 359(1):189–217, 1985.

- [157] H. Ohshima and K. Furusawa. *Electrical Phenomena at Interfaces: Fundamentals, Measurements, and Applications*, volume 76. CRC Press, 1998.
- [158] B. Pan, J. Waguespack, M. E. Schnee, C. LeBlanc, and A. J. Ricci. Permeation properties of the hair cell mechanotransducer channel provide insight into its molecular structure. *Journal of neurophysiology*, 107(9):2408–2420, 2012.
- [159] A. W. Peng, F. T. Salles, B. Pan, and A. J. Ricci. Integrating the biophysical and molecular mechanisms of auditory hair cell mechanotransduction. *Nature communications*, 2:523, 2011.
- [160] J. L. Perry and S. G. Kandlikar. Review of fabrication of nanochannels for single phase liquid flow. *Microfluidics and Nanofluidics*, 2(3):185–193, 2006.
- [161] J. M. Perry, K. Zhou, Z. D. Harms, and S. C. Jacobson. Ion transport in nanofluidic funnels. *ACS nano*, 4(7):3897–3902, 2010.
- [162] S. Prakash, A. Piruska, E. N. Gatimu, P. W. Bohn, J. V. Sweedler, and M. A. Shannon. Nanofluidics: systems and applications. *Sensors Journal, IEEE*, 8(5):441–450, 2008.
- [163] Q. Pu, J. Yun, H. Temkin, and S. Liu. Ion-enrichment and ion-depletion effect of nanochannel structures. *Nano Letters*, 4(6):1099–1103, 2004.
- [164] A. Ricci, B. Kachar, J. Gale, and S. Van Netten. Mechano-electrical transduction: new insights into old ideas. *The Journal of membrane biology*, 209(2-3):71–88, 2006.
- [165] A. J. Ricci, A. C. Crawford, and R. Fettiplace. Tonotopic variation in the conductance of the hair cell mechanotransducer channel. *Neuron*, 40(5):983–990, 2003.
- [166] F. M. Richards. Areas, volumes, packing and protein structure. *Annual review of biophysics and bioengineering*, 6:151–76, 1977.
- [167] R. Roth and D. Gillespie. Physics of size selectivity. *Physical Review Letters*, 95(24):247801, 2005.
- [168] B. Roux, T. Allen, S. Berneche, and W. Im. Theoretical and computational models of biological ion channels. *Quarterly reviews of biophysics*, 37(01):15–103, 2004.
- [169] G. Rutkai and T. Kristóf. Dynamic Monte Carlo simulation in mixtures. *The Journal of chemical physics*, 132(10):104107, 2010.
- [170] M. F. Sanner, A. J. Olson, and J.-C. Spohner. Reduced surface: an efficient way to compute molecular surfaces. *Biopolymers*, 38(3):305–320, 1996.
- [171] R. B. Schoch, A. Bertsch, and P. Renaud. pH-controlled diffusion of proteins with different pI values across a nanochannel on a chip. *Nano letters*, 6(3):543–547, 2006.
- [172] R. B. Schoch, J. Han, and P. Renaud. Transport phenomena in nanofluidics. *Reviews of Modern Physics*, 80(3):839, 2008.

- [173] R. B. Schoch and P. Renaud. Ion transport through nanoslits dominated by the effective surface charge. *Applied Physics Letters*, 86(25):253111, 2005.
- [174] R. Schulz and U. Kleinekathöfer. Transitions between closed and open conformations of TolC: the effects of ions in simulations. *Biophysical journal*, 96(8):3116–3125, 2009.
- [175] M. Schwander, B. Kachar, and U. Müller. The cell biology of hearing. *The Journal of cell biology*, 190(1):9–20, 2010.
- [176] K. A. Sharp and B. Honig. Calculating total electrostatic energies with the nonlinear Poisson–Boltzmann equation. *Journal of Physical Chemistry*, 94(19):7684–7692, 1990.
- [177] K. A. Sharp and B. Honig. Electrostatic interactions in macromolecules: theory and applications. *Annual review of biophysics and biophysical chemistry*, 19(1):301–332, 1990.
- [178] K. Shirono, N. Tatsumi, and H. Daiguji. Molecular simulation of ion transport in silica nanopores. *The Journal of Physical Chemistry B*, 113(4):1041–1047, 2009.
- [179] S. W. Siu and R. A. Böckmann. Electric field effects on membranes: Gramicidin A as a test ground. *Journal of structural biology*, 157(3):545–556, 2007.
- [180] Z. Siwy, P. Apel, D. Baur, D. D. Dobrev, Y. E. Korchev, R. Neumann, R. Spohr, C. Trautmann, and K.-O. Voss. Preparation of synthetic nanopores with transport properties analogous to biological channels. *Surface Science*, 532:1061–1066, 2003.
- [181] Z. Siwy, D. Dobrev, R. Neumann, C. Trautmann, and K. Voss. Electro-responsive asymmetric nanopores in polyimide with stable ion-current signal. *Applied Physics A*, 76(5):781–785, 2003.
- [182] Z. Siwy, Y. Gu, H. Spohr, D. Baur, A. Wolf-Reber, R. Spohr, P. Apel, and Y. Korchev. Rectification and voltage gating of ion currents in a nanofabricated pore. *EPL (Europhysics Letters)*, 60(3):349, 2002.
- [183] Z. Siwy, E. Heins, C. C. Harrell, P. Kohli, and C. R. Martin. Conical-nanotube ion-current rectifiers: the role of surface charge. *Journal of the American Chemical Society*, 126(35):10850–10851, 2004.
- [184] Z. S. Siwy. Ion-current rectification in nanopores and nanotubes with broken symmetry. *Advanced Functional Materials*, 16(6):735–746, 2006.
- [185] Z. S. Siwy and S. Howorka. Engineered voltage-responsive nanopores. *Chemical Society Reviews*, 39(3):1115–1132, 2010.
- [186] J. Song, R. Evans, Y.-Y. Lin, B.-N. Hsu, and R. Fair. A scaling model for electrowetting-on-dielectric microfluidic actuators. *Microfluidics and Nanofluidics*, 7(1):75–89, 2009.
- [187] M. Sotomayor and K. Schulten. Molecular dynamics study of gating in the mechanosensitive channel of small conductance MscS. *Biophysical journal*, 87(5):3050–3065, 2004.

- [188] W. Sparreboom, A. Van Den Berg, and J. Eijkel. Principles and applications of nanofluidic transport. *Nature Nanotechnology*, 4(11):713–720, 2009.
- [189] W. Sparreboom, A. Van Den Berg, and J. Eijkel. Transport in nanofluidic systems: a review of theory and applications. *New Journal of Physics*, 12(1):015004, 2010.
- [190] D. Stein, M. Kruithof, and C. Dekker. Surface-charge-governed ion transport in nanofluidic channels. *Physical Review Letters*, 93(3):035901, 2004.
- [191] S. Sukharev, S. R. Durell, and H. R. Guy. Structural models of the MscL gating mechanism. *Biophysical journal*, 81(2):917–936, 2001.
- [192] J. Timko, D. Bucher, and S. Kuyucak. Dissociation of NaCl in water from ab initio molecular dynamics simulations. *The Journal of chemical physics*, 132(11):114510, 2010.
- [193] J. Tomasi, B. Mennucci, and R. Cammi. Quantum mechanical continuum solvation models. *Chemical reviews*, 105(8):2999–3094, 2005.
- [194] B. Tu, M. Chen, Y. Xie, L. Zhang, B. Eisenberg, and B. Lu. A parallel finite element simulator for ion transport through three-dimensional ion channel systems. *Journal of computational chemistry*, 34(24):2065–2078, 2013.
- [195] S. Turner, M. Cabodi, and H. Craighead. Confinement-induced entropic recoil of single DNA molecules in a nanofluidic structure. *Physical Review Letters*, 88(12):128103, 2002.
- [196] B. M. Venkatesan and R. Bashir. Nanopore sensors for nucleic acid analysis. *Nature nanotechnology*, 6(10):615–624, 2011.
- [197] E. J. W. Verwey, J. T. G. Overbeek, and J. T. G. Overbeek. *Theory of the stability of lyophobic colloids*. Courier Dover Publications, 1999.
- [198] V. Vlachy. Ionic effects beyond Poisson–Boltzmann theory. *Annual review of physical chemistry*, 50(1):145–165, 1999.
- [199] I. Vlassiouk, S. Smirnov, and Z. Siwy. Ionic selectivity of single nanochannels. *Nano letters*, 8(7):1978–1985, 2008.
- [200] I. Vlassiouk, S. Smirnov, and Z. Siwy. Nanofluidic ionic diodes. Comparison of analytical and numerical solutions. *Acs Nano*, 2(8):1589–1602, 2008.
- [201] B. Wallace. Recent advances in the high resolution structures of bacterial channels: Gramicidin A. *Journal of structural biology*, 121(2):123–141, 1998.
- [202] J. Wang, M. Lin, A. Crenshaw, A. Hutchinson, B. Hicks, M. Yeager, S. Berndt, W.-Y. Huang, R. B. Hayes, S. J. Chanock, et al. High-throughput single nucleotide polymorphism genotyping using nanofluidic dynamic arrays. *BMC genomics*, 10(1):561, 2009.

- [203] Y. Wang, K. Pant, Z. Chen, G. Wang, W. F. Diffey, P. Ashley, and S. Sundaram. Numerical analysis of electrokinetic transport in micro-nanofluidic interconnect pre-concentrator in hydrodynamic flow. *Microfluidics and nanofluidics*, 7(5):683–696, 2009.
- [204] Y.-C. Wang, A. L. Stevens, and J. Han. Million-fold preconcentration of proteins and peptides by nanofluidic filter. *Analytical chemistry*, 77(14):4293–4299, 2005.
- [205] J. D. Weeks, D. Chandler, and H. C. Andersen. Role of repulsive forces in determining the equilibrium structure of simple liquids. *The Journal of chemical physics*, 54(12):5237–5247, 1971.
- [206] G.-W. Wei. Differential geometry based multiscale models. *Bulletin of mathematical biology*, 72(6):1562–1622, 2010.
- [207] G.-W. Wei. Multiscale, multiphysics and multidomain models I: Basic theory. *Journal of Theoretical and Computational Chemistry*, 12(08), 2013.
- [208] G.-W. Wei, Q. Zheng, Z. Chen, and K. Xia. Variational multiscale models for charge transport. *SIAM Review*, 54(4):699–754, 2012.
- [209] P. K. Weiner and P. A. Kollman. AMBER: Assisted model building with energy refinement. A general program for modeling molecules and their interactions. *Journal of Computational Chemistry*, 2(3):287–303, 1981.
- [210] D. Wu and A. J. Steckl. High speed nanofluidic protein accumulator. *Lab on a Chip*, 9(13):1890–1896, 2009.
- [211] J. Wu and Z. Li. Density-functional theory for complex fluids. *Annu. Rev. Phys. Chem.*, 58:85–112, 2007.
- [212] K. Xia, X. Feng, Z. Chen, Y. Tong, and G.-W. Wei. Multiscale geometric modeling of macromolecules I: Cartesian representation. *Journal of computational physics*, 257:912–936, 2014.
- [213] K. Xia, K. Opron, and G.-W. Wei. Multiscale multiphysics and multidomain models-flexibility and rigidity. *The Journal of chemical physics*, 139(19):194109, 2013.
- [214] K. Xia, M. Zhan, and G.-W. Wei. The matched interface and boundary (MIB) method for multi-domain elliptic interface problems. *J. Comput. Phys*, 230:8231–8258, 2011.
- [215] R. Yan, W. Liang, R. Fan, and P. Yang. Nanofluidic diodes based on nanotube heterojunctions. *Nano letters*, 9(11):3820–3825, 2009.
- [216] S. Yu, W. Geng, and G. Wei. Treatment of geometric singularities in implicit solvent models. *The Journal of chemical physics*, 126(24):244108, 2007.
- [217] S. Yu and G. Wei. Three-dimensional matched interface and boundary (MIB) method for treating geometric singularities. *Journal of Computational Physics*, 227(1):602–632, 2007.

- [218] Z. Yuan, A. L. Garcia, G. P. Lopez, and D. N. Petsev. Electrokinetic transport and separations in fluidic nanochannels. *Electrophoresis*, 28(4):595–610, 2007.
- [219] S. Zhao and G. Wei. High-order FDTD methods via derivative matching for Maxwell’s equations with material interfaces. *Journal of Computational Physics*, 200(1):60–103, 2004.
- [220] Q. Zheng, D. Chen, and G.-W. Wei. Second-order Poisson–Nernst–Planck solver for ion transport. *Journal of computational physics*, 230(13):5239–5262, 2011.
- [221] Q. Zheng and G.-W. Wei. Poisson–Boltzmann–Nernst–Planck model. *The Journal of chemical physics*, 134(19):194101, 2011.
- [222] Z. Zheng, D. J. Hansford, and A. T. Conlisk. Effect of multivalent ions on electroosmotic flow in micro-and nanochannels. *Electrophoresis*, 24(17):3006–3017, 2003.
- [223] K. Zhou, J. M. Perry, and S. C. Jacobson. Transport and sensing in nanofluidic devices. *Annual Review of Analytical Chemistry*, 4:321–341, 2011.
- [224] Y. Zhou, M. Feig, and G.-W. Wei. Highly accurate biomolecular electrostatics in continuum dielectric environments. *Journal of Computational Chemistry*, 29(1):87–97, 2008.
- [225] Y. Zhou, B. Lu, G. A. Huber, M. J. Holst, and J. A. McCammon. Continuum simulations of acetylcholine consumption by acetylcholinesterase: A Poisson–Nernst–Planck approach. *The Journal of Physical Chemistry B*, 112(2):270–275, 2008.
- [226] Y. Zhou, S. Zhao, M. Feig, and G.-W. Wei. High order matched interface and boundary method for elliptic equations with discontinuous coefficients and singular sources. *Journal of Computational Physics*, 213(1):1–30, 2006.
- [227] Z. Zhou, P. Payne, M. Vasquez, N. Kuhn, and M. Levitt. Finite-difference solution of the Poisson–Boltzmann equation: Complete elimination of self-energy. *Journal of computational chemistry*, 17(11):1344–1351, 1996.